POST-DEPOSITION DOPING OF

SILICON NANOWIRES

by

Jané Bronwyn Slinger

A thesis submitted in partial fulfilment of the requirements for the degree of

Magister Scientiae in the Department of Physics (Nanoscience), University of the

Western Cape (UWC)

Supervisor **: Prof. C.J. Arendse, University of the Western Cape (UWC)**

Co-supervisor(s) **: Dr F.R. Cummings, University of the Western Cape (UWC)**

: Dr C.J. Oliphant, National Metrology Institute of South

Africa (NMISA)

October 2017

Dedications

Impossible is just a big word thrown around by small men who find it easier

to live in the world they've been given than to explore the power they have to

change it.

Impossible is not a fact. It's an opinion.

Impossible is not a declaration. It's a dare.

Impossible is potential.

Impossible is temporary.

Impossible is nothing

Muhammad Ali (1942 – 2016)

Dedicated to my parents, two brothers and Patrick

Acknowledgements

"With man this is impossible, but with God all things are possible."

– Matthew 19:26

I am grateful to the following people and organisations without whose assistance, advice and guidance the completion of this thesis would not be possible

To Prof. Christopher Arendse (Department of Physics and Astronomy, UWC): For the excellent supervision of this thesis, guidance, patience and understanding throughout the process.

To Dr Franscious Cummings (Department of Physics and Astronomy, UWC): Thank you for your unselfish help throughout the course of this process; for the SEM and TEM characterisations and data analysis; for the many stimulating discussions.

To Dr Clive Oliphant (National Metrology Institute of South Africa): Thank you for your unselfish help throughout the course of this process; for the XRD characterisation; for the many stimulating discussions; and for your understanding.

To the Electron Microscopy Unit (University of the Western Cape) and the National Metrology Institute of South Africa for all the microscopy work.

To Mr Earl Mc Donald, Mrs Louise Mostert, and Mr Werner Jordaan for the SEM, EDS, and XPS characterisations.

iv

especially the staff at the Transport Services and the faculty of Natural Science for helping me throughout the years.

To my intermediate family:

Mummy – thank you for being my pillar of strength, for always lending a listening ear, for the effort you put into making me happy. *I Love You!*

Daddy – Thank you for always putting me first; for ensuring that I have everything that I need, especially when it comes to food; for never hesitating to make sure I have everything I need. *I Love You!*

Justin & Allan – Thank you for coping with me, especially when it comes to me complaining; for being a support structure; and for understanding my absence*. I Love You!*

To Patrick: Thank you for being there for me through every step of the way; for always being by my side; for understanding my absence; for your patience and support in literally everything. I cannot thank you enough. *I Love You!*

To my extended family, neighbours, and friends: Thank you for the constant belief in me; for the constant prayers and support.

THANK YOU!!

Declaration

I declare that

"POST-DEPOSITION DOPING OF SILICON NANOWIRES"

Is my own work, that it has not been submitted for any degree or examination in any other university, and that all the sources I have used or quoted have been indicated and acknowledged by means of complete references.
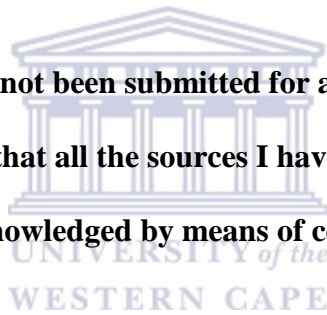
Jané Bronwyn Slinger   **October 2017**

Signature……………..

Keywords

POST-DEPOSITION DOPING OF SILICON NANOWIRES

Jané Bronwyn Slinger

Photovoltaics

Silicon

Silicon Nanowires

Phosphorus Diffusion

Metal-assisted Chemical Etching

Post-doping

Morphology

Structural Properties

Composition

Hall effect

Abstract

POST-DEPOSITION DOPING OF SILICON NANOWIRES

Jané Bronwyn Slinger

M.Sc. Thesis, Department of Physics, University of the Western Cape

Silicon nanowires (Si NWs) continue to demonstrate superior properties to their bulk counterparts, with respect to their morphological and electrical transport properties for the use in photovoltaic (PV) applications. The two most common and simplest approaches for Si NW fabrication are the bottom-up approach, namely, vapour-liquid-solid (VLS) growth and the top-down approach, namely, the metal-assisted chemical etching (MaCE) fabrication technique. Thermal diffusion of phosphorus (P) in Si is at present the primary method for emitter formation in Si solar cell processing. Most work done in the literature that is based on the diffusion doping of Si NWs has been carried out by means of VLS-grown Si NWs. Therefore, there is a lack of the understanding of the particular diffusion mechanism of applying the phosphorus dopant source to the MaCE-grown Si NWs.

In this study, Si NW formation was thus induced by etching the Silver (Ag)-coated p-type polished single-crystalline (100) Si wafer in a hydrofluoric/peroxide (HF/H_2O_2) solution at pre-determined molar ratios. Thereafter, the p-type Si NWs were spin cast with liquid phosphorus-oxychloride ($POCl_3$), an n-type P-containing spin-on dopant

(SOD) source, which was followed by drive-in diffusion annealing in a nitrogen carrier gas (N_2) high-temperature furnace.

The focus of this study was to interrogate the effect of the annealing temperature (ranging from 700 to 1000 °C) on the morphological, structural, compositional, and electrical transport properties of the MaCE-grown Si NWs. In particular, scanning electron microscopy (SEM) and transmission electron microscopy (TEM) were used to study the effect of n-type doping on the morphological properties of the MaCE-grown Si NWs. TEM and X-ray diffraction (XRD) were used to evaluate whether the MaCE-grown Si NWs and n-doped Si NWs maintained the original structural properties of the bulk single-crystalline (100) Si wafer. X-ray photoelectron spectroscopy (XPS) was used to study the chemical composition of the n-doped Si NW annealed at 1000 °C. Lastly, the temperature dependence of electrical transport properties on the n-doped Si NWs using the Hall effect measurement technique was interrogated.

The SEM and TEM results show that the morphological properties of the MaCE-grown Si NWs changes post-annealing. The diameter and length for the n-doped Si NWs enhance from 133 ± 22 nm to 160 ± 17 nm and reduces from 8.21 ± 0.27 μm to 4.48 ± 0.14 μm as compared to the as-synthesised Si NWs due to the parasitic layers formed post-annealing and to the wafer damage during SEM preparation, respectively. The TEM results show that the surface roughness of the MaCE-grown Si NWs alters post-annealing, due to the N_2 carrier gas ambient. The TEM and XRD results show that the MaCE-grown Si NWs and n-doped Si NWs maintained the single-crystalline diamond lattice structure of the starting (100) Si wafer. The XPS results show that the phosphorus dopant atoms tend to exist mostly within the Si NWs since phosphorus has a low diffusivity and high segregation coefficient in SiO_2. The hall effect measurement

technique shows that that electrical transport properties improve with increasing annealing temperature.

October 2017

List of Abbreviations

A

Å	: Angstrom
Ag ions	: Silver ions
$AgNO_3$	: Silver nitrate
Al	: Aluminium
AM 1.5	: Global Air Mass 1.5
Ar	: Argon
As	: Arsenic
Au	: Gold

B

B	: Boron
BE	: Binding energy

C

C	: Carbon
°C	: Degree Celsius

CB : Conduction band

Cl_2 : Chlorine gas

cm : Centimetre

cm^2/s : Square centimetre per second

CO_2 : Carbon dioxide

Cu : Copper

CVD : Chemical vapour deposition

Cz : Czochralski

C_2H_60 : Ethanol

C_3H_60 : Acetone

D

DI : Deionised water

DOF : Depth of field

DOS : Density of states

E

EDS : Energy dispersive spectroscopy

EELS : Electron energy loss spectroscopy

EMU   : Electron Microscope Unit

eV   : Electronvolt

F

FEG-SEM   : Field emission gun scanning electron microscope

FEG-TEM   : Field emission gun transmission electron microscope

FETs   : Field-effect transistors

FTIR   : Fourier transport infrared spectroscopy

FWHM   : Full width at half maximum

FZ   : Float-zone

G

GaAs   : Gallium arsenide

Ge   : Germanium

GHGs   : Greenhouse gases

H

H   : Hydrogen

HCl   : Hydrogen Chloride

HF   : Hydrofluoric acid

H_2O_2 : Hydrogen peroxide

Hr	: Hour
HR-TEM	: High-resolution transmission electron microscopy
HSiCl$_3$	: Trichlorosilane

I

ICs	: Integrated circuits

K

KE	: Kinetic energy
keV	: Kiloelectron volt
kV	: Kilovolt

M

M	: Molar concentration
mA	: Milliampere
MaCE	: Metal-assisted chemical etching
mA/cm^2	: Milliampere per square centimetre
mbar	: millibar
MCA	: Multichannel analyser
MeV	: Megaelectron volt
MFC	: Mass flow control

mg	: milligrams
MGS	: Metallurgical grade silicon
mL	: Millilitre
mm	: Millimetre
$MoSi_2$	: Molybdenum disilicide
mV	: Millivolt
MW	: Megawatt

N

N_2	: Nitrogen gas
NA	: Numerical aperture
nm	: nanometre
NMISA	: National metrology institute of South Africa
NPs	: Nanoparticles
NWs	: Nanowires

O

O_2	: Oxygen gas
OAG	: Oxide-assisted growth

P

P	: Phosphorus
Pd	: Palladium
PL	: Photoluminescence
Pm	: Petameter
P_2O_5	: Phosphorus pentoxide
$POCl_3$	: Phosphorus oxychloride
PSG	: Phosphorus silicate glass
PTFE	: Polytetrafluoroethylene
PV	: Current temperature
PVs	: Photovoltaics

R

RE	: Renewable energy
rpm	: Rotations per minute

S

s	: Seconds
SAED	: Selected area electron diffraction

Sb : Antimony

SC : Solar cell

sccm : Standard cubic centimetre per minute

SDD : Silicon drift detector

SEC : Solar energy conversion

SEM : Scanning electron microscopy

Si : Silicon

$SiCl_4$: Silicon tetrachloride

SiH_4 : Silane

Si NWs : Silicon nanowires

SiO_2 : Silicon dioxide

SOD : Spin-on dopant

SV : Set temperature

T

T : Tesla

TCVD : Thermal chemical vapour deposition

TEM : Transmission electron microscopy

U

μm	: Micrometre
μW	: Microwatt

V

VB	: Valence band
VLS	: Vapour-liquid-solid

W

W	: Watt
WD	: Working distance

Table of Content

UNIVERSITY *of the*

WESTERN CAPE

Chapter One: Introduction

1.1 The Energy Crisis and Renewable Energy

It is realised that the burning of fossil fuels for electricity generation is affecting the Earth's atmosphere. Carbon dioxide (CO_2) emissions produced globally from the combustion of fossil fuels have a significant impact on greenhouse gases (GHGs) in the atmosphere, resulting in global warming. South Africa is regarded as the seventh largest coal exporting country in the world. The coal-generated energy produced in South Africa contributes an appreciable amount to global climate change, thus the South African government has acknowledged the need for a sustainable energy mix, and it has recognised renewable energy (RE) sources as a reliable candidate for reducing the energy crisis and GHG emissions [1.1, 1.2].
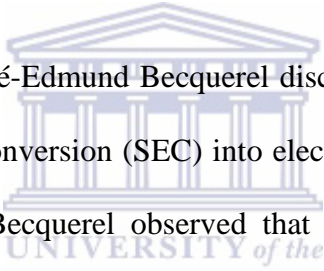
The use of RE sources offers an alternative to the growing global energy demand and the impacts of climate change. There will be a high demand for clean RE sources in the coming decades due to the increasing inaccessibility and price of natural fossil fuels. Of the various energy sources, which include hydro, biomass, wind, geothermal, and solar energy is the most naturally abundant energy resource. South Africa has one of the highest solar capacities in the world with the annual solar direct nominal irradiation (DNI) being the highest [1.2, 1.3].

Since ancient times, solar energy has been a significant source of energy. The industrial age marked the discovery of sunlight as an energy source. On average, the sun supplies the Earth's surface with about 1.2×10^{17} Watts (W) of solar power. This means that the

energy radiated in less than an hour (hr) could meet the energy demands of the human population for an entire year. Other renewable means of generating power that also depend on the sun include hydroelectric, wind and wave power. Conversion of solar energy to electricity by means of photovoltaic (PV) technology is recognised as reliable energy sources to minimise the significant impact of GHGs in the atmosphere and to lessen global warming [1.1].

1.2 Photovoltaic Solar Energy

1.2.1 Background

As far back as 1839, Alexandré-Edmund Becquerel discovered the PV effect, which is based on direct solar energy conversion (SEC) into electricity by PV cells, also termed solar cells (SCs) [1.4, 1.5]; Becquerel observed that certain light-induced chemical reactions produced electricity. In the SEC process, incident light energy creates moving charged particles in a semiconductor; these particles are then separated by the structure of the device in order to produce electricity [1.1]. However, it was not until the mid-1950s that the PV effect awakened curiosity amongst scientists in laboratories, although it had few practical uses at the time. The real revolution only occurred during the American space program, starting with America's Vanguard I in 1958, which initiated the practical use of Si SCs in scientific, commercial and military satellites launched by various space organisations [1.4].

PV devices are simple in design and do not require any heat engine. Their main advantage is their ability to give outputs ranging from microwatts (µW) to megawatts (MW) as stand-alone systems. PVs are employed in power sourcing, water pumping,

remote buildings, solar home systems, communications, satellites, space vehicles, reverse osmosis plants, and MW-scale power plants [1.5]. PV systems are prepared from semiconductors and are similar in construction to other solid-state electronic devices such as diodes, integrated circuits (ICs), and transistors. PV modules have production efficiencies approaching 18% and a long lifetime of 20 years [1.1].

1.2.2 Intrinsic and Extrinsic Semiconductor Materials

The band gap (E_g) of a material characterises materials into semiconductors, conductors and insulators. The band gap is an important property of materials, as it controls the functionality of a SC. Insulators, such as glass, have a broad band gap, viz. a value of 2 electronvolts (eV), while a conductor or a metal has an overlapping band gap, A semiconductor has a band gap between that of a conductor and an insulator in the range of 0.5 to 3 eV [1.6].

In an intrinsic semiconductor (i.e. a pure semiconductor), the valence band (VB) is completely filled with sufficient electrons (e's), whereas the conduction band (CB) is completely empty (see Figure 1.1 (a)). Since the VB is completely filled, the electrons in this band are unable to move. One way in which semiconductors can become conductive is either to introduce carriers into the CB or to remove carriers from the VB [1.1]. This procedure, in which the semiconductor is alloyed with impurities, is known as doping [1.1, 1.7].

Semiconductors that are comprised of impurity atoms are called extrinsic semiconductors [1.8]. If for instance, some impurity atoms of a group V element (e.g. phosphorus (P)) are added to silicon (Si), only four electrons are used to fill the VB. The one remaining electrons from each impurity atom is enhanced to the CB (see also

Figure 1.1 (b)). These impurity atoms from the CB are mobile and are called donors. At this point, the semiconductor becomes a conductor. This type of semiconductor is referred to as n-type since the negatively charged electrons contribute to the electrical current [1.1, 1.8].
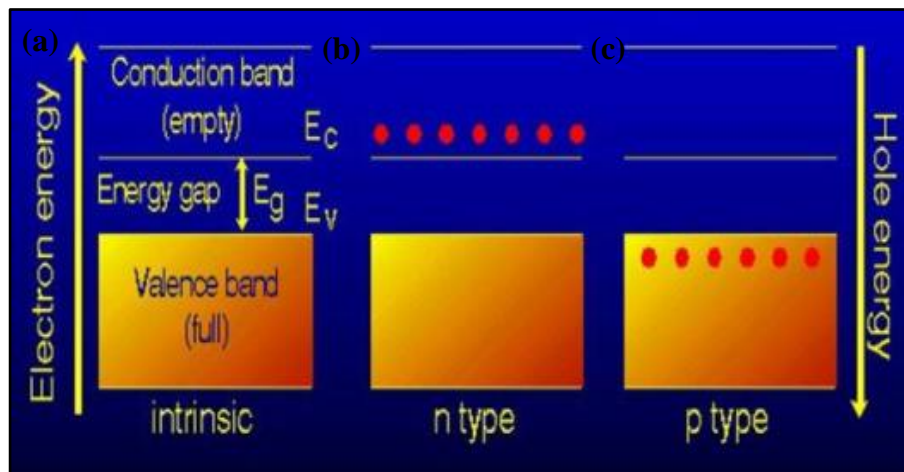
Figure 1.1: Band diagram and electron-hole distribution in semiconductors. (a) Intrinsic semiconductor and (b) and (c) n-type and p-type semiconductors, respectively [1.9].

Similarly, if some impurity atoms of a group III element (e.g. Boron (B)) are doped with Si, a deficiency of electrons is created within the VB, since four electrons per atom are required to fill this band completely. These atoms are called acceptors (see also Figure 1.1 (c)). The absence of an electron is called a hole (*h*); this is mobile and contributes to the electrical current. A semiconductor that holds more holes than electrons is called p-type since holes are positively charged. In an n-type semiconductor, the majority and minority carriers are electrons and holes, respectively. In contrast, for p-type semiconductors, the majority and minority carriers are holes and electrons, respectively [1.1, 1.8].

4

1.2.3 Semiconductor Junctions

The basic operation of a SC is centred on the formation of a junction [1.1]. Figure 1.2 presents various types of junctions.
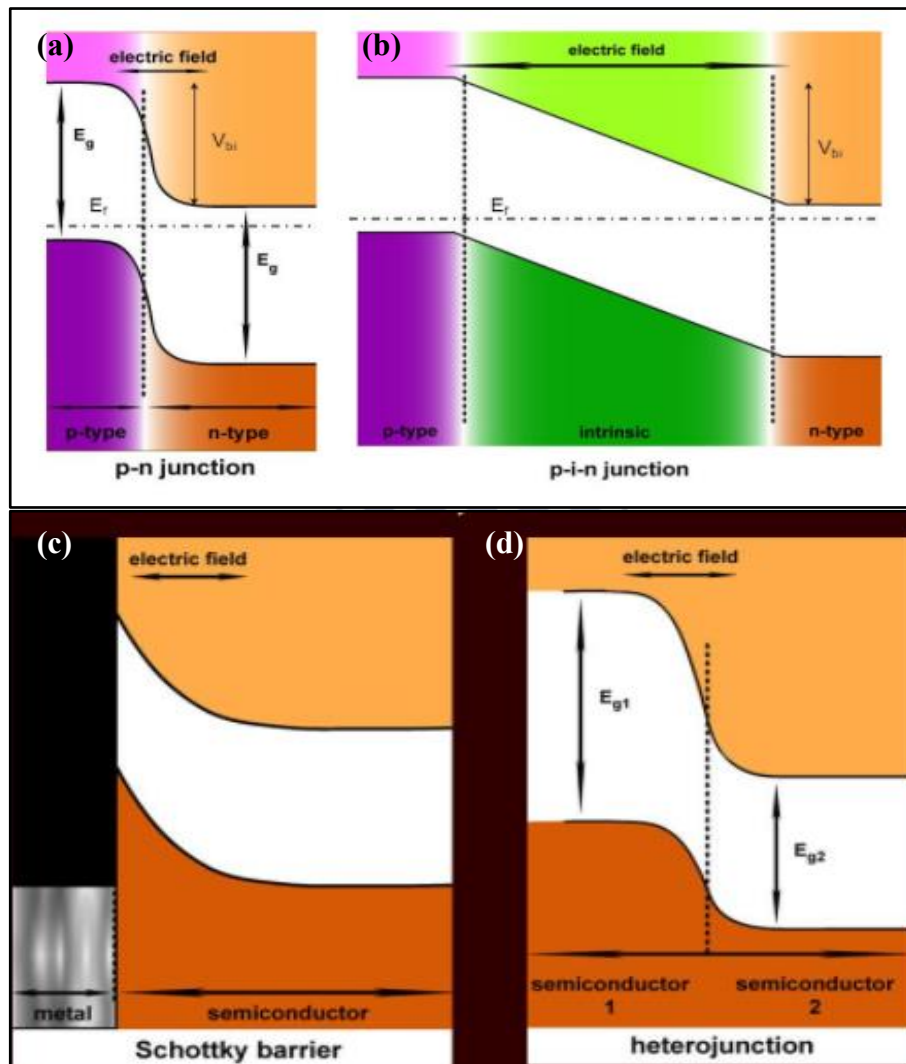
Figure 1.2: Band diagram of semiconductor junctions: (a) and (b) the p-n and p-i-n junction, respectively; (c) and (d) Schottky and heterojunction, respectively [1.10, 1.11].

When two semiconductor materials are brought into contact (i.e. an n-type and a p-type material), a strong electric field (**E**) is formed pulling the electrons and holes in opposite directions. In separation, there are more electrons and more holes in an n-type and a p-

type material, respectively. When the two materials are brought together, the electrons near the interface from the n-side diffuse to the p-side, leaving behind positively charged ions by the donors. Similarly, holes diffuse to the n-side, resulting in a layer of electrons on the p-side [1.1]. If there is no external source, the diffusion process cannot go on repeatedly [1.8]. The junction region contains immobile charge carriers and the fixed charges of the dopant atoms further restrict [i.e. 'the charges restrict'] the movement of both electrons and holes, creating a potential barrier [1.1].

The p-n junction (Figure 1.2 (a)), possibly the simplest type, is an interface between the n and p regions of a semiconductor. In addition, a layer of intrinsic material is embedded between the n-and p regions, resulting in a broader transition zone; the resultant junction is called a p-i-n junction (Figure 1.2 (b)). These are labelled as homojunctions. A Schottky barrier, an interface between a metal and a semiconductor, also forms a junction (Figure 1.2 (c)). Conversely, heterojunctions (Figure 1.2 (d)) are formed between two different semiconductors that have different band gaps [1.1].

1.3 Silicon for Photovoltaic Applications

1.3.1 Introduction

Si is the most commonly used material in commercial SC modules, accounting for $\approx$ 90% of the PV market. As a result, Si PVs are employed due to their special features such that (1) Si is abundant (Si is the second most abundant element on Earth), (2) Si is typically stable and non-toxic, (3) The band gap of Si (1.12 eV) is nearly perfectly matched to the terrestrial solar spectrum, and (4) Si PVs are readily well-suited to the modern Si-based microelectronics industry [1.3]. Even though pure Si does not occur in

nature, 60% of the Earth's crust is composed of sand, mostly in the form of quartzite or silicon dioxide (SiO_2) [1.1].

The principles of semiconductor physics are best demonstrated by using Si, a group 4 semiconductor element, as an example. The crystal structure of Si is the so-called *diamond lattice*, where each Si atom has four nearest neighbours at the vertices of a tetrahedron. The four-fold tetrahedral coordination is a consequence of the bonding arrangement that uses the four valence electrons (i.e. outer electrons) of each atom. Figure 1.3 shows the *diamond lattice* four-fold tetrahedral coordination of Si. Each bond is comprised of two electrons, in which all the valence electrons are taken up by the bonds [1.1].
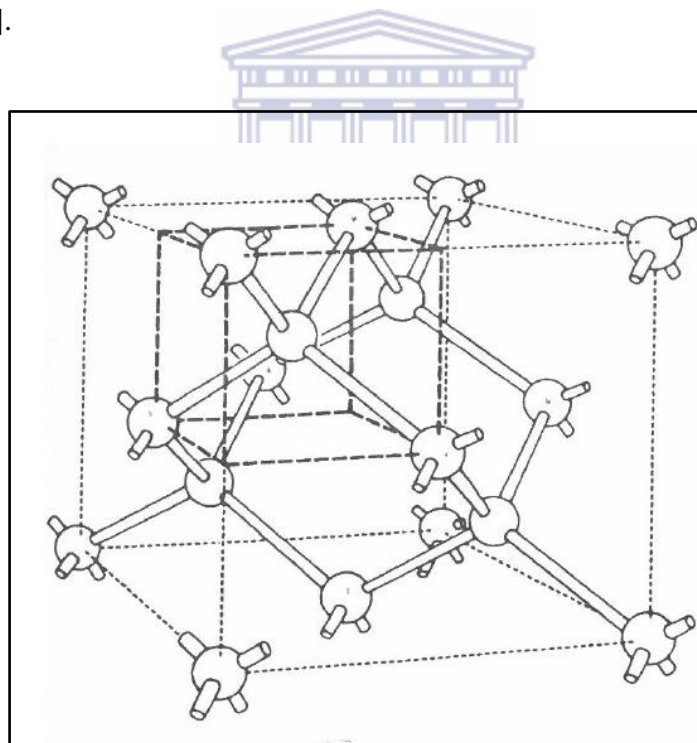
Figure 1.3: The Si *diamond lattice* [1.1].

1.3.2 Generations of Silicon Solar Cells

Wafer-based Si SCs are acknowledged as first generation SCs [1.4], whereas second-generation SCs are based on thin film technologies [1.6]. The efficiency of typical

7

monocrystalline Si SC modules lies between 17 and 18% [1.4]. The efficiency of typical poly-crystalline SC modules is roughly 15 to 17%, about 1% lower than monocrystalline cells, manufactured within similar production lines [1.12]. The focus of this study is on the use of monocrystalline Si as a starting material.

1.3.3 Monocrystalline Silicon Solar Cell

The monocrystalline production process comprises various steps. Firstly, metallurgical grade silicon (MGS) with purity in the range of 98 to 99% is produced, after melting carbon (C) (found in coal and coke) and quartzite (SiO_2) at operating temperatures above 1800 degree Celsius (°C) according to the reduction process demonstrated by Equation (1.1) [1.13]:

$$SiO_2 \text{ (s)} + 2C \text{ (s)} \rightarrow Si \text{ (ℓ)} + 2CO \text{ (g)} \tag{1.1}$$

Polycrystalline Si is a result of further purification, in which purities higher than 99.999999% may be achieved. MGS is changed to trichlorosilane ($HSiCl_3$) by using hydrogen chloride (HCl) according to the exothermic process demonstrated by Equation (1.2) [1.13]:

$$Si \text{ (s)} + 3HCl_3 \text{ (g)} + H_2 \text{ (g)} + \text{heat} \tag{1.2}$$

The purity is further enhanced through a sequence of distillation steps. Thereafter, the Siemens process is employed to reduce $HSiCl_3$ thermally under a hydrogen (H) atmosphere to deposit polycrystalline Si by means of chemical vapour deposition (CVD), according to the process described in Equation (1.3). This results in Si being deposited on high purity Si rods [1.13].

$$SiHCl_3 \text{ (g)} + H_2 \text{ (g)} \rightarrow Si \text{ (s)} + 3HCl \text{ (g)} \tag{1.3}$$
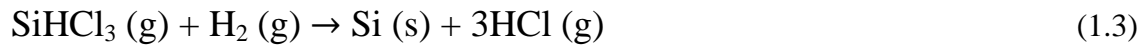
The crystallisation processes continue with the use of the polycrystalline Si described above to produce Si wafers. Some methods include the Czochralski (Cz) and the Float-zone (FZ) processes. These methods produce high-quality monocrystalline Si (see Figure 1.4). Because of the lower Si purity, polycrystalline SCs are not as efficient as monocrystalline SCs [1.13].

Figure 1.4: Typical Mono crystalline Si SC [1.14].

The need for large quantities of high-purity Si materials explains the high cost of Si SCs. The immense increase in the demand for raw Si material in recent years has inflated the price. Even though monocrystalline Si is expensive to manufacture, its good electrical properties allow it to be exploited by the introduction of advanced cell processing [1.13]. The focus of this study is on the use of monocrystalline Si as a starting material.

1.4 Nanostructured Materials for Photovoltaic Applications

1.4.1 Introduction

The high cost of wafer-based Si has resulted in a low mass distribution of Si SCs, hence much attention has been focused on developing new unconventional SCs to create low-cost and high-performance SCs. Of particular interest are nanostructured materials, including nanocrystals (also known as quantum dots and nanoparticles), nanorods (also known as nanopillars), nanotubes, and nanowires (NWs); their novel properties make them excellent for use in PV design applications, such as strong light absorption, due to their large surface areas [1.3].

1.4.2 Silicon Nanowires

Si nanostructures, such as silicon nanowires (Si NWs), continue to demonstrate superior properties to their bulk counterparts, with respect to their morphology and energetic features. For this reason, researchers are driven to explore controllable fabrication methods of Si nanostructures and their applications [1.15]. NWs along with nanorods and nanobelts form part of the one-dimensional (1D) nanostructures [1.16]. NWs are hair-like 1D nanomaterials with diameters of a scale of sub-one hundred nanometres (nm) and lengths in the range of more than a few hundreds of nm to a few micrometres (μm) [1.17].

Research on Si NW-based PVs is still in its early stages [1.18]. The ability of NWs to be incorporated into electronic devices [1.16], their ability to trap light [1.19 - 1.22], along

with many other properties, allow this semiconductor NWs to be utilised in many device applications [1.16], such as PVs, electronics, thermoelectrics, and biological sensors [1.19 - 1.22].

1.5 Photovoltaic Devices Based on Silicon Nanowires

1.5.1 Radial p-n Junction Silicon Nanowire Photovoltaic Devices

The fascinating theoretical results on radial p-n junction assemblies (i.e. coaxial core/shell NWs) have driven scientists to develop Si NW-based PV devices of this sort. Each NW consists of a p-type Si wire core, and an n-type Si layer shell, producing radial p-n junction geometry. Figure 1.5 shows a radial p-n junction Si NW SC by means of P dopant diffusion. Worthy characteristics of radial p-n junctions include their short travel distances of photoexcited minority carriers to the collection electrodes causing increased carrier collection efficiency and minimum bulk recombination [1.3].
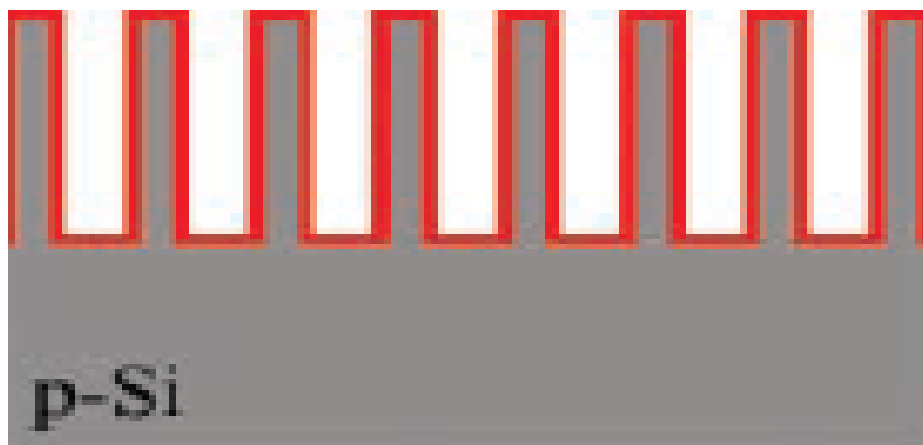
Figure 1.5: Radial p-n junction Si NW SC through P dopant diffusion. Shown in red is the n-type Si shell [1.3].

1.5.2 Axial Homojunction Silicon Nanowire Photovoltaic Devices

The radial and axial p-n junction NWs are two structural geometries employed for application in PV devices. Both the radial and axial p-n junction NWs adopt the same device physics. For an axial p-n junction NW structure, the photoexcited electron-hole pair (the *e-h* pair) separates at the depletion region due to the built-in field that can be recognised in the axial direction. In contrast to the radial p-n junction NW configuration, the carriers have to travel a longer distance along the wire direction to the collection electrodes [1.3].

1.5.3 Photovoltaic Devices Based on n-Silicon Nanowires Grown on a p-Si substrate

A p-n junction is formed between a p-type Si wafer and n-type Si NWs. These cells show poorer carrier collection abilities than the radial p-n junction. In 2008, Stelzner and co-workers synthesised n-type Si NWs on the p-type Si wafer by means of the vapour-liquid-solid (VLS) method. Under Global Air Mass 1.5 (AM 1.5) illumination, the device exhibited an open-circuit voltage (V_{oc}), short circuit current density (J_{sc}), overall conversion efficiency (η) and fill factor (FF) of 230 to 280 millivolt (mV), 2 milliampere per square centimetre (mA/cm^2), 0.1% and 0.2, respectively [1.3].

1.5.4 Photovoltaic Device Based on a Silicon Nanowire Schottky Metal/Semiconductor Junction

Currently, researchers at Caltech have developed a single-junction Si NW SC device, by depending on the metal/semiconductor rectifying contacts (see Figure (1.6)) that were

12

selectively introduced underneath Aluminium (Al) contacts to Gold (Au)-catalysed wires, by joule heating a piece of the wire. Figure 1.6 shows a dark current-voltage (I-V) measurement of a single Si NW diode device with a 900 nm diameter. The downward-facing arrows points towards the two inner contacts and the upward-facing arrows show adjacent upper contacts from which a rectifying junction was formed by sourcing current between the upper contacts until the enclosed wire segment was destroyed [1.3].
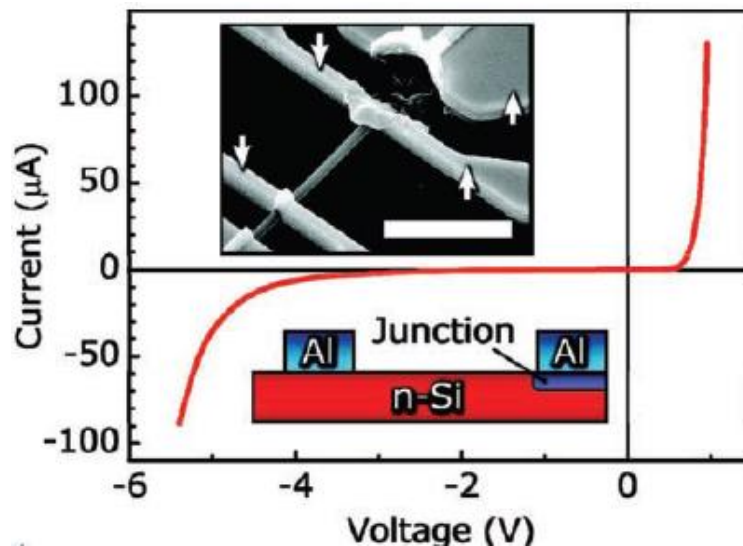
Figure 1.6: Silicon nanowire schottky metal/semiconductor junction. Inset: 45° view scanning electron microscopy (SEM) micrograph. Scale bar: 10 μm [1.3].

1.6 Fabrication Techniques of Silicon Nanowires

1.6.1 Introduction

There are two general methods of fabricating Si NWs, viz. the bottom-up approach and top-down approach. The bottom-up approach can be seen as a building process, in which Si atoms are fitted together to create a Si NW array. This approach includes growth processes such as the VLS, oxide-assisted growth (OAG), supercritical-fluid-

based, and solution-based processes, amongst other methods. The most well-known bottom-up approach is the CVD, which uses the VLS mechanism. The fabrication of Si NWs by means of the conventional Au-catalysed VLS growth process involves (1) the decomposition of a Si precursor on a metal catalyst, (2) creation of the Si-metal liquid alloy, (3) Si distribution into the Si-metal alloy droplet, and (4) Si precipitation to produce Si NWs from the droplet upon Si supersaturation [1.3].

In contrast, the top-down approach forms Si NWs by reducing the dimensions of bulk Si by means of lithography and etching. This approach is capable of fabricating Si NWs with diameters in the range of tens to hundreds of nanometers through electron beam lithography, reaction ion etching (RIE), and the metal-assisted chemical etching (MaCE) of Si. In contrast to the conventional bottom-up approach, the MaCE fabrication method is a potentially low-cost alternative of producing Si NWs high surface-to-volume ratio, vertically-aligned and wafer-scale in size [1.3]. The MaCE method is thus of particular interest in this study. Furthermore, MaCE is a simple, low-temperature, a scalable and fast method to synthesise Si NWs [1.3, 1.23]. Since MaCE-grown Si NWs are vertically-aligned with diameters in the range of 20 to 300 nm, they have desirable electrical properties and growth orientations; moreover, they are synthesised from the bulk Si wafer, hence they are of interest in this study. In the next section, we thus outline some of the Si NW growth methods, which use bottom-up and top-down approaches [1.3].

1.6.2 Bottom-Up Fabrication Techniques

1.6.2.1 Chemical Vapour Deposition

The VLS process is a well-known method capable of producing dense, high surface-to-volume ratio, vertically aligned Si NWs. In the CVD-VLS process, Au or any other appropriate metal acts as the catalyst that assists in the growth of Si NWs. The gaseous Si reactants are provided by Si gaseous precursors such, as Silane (SiH_4) or Si tetrachloride ($SiCl_4$). Figure 1.7 summarises the VLS-CVD growth technique [1.3].
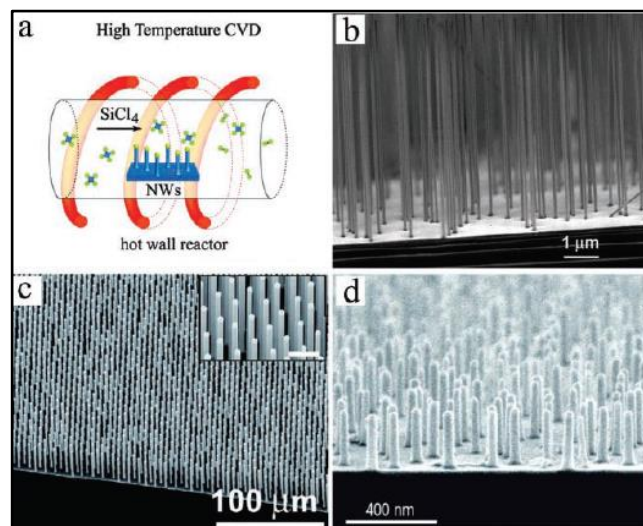
Figure 1.7: (a) Schematic representation of a high-temperature CVD set-up. (b) A SEM cross-sectional micrograph of Si NWs grown from Au colloids. (c) A tilted SEM micrograph of Cu-catalysed Si NWs across a large area (> 1 cm^2). (d) A SEM cross-sectional micrograph of Al-catalysed Si NWs on a Si (111) wafer grown at a temperature of 430 °C [1.3].

Uniform Si NWs can be fabricated with a diameter of 3 nm using SiH_4 as the precursor and H_2 as the carrier gas. H_2 softens radial growth of Si NWs either by Si reactant absorption, by terminating the Si surface or by dissociation of SiH_4. The changeability

in Si NW growth using $SiCl_4$ as the precursor is a result of using HCl as a by-product of $SiCl_4$ decomposition, which ultimately etches the surface oxide of Si to form a clean Si surface for Si precipitation from the binary liquid droplet [1.3].

1.6.2.2 Oxide-assisted growth

Another vapour-phase NW formation mechanism is the oxide-assisted growth (OAG) technique. Through synthesis and optical characterisation, it was found that NWs created with gallium arsenide (GaAs) NWs exhibited lengths of up to tens of micrometres, and that a diameter in the range of 10 to 120 nm or an average diameter of about 60 nm can be achieved. The NWs consist of a GaAs core with a crystalline <111> growth direction covered with a thin oxide layer. This growth technique is also used to grow Si NW. Si NW growth is improved if SiO_2 with Si powder targets are used. By mixing 30 to 70% SiO_2 into the Si powder target, dense Si NWs can be obtained through laser ablation. The key factor in the proposed OAG mechanism is the generation of the vapour phase of Si_xO ($0 < x > 1$) by thermal evaporation or laser ablation [1.25].

1.6.3 Top-Down Fabrication Techniques

1.6.3.1 Reactive Ion Etching

Reactive ion etching (RIE) is a technique utilised for standard Si micro-/nanofabrication that produces a large area of vertically and horizontally uniformly grown Si NWs from the bulk Si wafer. Another technique, electron beam lithography, is commonly used to form sub-ten-nm patterns. However, this technique is time-consuming and expensive. Advanced lithography techniques, including photolithography, nanosphere lithography

and nanoimprint lithography are used to improve the standard RIE Si micro-/nanofabrication technology. This popular technique is widely used to fabricate vertically aligned orderly Si nanopillars on Si wafers, although it is challenging to achieve high surface-to-volume ratio Si NWs through etch-mask erosion. Si NWs produced by a combination of RIE and the lithography technique exhibit ordered arrays of <100>-orientation with controlled size, density, and electronic properties [1.3].

1.7 Metal-assisted Chemical Etching of Silicon

1.7.1 Introduction

In this study, the MaCE fabrication technique is employed to synthesise vertically aligned Si NWs. MaCE is a top-down method developed to fabricate Si nanostructures with the aim of controlling the parameters, such as cross-sectional shape, diameter, length, orientation, doping type, and doping level of Si nanostructures. Over the past few years, MaCE has become a key fabrication technique for Si or Si/Germanium (Ge) nanostructures. These structures have proved their potential in various applications, such as biomimetic superhydrophobicity, biological and chemical sensing, energy storage, solar energy conversion, and thermal power conversion. The benefits of using the MaCE fabrication technique includes [1.23]:

- It is a simple and low-cost method of fabricating various Si nanostructures.

- It is possible to control parameters, such as shape, diameter, doping level, doping type, length, and orientation of the nanostructures.

- It is a flexible method and enables high surface-to-volume ratio structures.

- There is no recognisable limitation in the size of the features.

Despite all these positive aspects, the MaCE technique has not yet been fully studied or understood.

1.7.2 Methods and Mechanisms

1.7.2.1 Formation Mechanism of Silver Nanoparticles

Numerous coating solutions containing noble metal ions may be used to coat noble metals electroless onto a Si wafer. The coating solution is typical of a galvanic process. MaCE process includes two steps: firstly, a metal catalyst is coated onto the wafer surface, which precedes the anisotropic etching in an oxidant/hydrofluoric acid (HF) solution. During the initial stages of the metal coating, silver ions (Ag^+ ions) in the presence of the Si surface extract electrons from Si to form negatively charged Ag nuclei (i.e. nucleation). The Ag^+ ions moving towards the Si surface acquire electrons from the Ag nuclei and localise around them rather than on the uncovered Si, leading to Ag nuclei growing into larger particles as more Ag ions approach [1.22 - 1.23, 1.26].

1.7.2.2 Formation Mechanism of Silicon Nanowires

It is suggested that, during the etching process, the Silver nanoparticles (Ag NPs) act as the cathodes on which the reduction of the oxidant takes place. The Si underneath the Ag NPs acts as the anodes and is oxidised due to hole injection to form SiO_2 and at the same time, SiO_2 is dissolved by HF, forming shallow 'craters' underneath the Ag NPs. The Ag NPs are effectively maintained in their original state, and they gradually sink vertically downwards. The on-going sinking of Ag NPs results in the etching of Si that is in contact with the Ag NPs. As the process progresses, Ag NPs continues to sink

vertically downwards at the etched regions to form vertically aligned Si NWs [1.23, 1.27].

The approved method is that the chemical or electrochemical reactions should preferably take place near the noble metal particle. Several cathode and anode reactions are generally recommended for the etching process. The cathode and anode reactions of the etching process shown below explain one of the few proposed models in the literature [1.27].

Cathode reaction:

It is approved that the oxidant (for example hydrogen peroxide (H_2O_2)) is reduced at the metal, such that:

$$H_2O_2 + 2H^+ \rightarrow 2H_2O + 2h^+ \tag{1.4}$$

Anode reaction:

The anode reaction involves the oxidation and dissolution of the Si wafer. Si oxide formation is followed by dissolution of the oxide, such that:

$$Si + 2H_2O \rightarrow SiO_2 + 4H^+ + 4e^- \tag{1.5}$$

$$SiO_2 + 6HF \rightarrow H_2SiF_6 + 2H_2O \tag{1.6}$$

1.7.2.3 The Overall Etching Process

Figure 1.8 presents a schematic representation of the proposed etching process in the MaCE fabrication technique. The following steps summarise the proposed etching process [1.23]:

19

1. The oxidant is reduced at the surface of the noble metal due to the catalytic activity of the noble metal on the reduction of the oxidant.

2. The holes are diffused due to the reduction of the oxidant. Subsequently, the holes move through the metal and are introduced into the Si that is in contact with the noble metal.

3. Si is oxidised due to the introduction of holes, and it is dissolved at the Si/metal interface by HF. The reactant (HF) and the by-products diffuse along the Si/metal interface.

4. The hole concentration is dominant at the Si/metal interface, which suggests that Si in the presence of a noble metal is etched much faster by HF than would be the case on a Si surface without metal coverage.

5. Holes diffuse from the Si underneath the noble metal to off-metal areas or to the wall of the pore, if the rate at which the holes are consumed at the Si/metal interface is less than the rate at which holes are introduced. Accordingly, the off-metal sections or sidewalls of the pore may possibly etch and result in microporous Si as in a case of electrochemical or stain etching.
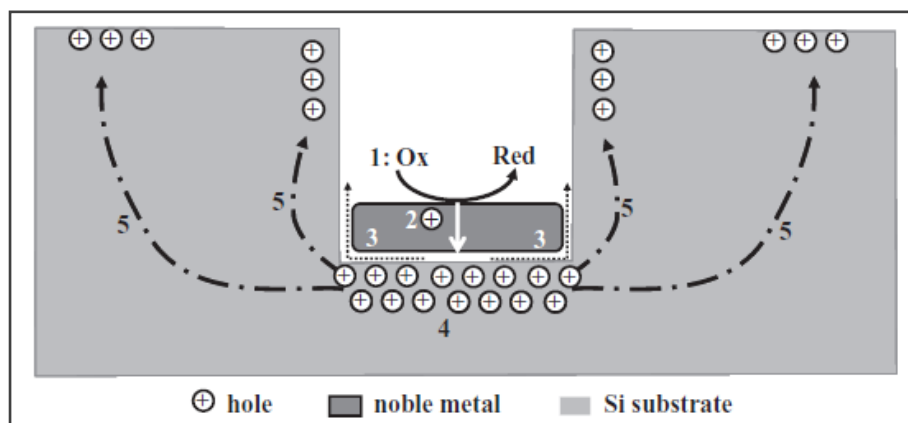

Figure 1.8: Schematic representation of the proposed processes involved in MaCE. The numbers indicate the steps mentioned in this section [1.23].

20

1.8 Properties of Silicon Nanowires

1.8.1 Electrical Transport Properties

Properties of NWs, such as the chemical composition, diameter, doping level, growth direction, and surface-to-volume ratios influence the electrical characteristics of devices [1.28]. Electrical transport properties of Si NWs, such as n- or p-type conducting, are imperative for producing functional electronic devices, such as field-effect transistors (FETs) and SCs [1.3].

Si NWs are known to be quantum wires since they show quantum confinement effects. The quantum confinement effects in Si NWs influences the band gap and the effective mass (m^*) of the carriers. The change in the band gap of Si NWs and effective mass of carriers depend on surface termination of the NWs. Theoretical studies show that the effective mass reduces from 0.47 to $0.31 m_e$ with increasing Si thickness from 1.6 to 3.2 nm for hydrogenated-terminated NWs. In contrast, the effective mass reduces from 0.36 to $0.29 m_e$ with the same Si thickness for SiO_2 terminated Si NWs. The same study showed that the band gap was enhanced from 1.56 to 2.44 eV and from 1.50 to 1.88 eV when the Si thickness decreased from 1.6 to 3.2 nm for hydrogenated and SiO_2 terminated Si NWs, respectively [1.28].

The addition of dopants or impurities changes the electrical transport properties of Si NWs. The addition of pentavalent dopants such as P, arsenic (As) and antimony (Sb) results in n-type semiconducting NWs, in which electrons are the majority charge carriers. In contrast, the addition of trivalent dopants such as B results in p-type semiconducting NWs, in which the majority charge carriers are holes. The doping level

regulates the density of states (DOS) in the NWs. A theoretical value of 10^{13} $1/cm^2$ was obtained for a doping level of 10^{20} $1/cm^3$ for p-type and n-type NWs [1.28].

The dopant concentration (N_D) has an influence on the charge carrier mobility (μ) of bulk Si such that it decreases with enhanced impurity concentration. This is attributed to scattering centres of charge carriers created by ionised impurity atoms [1.28]. Significant work has been put into increasing the mobility of Si NWs to improve device performance [1.3]. The mobility value obtained experimentally enhanced from 95 to 250 cm^2/Vs with reduced P concentration in n-doped Si NW FETs. Thermal annealing and passivating surface defects through chemical modification showed improvement in the carrier mobility. An average mobility of 30 to 560 cm^2/Vs was achieved after surface treatment [1.28].

1.8.2 Optical Properties

The focus of most work in the literature has been on understanding light emissions in Si NWs, rather than on understanding the practical application of Si NWs in light emitting devices. Even though mechanisms such as quantum confinement effects and surface state or defects in SiO_x have been suggested, there has been a limited study of the basis of light emission [1.15].

Etching conditions during non-lithographic patterning and MaCE of Si, such as etchant concentration, doping level and orientation and an etching time of Si, have an influence on optical properties. The light emission in the whole visible range and in the near infrared range that is seen in all the samples is independent of etching conditions. However, as can be seen in Figure 1.9, solid vertically-aligned Si NWs (Figure 1.9 (a)) showed stronger emission in the blue spectrum (~ 470 nm) (Figure 1.9 (c)), as opposed

to porous slanted Si NWs (Figure 1.9 (b)), which showed stronger emissions in the red spectrum (624 nm) (Figure 1.9 (c)) [1.15].

A remarkable observation has been found in Si NWs with diameters of 1000 nm (Figure 1.9 (d)-top micrograph) and 400 nm (Figure 1.9 (d)-bottom micrograph). The Si NWs with different diameters showed comparable emission wavelengths (λ) and intensities. Both of these diameters are far larger than the quantum confinement threshold (~ 5 nm). Hence, it was suggested that the visible emission is due to surface morphology [1.15].
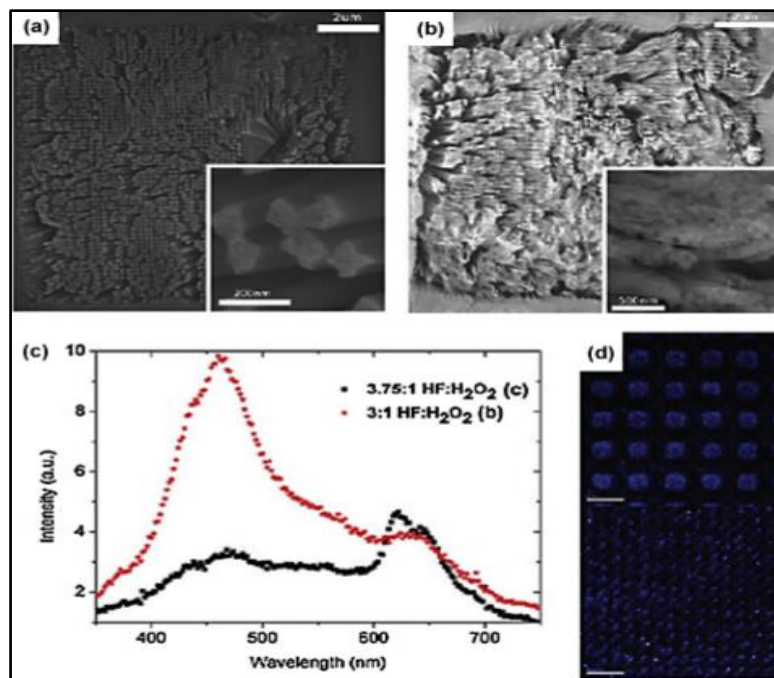
Figure 1.9: Top-view SEM micrographs with corresponding higher magnification micrographs of (a) solid vertically-aligned Si NWs and (b) porous slanted Si NWs. (c) PL spectra of the solid vertically-aligned Si NWs and porous slanted Si NWs indicative of the red and blue squares, respectively. (d) Faux colour PL micrographs at a wavelength of 470 nm from the Si NWs with a diameter of 1000 nm (top micrograph) and 400 nm (bottom micrograph) [1.15].

The main experiment performed was to investigate the SiO_x-based interface state before and after HF treatment. A collective study of optical and transmission electron microscopy (TEM) characterisation, revealed that the quantum confinement effect due to nanostructures at the rough sidewall seemed to be the reason of the photoluminescence (PL) rather than SiO_x-based interface states. The intensity of the PL peak enhanced and shifted to red wavelength with increasing porosity. Also, the PL spectrum was deconvoluted into two peaks positioned at 750 nm and 850 nm. According to Fourier-transport infrared spectroscopy (FTIR) studies, the 750 nm and 850 nm PL peaks are related to Si-O and $Si-H_x$ bonds, respectively [1.15].

This result confirms that there are two phenomena of light emission. In other words, the 750 nm peak originates from surface-oxidised nanostructures and the 850 nm peak originates from nano-porous structures. Increasing surface Si-O bonds and porosity result in enhanced light emission intensity. They also suggested that the Si-O bonds and self-trapped excitations in nano-porous structures cause the strong emission [1.15].

1.9 Aim and Outline of Thesis

The burning of fossil fuels for electricity generation is recognised as an environmental problem since it is affecting the Earth's atmosphere by causing global warming [1.1, 1.29]. However, given increased efforts to control the emissions of CO_2 produced from fossil fuels, it is likely that RE sources, including PVs, will become more important in generating electricity in the future [1.29]. The most popular solar PV modules sold are Si-based, but in recent years, an increased need for Si SCs has inflated the price of raw Si materials. The scarcity of high-quality Si materials has led researchers to seek alternative means of producing Si-based PV cells by using novel materials that are

inexpensive [1.30]. Si NWs have appeared as a promising candidate for PV application. Vertically-aligned Si NWs synthesised by means of the MaCE fabrication technique can be used as a low-cost solution for PV applications. Si NWs are becoming more attractive due to their novel optical and electrical transport properties compared to their bulk counterparts. The important role of vertically-aligned Si NWs is to minimise effective losses in PV devices [1.31].

In this study, n-doped Si NWs are synthesised from p-type MaCE-grown Si NWs using a phosphorus (P)-containing spin-on dopant (SOD) by means of a post-deposition technique. There is a lack of understanding and a lack of resources with regard to the exact explanation of the diffusion mechanism involved when applying SODs to MaCE-grown Si NWs. Hence, it is the intention of this study to add to the understanding of the effects of n-type doping on MaCE-grown Si NWs by this method. For this purpose, an investigation will be conducted into the following effects:

- The effect of the Ag catalyst morphology on the MaCE-grown Si NWs by using the scanning electron microscopy (SEM) characterisation technique.

- The effect of n-type doping on the MaCE-grown Si NWs using the SEM and the transmission electron microscopy (TEM) characterisation technique.

- Evaluate whether the MaCE-grown Si NWs and n-doped Si NWs maintained the original characteristics of the bulk single-crystalline (100) Si wafer using the TEM and the X-ray diffraction (XRD) characterisation technique.

- The composition of n-doped Si NWs using the X-ray photoelectron spectroscopy (XPS) technique, and

- The electrical transport properties of the n-doped Si NWs using the Hall effect measurement technique.

The outline of this thesis is as follows:

Chapter One presented some background on the importance of moving away from the use of fossil fuels to the use of using RE for electricity generation. The theory of using Si and Si NWs for PV application was introduced, as were the various types of PVs based on Si NWs, the various techniques of fabricating Si NWs, and the properties of Si NWs.

Chapter Two will provide a comprehensive fundamental understanding of phosphorus (P) diffusion, which includes some background of the spin-on doping process, the atomic mechanism of diffusion, and the mechanism of the post-deposition doping of Si NWs that is proposed for this study, and the diffusivity and solid solubility of P in Si.

Chapter Three will give comprehensive descriptions of the evolution of the experimental techniques that were ultimately used to produce the n-doped Si NWs. This specifically includes the synthesis of the Si NWs by using MaCE, the spin-on doping experimental procedure and the thermal annealing procedure. Also, the emphasis of this chapter will be on the fundamental physics, the preparation of the samples, and the data acquisition within the respective analytical techniques used to characterise the various samples.

Chapter Four will discuss the results of this study, in particular, the effects of the initial morphology of the Ag NPs on the resultant etched structures (i.e. the MaCE-

grown Si NWs) and the effects of n-type doping on the morphological, structural, compositional, and electrical transport properties of the MaCE-grown Si NWs.

Chapter Five will conclude this study by providing the conclusions, suggesting future work that could be implemented in this field and by making recommendations to improve this study.

1.10 References

[1.1] Markvart, T. (Ed.). (1992). Solar Electricity (2nd ed.). England: John Wiley & Sons.

[1.2] Nakumuryango, A. and Inglesi-Lotz, R. (2016). South Africa's performance on renewable energy and its relative position against the OECD countries and the rest of Africa. Renewable and Sustainable Energy Reviews, 56, 999.

[1.3] Peng, K. and Lee, S. (2011). ChemInform Abstract: Silicon Nanowires for Photovoltaic Solar Energy Conversion. ChemInform, 42(14), 198.

[1.4] Hill, R. (Ed.). (1989). Applications of Photovoltaics. England: IOP Publishing Ltd.

[1.5] Parida, B., Iniyan, S. and Goic, R. (2011). A review of solar photovoltaic technologies. Renewable and Sustainable Energy Reviews, 15(3), 1625.

[1.6] Ngqoloda, S. (2015). Vertically aligned silicon nanowires synthesised by metal assisted chemical etching for photovoltaic applications. MSc thesis. University of the Western Cape.

[1.7] Kittel, C. (Ed.). (2005). Introduction to Solid State Physics. (8th ed.). United States of America: John Wiley & Sons.

[1.8] Neamen, D.A. (Ed.) (2003). Semiconductor Physics and Devices: Basic Principles. (3rd ed.). United States: McGraw-Hill Companies, Inc.

[1.9]Anon,(2016).[online]Availableathttp://electronicsgurukulam.blogspot.co.za/2012/09/a-simple-analogy-to-band-theory-in.html. [Accessed 20 Feb. 2016].

[1.10] Anon,(2016). [online] Available at: http://slideplayer.com/lide/7386194 [Accessed 20 Feb. 2016].

[1.11] Slideplayer.com. (2016). Solar Photovoltaic Physics - ppt download. [online] Available at: http://slideplayer.com/slide/4661849. [Accessed 18 May. 2016].

[1.12] Sidhu, R., Carlson, D.E. (2010). Bp solar. Crystalline Silicon Solar Cell Technology. [online] Available at: bpsolarsidhu_4_13_2010 [Accessed 18 May. 2016].

[1.13] Martinez, P. (2012). Diffusion through Oxide Barriers for Solar Cell Application. Phd Thesis. University of Konstanz.

[1.14] Saga, T. (2010). Advances in crystalline silicon solar cell technology for industrial mass production. NPG Asia Materials, 2(3), 96.

[1.15] Han, H., Huang, Z. and Lee, W. (2014). Metal-assisted chemical etching of silicon and nanotechnology applications. Nano Today, 9(3), 271.

[1.16] Dasgupta, N.P., Sun, J., Liu, C., Brittman, S., Andrews, S.C., and…Yang, P. (2014). 25th Anniversary Article: Semiconductor Nanowires-Synthesis, Characterization, and Applications. Advanced Materials, 26, 2137.

[1.17] Nalwa, H.S. (2011). Journal of Nanoscience and Nanotechnology, 11(12), 1.

[1.18] Stelzner, T., Pietsch, M., Andrä, G., Falk, F., Ose, E. and Christiansen, S. (2008). Silicon nanowire-based solar cells. Nanotechnology, 19(29), 295203.

[1.19] Zhang, X., Zeng, X., Zhang, S. and Liu, F. (2016). Improving the performance of radial n-i-p junction Si nanowire solar cells by catalyst residue removal. Materials Science in Semiconductor Processing, 41, 457.

[1.20] Zeng, L., Yu, X., Han, Y. and Yang, D. (2012). Performance of Silicon Nanowire Solar Cells with Phosphorus-Diffused Emitters. Journal of Nanomaterials, 156986(2012), 1.

[1.21] Lajvardi, M., Eshghi, H., Ghazi, M., Izadifard, M. and Goodarzi, A. (2015). Structural and optical properties of silicon nanowires synthesized by Ag-assisted chemical etching. Materials Science in Semiconductor Processing, 40, 556.

[1.22] Li, S., Ma, W., Zhou, Y., Chen, X., Xiao, Y., Ma, M., Zhu, W. and Wei, F. (2014). Fabrication of porous silicon nanowires by MACE method in $HF/H_2O_2/AgNO_3$ system at room temperature. Nanoscale Research Letters, 9(1), 196.

[1.23] Huang, Z., Geyer, N., Werner, P., de Boor, J. and Gösele, U. (2010). Metal-Assisted Chemical Etching of Silicon: A Review. Advanced Materials, 23(2), 285.

[1.24] Xiu, F., Lin, H., Fang, M., Dong, G., Yip, S. and Ho, J. (2014). Fabrication and enhanced light-trapping properties of three-dimensional silicon nanostructures for photovoltaic applications. Pure and Applied Chemistry, 86(5), 1.

[1.25] Muralidharan, V.S., and Subramania, A. (2009). Nanoscience & Technology. India: Ane Books Pvt. Ltd.

[1.26] Chartier, C., Bastide, S. and Lévy-Clément, C. (2008). Metal-assisted chemical etching of silicon in $HF–H_2O_2$. Electrochimica Acta, 53(17), 5509.

[1.27] Fang, H., Wu, Y., Zhao, J. and Zhu, J. (2006). Silver catalysis in the fabrication of silicon nanowire arrays. Nanotechnology, 17(15), 3768.

[1.28] Aslan, T. (2015). Electronic Transport Properties of Silicon Nanowires. MSc thesis. University of the Witwatersrand.

[1.29] Mohr, N., Meijer, A., Huijbregts, M. & Reijnders, L. (2009). Environmental impact of thin-film GaInP/GaAs and multicrystalline silicon solar modules produced with solar electricity. The International Journal of Life Cycle Assessment. 14(3), 225.

[1.30] Chen, G. (2008). Silicon nanowires for solar photovoltaic applications. SPIE Newsroom, 11(7), 52.

[1.31] Khan, F., Baek, S. & Kim, J. (2014). Dependence of Performance of Si Nanowire Solar Cells on Geometry of the Nanowires. The Scientific World Journal, 2014, 1.

UNIVERSITY of the
WESTERN CAPE
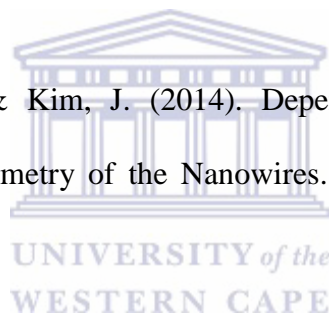
Chapter Two: Phosphorus Diffusion

2.1 Introduction

Introducing carriers into the conduction band (CB) or removing carriers from the valence band (VB) of semiconductors allows semiconductors to become more conductive; this process is known as doping. In the simplest case, a p-n junction is formed by doping p-type semiconductors with n-type dopants [1.1], as outlined in Chapter One, Section 1.2.2. In order to form a p-n junction, thermal diffusion using gaseous or liquid sources is an alternative doping method to ion implantation [2.1, 2.2]. Thermal diffusion of P in Si is currently the principal method for emitter formation in Si solar cell (SC) processing [2.1, 2.3]. Here, we adopt the drive-in diffusion annealing technique of bulk p-type Si, to produce n-doped MaCE-grown Si NWs by using a liquid Phosphorus oxychloride (POCl$_3$) n-type P-containing spin-on dopant (SOD) as the diffusant source by means of a post-deposition technique that separates the doping step (i.e. spin coating) from the Si NW growth process (i.e. MaCE). Most studies on the diffusion doping of Si NWs are carried out with VLS-grown Si NWs [2.4]. Hence, there is a limitation in our understanding of the exact diffusion process of applying the SOD to the MaCE-grown Si NWs. As a result, it cannot be confirmed whether the P-doped n-type Si NWs follows the same diffusion process that will be outlined in Section 2.3.

2.2 Spin-on Doping and Atomic Diffusion

2.2.1 Spin-on Doping

More than fifty years ago Emil et al. (1958) performed the original spin-on doping study by analysing the spreading of a Newtonian fluid characteristic of a thin axisymmetric film on a planar substrate that rotates with constant angular velocity. Centrifugal force causes the liquid to flow radially outward. The result of the viscous force and surface tension is the reason why the thin residual film can collect on the top flat surface of the substrate. The film becomes thin due to the product of outward fluid flow and evaporation [2.5].

The key stages of the spin-on doping method can include:

1. The fluid dispense

2. Spin-up

3. Stable fluid outflow

4. Evaporation

In this study, we refer to the thin film as the dopant layer; it is primarily formed by two independent parameters, namely the viscosity and spin speed. In general, the film thickness is about 1 to 200 μm. The key stages of the spin-on doping method are presented in Figure 2.1 and explained in detail as follows:

1. The fluid dispense

During the first stage, the SOD source may be exposed to the top surface of the spinning substrate from a microsyringe; the substrate accelerates at a specified rotation speed. The SOD spreads because of centrifugal forces and the initial thickness is reduced to an

33

acute thickness. In this study, the SOD was drop cast at the centre of a Si NW sample prior to spinning.

2. Spin-up

The second stage is usually characterised by forceful SOD removal from the substrate surface by the rotational motion. The substrate accelerates at a specified final rotation speed. Spiral vortices may be briefly present during this stage due to the initial depth of the SOD on the substrate surface because of the twisting motion caused by inertia that the top of the SOD exerts, whilst the substrate below subsequently moves faster. Ultimately, the SOD will be thin enough to be co-rotated with the substrate and a uniform source thickness is achieved. Once the substrate reaches its specified speed, the SOD will be thin enough so that the viscous shear drag balances the rotational acceleration.

3. Stable fluid outflow

The third stage is characterised by steady SOD thinning. The substrate is spinning at a constant rate and the SOD viscous forces overtake the SOD thinning behaviour.

4. Evaporation

The fourth stage is the dopant layer drying stage where the centrifugal outward flow stops, and the shrinkage of the layer occurs due to solvent loss. At this stage, the dopant layer forms on the substrate while the substrate is rotated at a constant speed and the solvent evaporation overtakes the coating thinning behaviour. The result is the formation of a P-rich oxide dopant layer on the Si NW substrate.
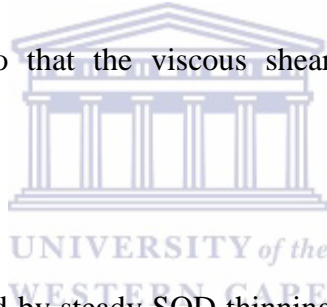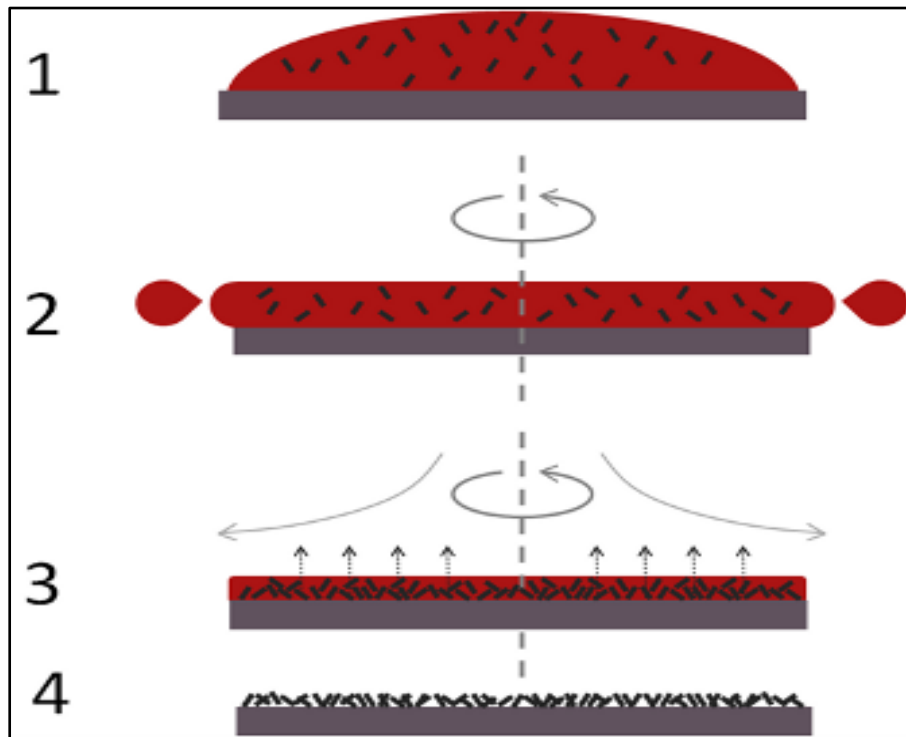
Figure 2.1: The key stages of the spin-on doping method [2.6].

Thin film (dopant source) deposition technology is classified into chemical and physical. Spin-on doping is a physical means of deposition that involves a physical reaction. This can be explained, such that the dopant source is physically deposited onto the Si NW wafer. In other words, the dopant layer is not formed by a chemical reaction. This is not entirely correct for spin-on doping but is more convenient to classify it as physical [2.7].

2.2.2 Atomic Diffusion

Diffusion in a semiconductor may be regarded as the re-arrangement of the dopant atoms through the crystal lattice because of random thermal movement. Impurity dopant atoms can occupy either interstitial or substitutional positions in the Si lattice (Figure 2.2). Dopant atoms such as arsenic (As), boron (B), and phosphorus (P) occupy

35

substitutional positions, in which the dopant atoms donate free electrons or holes to the Si lattice [2.8].
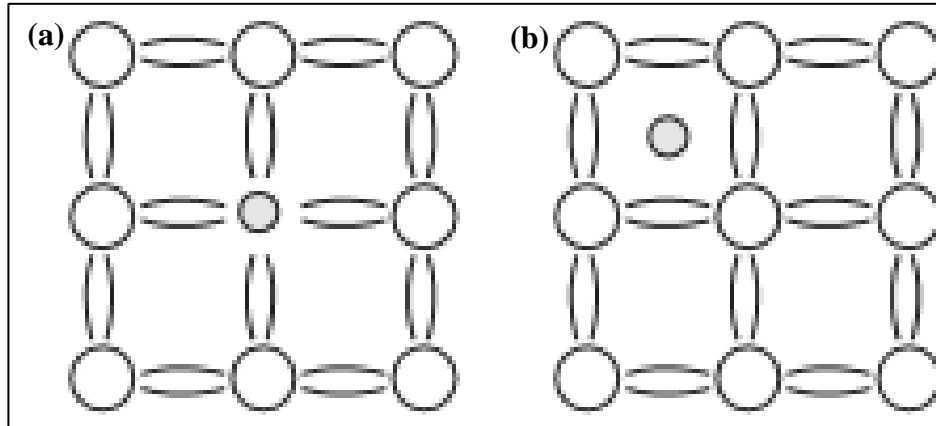

Figure 2.2: (a) Substitutional and (b) interstitial dopants in Si [2.8].

During high-temperature processing, the host atoms vibrate around equilibrium lattice sites. The vacancy diffusion mechanism involves the finite probability of a host atom acquiring sufficient energy to leave its lattice site to become an interstitial atom, thereby creating a vacancy and ultimately leading to a neighbouring dopant atom moving to a vacancy site as illustrated in Figure 2.3 (a). When a dopant atom moves from one position to the next without occupying a lattice site (see Figure 2.3 (b)), the mechanism is known as interstitial diffusion [2.8].

Another concept that arises is interstitialcy diffusion (see Figure 2.3 (c)). This occurs when Si self-interstitials relocate substitutional dopants to an interstitial position, hence requiring the presence of Si self-interstitials. The dopant interstitial can then displace a Si lattice atom into a self-interstitial position. Dopant atoms such as As, P, and B occupy substitutional positions once initiated, the dopant diffusion is controlled by the presence of vacancy and interstitial point defects [2.8].
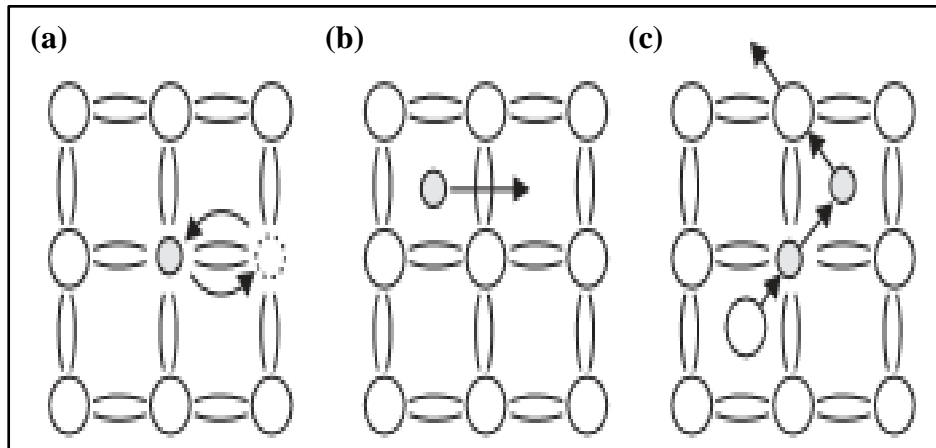
36

Figure 2.3: (a) Vacancy, (b) interstitial and (c) interstitialcy diffusion mechanism [2.8].

2.3 Phosphorus Diffusion

A liquid $POCl_3$ source (a P-containing source) along with nitrogen (N_2) and oxygen (O_2) as transport gasses is a well-known method employed in the PV industry to form an n-type emitter in a p-type Si wafer. P diffusion may be described as follows [1.13]:

The wafers are loaded in a boat into a closed tube furnace. The boat and the tube are normally made of quartz. The heating procedure commences once the wafers are inside the tube furnace. The diffusion process may be separated into two stages, namely the pre-deposition stage and the drive-in stage, which can proceed at the same or at different temperatures.

During the pre-deposition stage:

A N_2 carrier gas is used to bring the liquid $POCl_3$ into the tube furnace where O_2 is being supplied as well. The $POCl_3$ liquid becomes a gas inside the heated furnace and reacts with O_2 to form phosphorus pentoxide (P_2O_5) and chlorine (Cl_2), according to Equation 2.1:

37

$$4POCl_3 \text{ (g)} + 3O_2 \text{ (g)} \rightarrow 2P_2O_5 \text{ (ℓ)} + 6Cl_2 \text{ (g)} \tag{2.1}$$
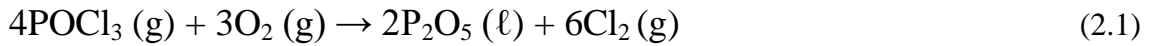
During the drive-in stage:

For the drive-in stage, the supply of $POCl_3$ is stopped. The P_2O_5 formed during the pre-deposition stage reacts with Si to form SiO_2 on the Si surface and P atoms are released and diffused into Si according to Equation (2.2). Due to the low boiling temperature (105.8 $^{\circ}$C), $POCl_3$ is decomposed into P compounds, such as P_2O_5 at temperatures between 750 $^{\circ}$C and 900 $^{\circ}$C. The drive-in stage is described by Equation (2.2):

$$2P_2O_5 \text{ (ℓ)} + 5Si \text{ (s)} \rightarrow 5SiO_2 \text{ (s)} + 4 P \text{ (s)} \tag{2.2}$$
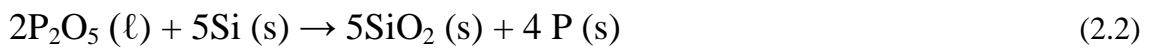
Si is oxidised, creating a liquid/solid thin layer of SiO_2 at the surface of Si. Furthermore, P_2O_5 reacts with SiO_2 to form a phosphorus silicate glass (PSG) layer on SiO_2 according to equation (2.3):

$$x SiO_2 + y P_2O_5 \rightarrow \ x SiO_2 \cdot y P_2O_5 \tag{2.3}$$

Figure 2.4 presents a proposed model showing the various areas formed during P diffusion. A SiO_2 (s) thin layer is formed on the surface of Si as described by Equation (2.2) (area IV). A layer of SiO_2 (s) + PSG (s) (area III) is formed on top of the SiO_2 layer. Thereafter, two distinct areas (II and I) exist as a liquid + solid (SiO_2 (s) + PSG (ℓ)) and a liquid phase (PSG (ℓ)), respectively. As can be seen in Figure 2.4, the PSG thickness can be considered to be $X_{PSG} = x_1 + x_2 + x_3$.
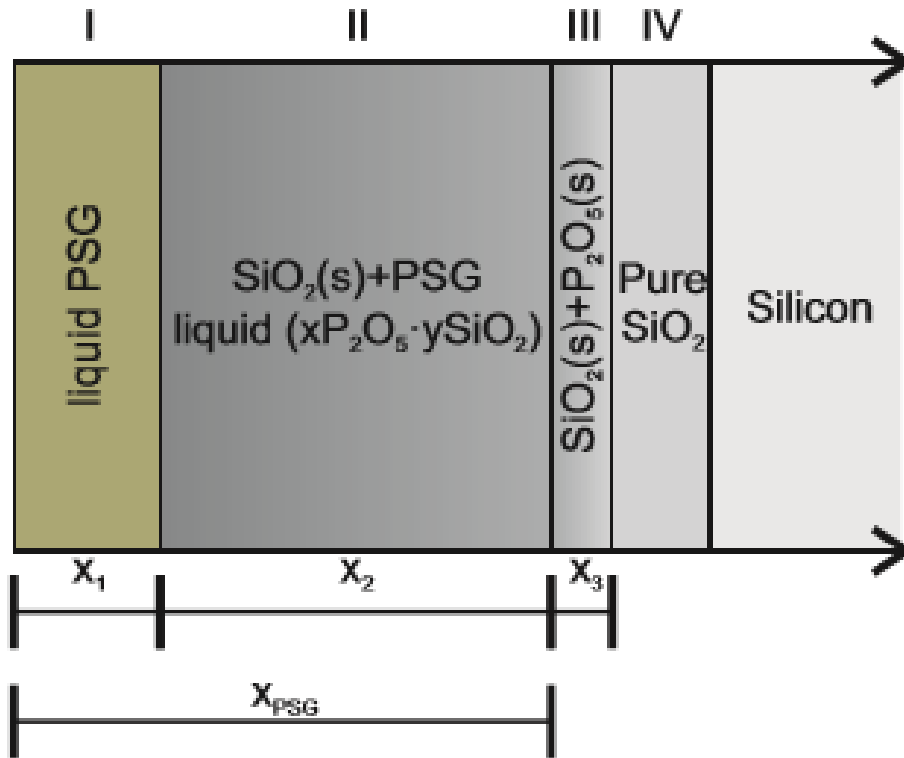
Figure 2.4: Schematic of the proposed model of PSG on Si [1.13].

2.4 Proposed Mechanism of the Post-doping of Silicon Nanowires

In this study, we assume that at the end of the spin-on doping procedure, a P-rich oxide layer of $x(P_yO_z)$ form is created. Figure 2.5 presents a schematic of the proposed $x(P_yO_z)$ layer created on the Si NW surface after spin-on doping. The stoichiometry of the $x(P_yO_z)$ layer can be determined from a characterisation technique such as X-ray photoemission spectroscopy as will be discussed in the results section. During the drive-in stage, $x(P_yO_z)$ reacts with Si forming SiO_2 on the Si NW surface and simultaneously releases P atoms to diffuse into the Si NWs [1.13]. This means that the Si NWs is oxidised forming a SiO_2/Si NW interface. At the same time, $x(P_yO_z)$ react with SiO_2 to form a PSG layer on-top of SiO_2 in accordance with Equation 2.4:

$$w\text{SiO}_2 + x\text{P}_y\text{O}_z \rightarrow w\text{SiO}_2 \cdot x\text{P}_2\text{O}_5 \tag{2.4}$$

Here onwards, we assume the same principles as outlined in Section 2.3 excluding the layers marked as I and II. Figure 2.6 presents the proposed layers formed after the drive-in stage. SiO_2 is continuously created at the SiO_2/Si NW interface during the reaction of $x(\text{P}_y\text{O}_z)$ with the Si NWs. As a result, the P atoms from $x(\text{P}_y\text{O}_z)$ need to move through the PSG, SiO_2 or the combination of both to reach the Si NW wafer. The P atoms that are able to reach the Si NW wafer will form the P-doped n-type Si NWs. The P atoms are rejected from the SiO_2 layer, and diffuse slowly in SiO_2, forming accumulations at the Si NW surface. The pile-up of P in the Si NWs thus depends on the diffusivity (D) and the segregation coefficient (k) of P in SiO_2. It was found that the $x(\text{P}_y\text{O}_z)$ concentration will reduce, as it reacts with the underlying SiO_2 layer.
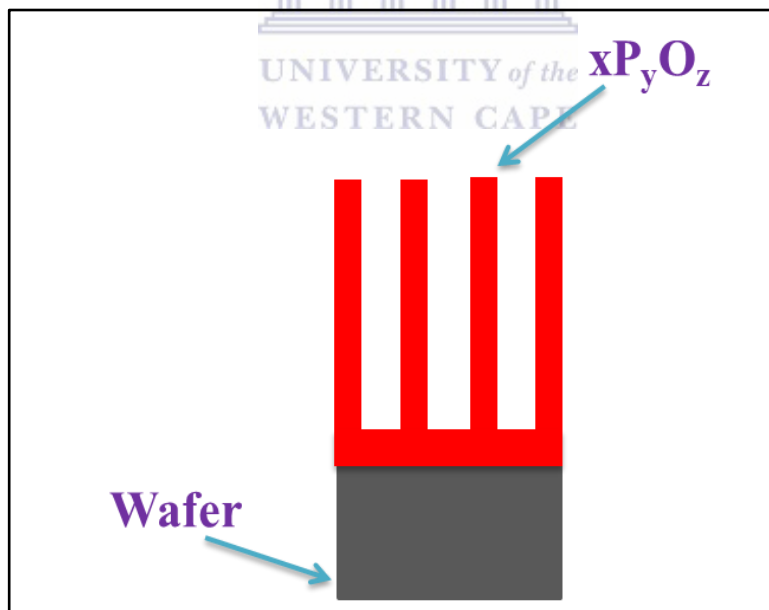

Figure 2.5: Schematic of the proposed $x(\text{P}_y\text{O}_z)$ layer created on the Si NW surface after spin-on doping.
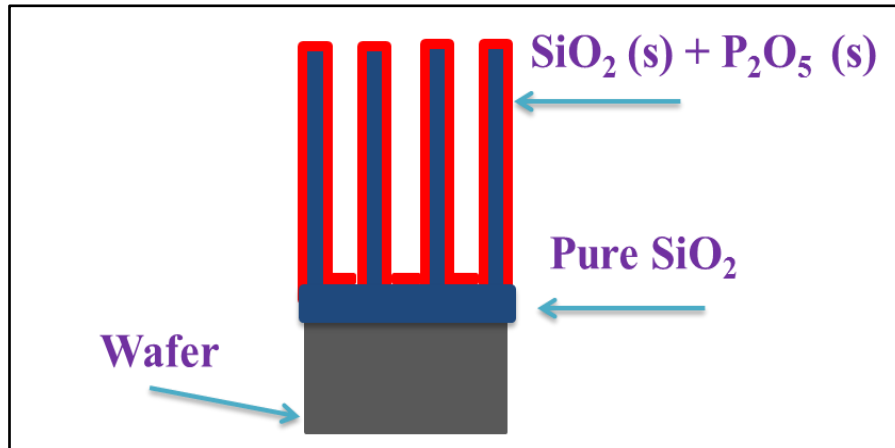
Figure 2.6: Proposed layers formed after the drive-in stage.

2.5 Diffusivity of Phosphorus in Silicon

Two mechanisms describe how impurity dopant atoms reoccur at the lattice, namely, the kick-out mechanism and the (dissociative) Frank-Turnbull mechanism. For the kick-out mechanism, a dopant atom exchanges positions with a lattice atom and for the dissociative mechanism an interstitial impurity atom is apprehended by a vacancy. These two mechanisms do not need the presence of self-interstitials. It is assumed that the diffusivity of P in Si is ruled by the vacancy mechanism. Figure 2.7 presents the vacancy model, depicting three regions where the diffusivity differs, depending on the concentration of the dopant atoms. In Figure 2.7 we see a high concentration region where the diffusivity of the dopant impurity is $D \propto n^2$ (n is the electron concentration) and in the tail region $D \propto n_e^3$ (n_e is the electron concentration at the plateau region). The vacancy diffusion requires a higher energy than interstitial diffusion since the substitutional atoms are more tightly bound than the interstitial atoms. The energy needed to jump from one position to the next is formally known as the activation energy (E_a), but for vacancy diffusion, it is the energy needed to form a silicon vacancy [1.13].

The following sets of equations describe the diffusivity of P in Si in the three regions in accordance with Figure 2.7 [1.13].

The intrinsic diffusivity of phosphorus is given as:

$$D_i = 3.85 \cdot \exp\,(-\,3.66/\,k_B T)\ [cm^2/\,s] \tag{2.5}$$

In the high concentration region, the total amount of P concentration exceeds the active amount of P concentration. The P^+ ions joins with $V^=$ vacancies (double negative charge vacancy) to generate $P^+V^=$ pairs as $(PV)^-$ and ***the extrinsic diffusivity of phosphorus is given as:***

$$D_x = D^0 + D^=\,(n/\,n_i)\ [cm^2/\,s] \tag{2.6}$$

Where $D^+ = 0$, $D^0 = D_i$ and $D^=$ is given as:

$$D^= = 44.2 \cdot \exp\,(-\,4.37/\,k_B T)\ [cm^2/\,s] \tag{2.7}$$

The electron concentration for the kink region is given as:

$$N_e = 4.65 \times 10^{17} \cdot \exp\,(-\,0.39/\,k_B T)\ [1/cm^3] \tag{2.8}$$

The diffusivity of phosphorus in the tail region is given as:

$$D_{Tail} = D^0 + D^-\,n_e^{\,3}/\,N_e^{\,2} n_i\,[1 + \exp\,(0.3/\,k_B T]\ \ [cm^2/\,s] \tag{2.9}$$

Where

$$D^- = 4.44 \cdot \exp\,(-\,4/\,k_B T)\ [cm^2/\,s] \tag{2.10}$$

Phosphorus diffusion is strongly linked to and controlled by the interstitial mechanism. The oxidation of Si plays a major role in the diffusion of P, whereby the self-interstitials

are included in the diffusion of elements in Group III and Group IV, and the conversion of P interstitialcy to substitutional form is due to self-interstitial emission.
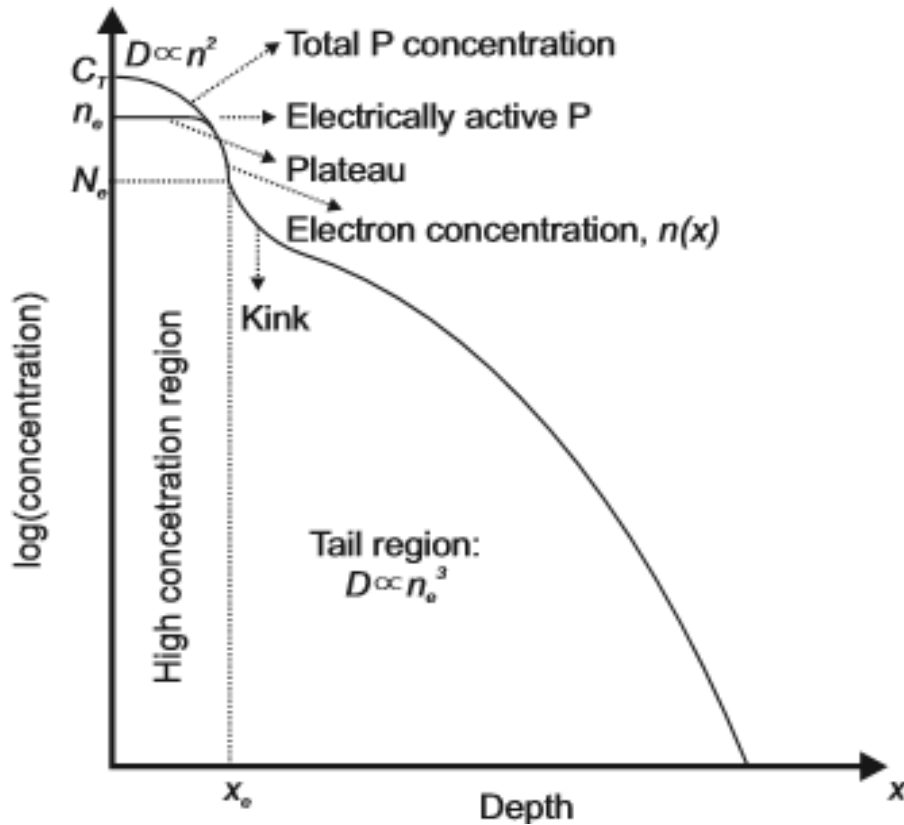
Figure 2.7: Phosphorus diffusion profile [1.13].

2.6 Solid Solubility of Phosphorus in Silicon

There exists a limit to a maximum amount of P concentration that can exist in the Si wafer in equilibrium at a given temperature. If this limit is exceeded, monoclinic or orthorhombic SiP precipitate forms in the highly doped region. The SiP precipitate may be expressed as [1.13]:

$$\text{SiP} + \text{P} \rightarrow \text{SiP} \qquad\qquad (2.11)$$

43

The P-precipitate is known to be inactive P atoms that occupy substitutional positions in the Si lattice and that do not contribute to current transport. Electrically inactive P dopants occupy positions near the surface area, called the "dead layer". From Figure 2.7, the dead layer is situated at the depth "x_d" for which $n(x_d) = n_e$, where n_e is the active dopant concentration at the plateau level. Electron diffraction studies showed that the precipitate in the diffused Si is SiP and assumes that P precipitates at the Si/SiO$_2$ interface. The inactive P thus exists in a precipitated phase and not as point defects, since they do not influence the electron mobility even at high concentrations. Figure 2.8 presents the plot of the active P concentration (n_e), inactive mobile P concentration ($C_{sat} - n_e$) and saturation concentration C_{sat} [1.13].
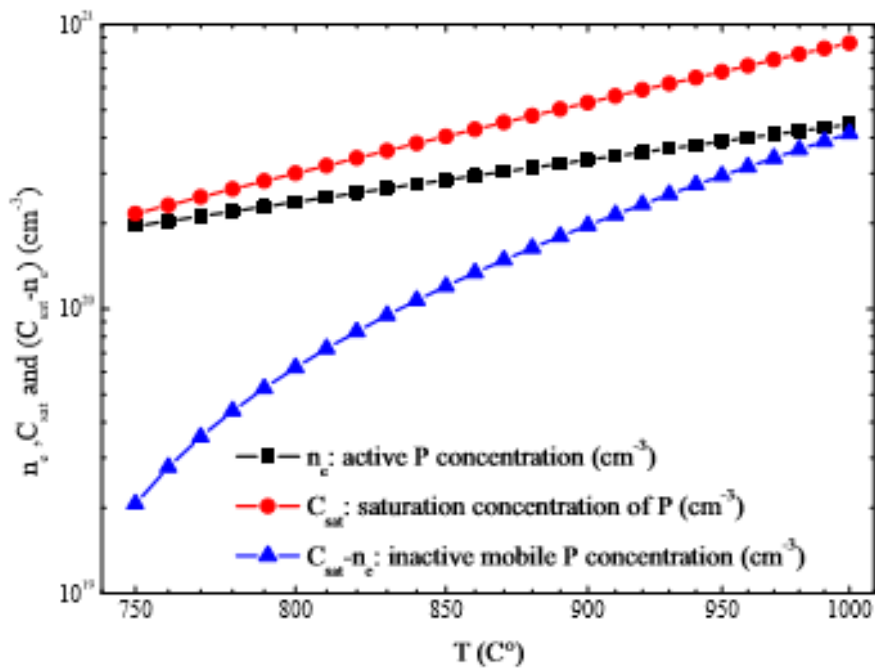

Figure 2.7: Active P, saturation and inactive mobile P concentration [1.13].

The plots were acquired by applying the following equations:

$$n_e(T) = 1.3 \times 10^{22} \cdot \exp(-0.37/k_B T) [1/cm^3] \qquad (2.12)$$

$$C_{sat}\,(T) = 2.45 \times 10^{23} \cdot \exp\,(\text{-}0.62/\,k_B T)\;[1/cm^3] \qquad\qquad (2.13)$$

P diffuses in the Si lattice by interacting with vacancies in three distinct charge states: $P^+\,V^x$, $P^+\,V^=$, where V^x is a neutral vacancy, $V^=$ is a double negative charge vacancy and V^- is a single negative charge vacancy. The $P^+\,V^=$ plays a major role when the total concentration exceeds N_e (see Figure 2.7). As a result, the $P^+\,V^=$ plays a major role when the total concentration exceeds N_e (See Figure 2.7). As a result, the $P^+\,V^=$ pair will extract an electron from the CB and ultimately fill the second acceptor level of the vacancy, thus forming an electrically inactive P atom. When the concentration is close to N_e, the $V^=$ vacancy has an increased probability of losing an electron by becoming V^-. Hence, this lowers the binding energy (BE) of the $P^+\,V^-$ pair and causes a higher probability of the pair dissociation, forming a surplus of V^- above equilibrium values. The end result is responsible for increased diffusion in the tail region [1.13].

A reliable diffusion mechanism has been proposed for P diffusion, such that the vacancy mechanism exists for the slower diffusion component and the interstitialcy mechanism for the faster diffusion component. Hence, it involves an interchange from the vacancy diffusion mechanism through the double negative charge vacancy at high concentrations to an interstitially governed diffusion at lower concentrations. At the high concentration region, P precipitates enter supersaturation. The supersaturation of P is due to the PSG formation and P exceeding its solid solubility limit. As a result, the precipitates are of SiP composition and orthorhombic structure [1.13].

2.7 References

[2.1]   Xu, Y. (2015). Fabrication and characterization of photodiodes for silicon nanowire applications and backside illumination. MSc thesis. The School of Engineering of the University of Dayton.

[2.2]   2016. Available: http://Experiment 3 (Doping using Drive-in-Diffusion) [2016, August 7].

[2.3]   Basher, M.K., and Shorowordi, K.M. (2015). Fabrication of Monocrystalline Silicon Solar Cell using Phosphorus Diffusion Technique. International Journal of Scientific and Research Publication, 5(3), 1.

[2.4]   Mertens, R. (2012). Characterization, morphology, oxidation and recession of silicon nanowires grown by electroless process. PhD Thesis. University of Central Florida.

[2.5]   Sahu, N., Parija, B. & Panigrahi, S. (2009). Fundamental understanding and modeling of spin coating process: A review. Indian Journal of Physics. 83(4), 493.

[2.6]   2016. Available: http://Ossila. (2016). Spin Coating: A Guide to Theory and Techniques. Retrieved from Ossila – enabling innovative electronics [2016, September 29].

[2.7] 2016.Available:http://personal.strath.ac.uk/barry.williams/Book/Chapter%201.pdf [2016, September 29].

[2.8]   2016. Available: http://Jones, S.W. IC Knowledge LLC. [2016, September 29].

Chapter Three: Experimental Techniques

3.1 Introduction

This chapter provides comprehensive descriptions of the progression of the experimental techniques used to ultimately form the n-doped Si NWs. Section 3.2 introduces the fabrication route used to synthesize the Si NWs by means of the metal-assisted chemical etching (MaCE) fabrication technique. Thereafter, Section 3.3 gives an overview of the equipment used and the experimental conditions during post-deposition doping of the Si NWs. This includes the operating conditions of the spin coater used in this work and the spin-on doping process, as well as the experimental route taken during phosphorus (P) dopant drive-in diffusion annealing and the operating conditions of the thermal chemical vapour deposition (TCVD) three-zone tube furnace that is equipped with a mass flow control (MFC) system. Section 3.4 focuses on the fundamental physics underlying the analytical techniques, as well as the sample preparation, and data acquisition within the respective techniques that were used to characterize the MaCE-grown Si NWs and n-doped Si NWs.

3.2 Synthesis of Si NWs by Metal-assisted Chemical Etching

The MaCE fabrication technique used to form Si NWs was specifically performed at room temperature (25 °C). At first, $\sim 1 \times 1$ cm^2 p-type polished single-crystalline (100) Si wafers (size (100 mm), resistivity (1-10 Ω.cm), thickness (380 μm), purchased from Saetra (Pty) Ltd., Pretoria, South Africa), were carved with a diamond cutter on a non-slipping cutting mat. Precautionary measures were taken in view of the hazardous nature of the solution and ingredients used, and the potential damage caused during the preparation of the solution and the wafers. These precautionary measures include the following: The Si wafers were stored in plastic sample holders to avoid any possible external damages. All solutions were prepared prior to the etching of the Si wafers to ensure a smooth-running process. In addition, protective gear was worn and the experiment was conducted under a fume hood, as it involved exposure to a highly corrosive liquid, such as hydrofluoric acid (HF, analysed reagent, 48% purity, purchased from Sigma-Aldrich, Missouri, USA). The $\sim 1 \times 1$ cm^2 carved Si wafers were handled with polytetrafluoroethylene (PTFE) Teflon beakers and Teflon coated stainless steel tweezers to avoid any possible contamination in the laboratory.

Thereafter, the wafers were ultrasonically cleaned with acetone (C_3H_6O), followed by ethanol (C_2H_6O) cleaning, both for 5 minutes in an ultrasonic cleaner to remove surface grease. The wafers were then rinsed a few times with de-ionized (DI) water. Subsequently, the cleaned wafers were cured with 5% HF for 60 seconds to remove the native surface oxide layer. To obtain 5% HF, 5 millilitres (mL) of the 48% HF was

48

diluted with 50 mL DI water, giving a total of ∼ 4.8% solution, which can be approximated to 5% HF.

The Si wafers were immediately immersed into a metallization aqueous solution of 5 molar concentrations (M) HF and 0.02 M silver nitrate ($AgNO_3$, ≥ 99.0%, ACS reagent, purchased from Sigma-Aldrich, Missouri, USA) for 60 seconds to deposit Ag nanocatalyst particles. Take note that, after every successive step from here onwards, the wafers were rinsed a few times with DI water and left to dry. The HF/$AgNO_3$ solution was diluted with DI water until it ultimately reached a volume of 100 mL. More specifically, 9.0625 mL of 5 M HF was slowly added to 40.938 mL of DI water to achieve 50 mL of HF solution, and ∼ 169.9 milligrams (mg) of 0.02 M $AgNO_3$ salt, which was measured on a sensitive mass scale, was added to 50 mL of DI water. Ultimately, the resultant HF/H_2O and $AgNO_3$/H_2O were added to each other to achieve a 100 mL $AgNO_3$/HF/H_2O solution for the Ag NP deposition. A volume of 100 mL was used for convenience.

Immediately after the Ag NP deposition, the wafers were individually rinsed a few times with DI water to remove the Ag ion residues formed on the Si wafer surface and left to dry. The Ag-catalysed Si wafers were then immersed into an etchant solution of HF/H_2O_2/H_2O for 20 minutes. The HF solution was prepared in the same manner as mentioned in this Section and 2.55 mL of 0.2 M hydrogen peroxide (H_2O_2, 30% purity, analysed reagent, purchased from Merck Chemicals (Pty) Ltd., Gauteng, South Africa) was diluted with 47.5 mL H_2O to achieve 50 mL of H_2O_2 solution. Ultimately, the resultant HF/H_2O and H_2O_2/H_2O solutions were added to achieve 100 mL of the etchant solution (HF/H_2O_2/H_2O) to form the resultant MaCE-grown Si NWs. Finally, the Ag NPs formed at each Si NW/wafer interface were removed by means of concentrated

49

nitric acid (HNO$_3$, 65% purity, ACS reagent, purchased from Sigma-Aldrich, Missouri, USA). Figure 3.1 presents a schematic representation of the MaCE fabrication technique to form the resultant MaCE-grown Si NWs. The Ag NPs formed at the Si NW/wafer interface is not shown in the Figure. Thereafter, the MaCE-grown Si NWs were ready for the spin-on doping process using a KW-4A Spin Coater.
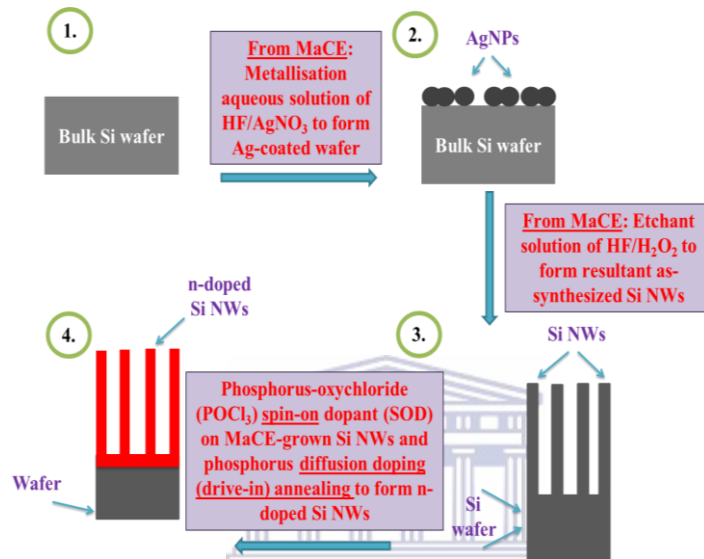

Figure 3.1: Schematic of the MaCE fabrication technique.

3.3 Post-deposition Doping Experimental Procedure

3.3.1 Spin-on Doping Experimental Procedure

3.3.1.1 KW-4A Spin Coater

The KW-4A Chemat Technology Spin Coater is compact and easy to use, in order to ensure the uniform deposition of coatings and thin films. Its versatility allows various studies to be conducted since its design is portable, rugged, and vibration-free. Figure 3.2 presents a pictorial representation of the control panel of the KW-4A Spin Coater [3.1]. The functions of the power and start switches are to turn the power of the spin coater on/off and to start the spinning cycle process, respectively. Note that the spinning cycle process will only function once the control and vacuum switches are pressed. The

50

control switch needs to be on before the spinning process can be carried out and switched off once the process is terminated. The vacuum switch allows the operator to control the vacuum to the vacuum chuck. If the vacuum switch is not on, then the motor cannot operate [3.2].

Figure 3.2: Control panel of the KW-4A Spin Coater [3.1].

3.3.1.2 Spin-on Doping Experimental Procedure

Safety precautions had to be adhered to when working with liquid phosphorus oxychloride (POCl$_3$, ≥ 99.0%, purchased from Merck Millipore, Massachusetts, USA), a P-containing spin-on dopant (SOD) as the dopant diffusant source, since elevated levels of POCl$_3$ are hazardous. Hence, the KW-4A Spin Coater used for the spin-on doping process was placed at a working distance in a built-in fume hood, from which air was drawn from the open side of the fume hood and fed back into the laboratory room. An Edwards RV3 vacuum pump was also employed to control the vacuum to the vacuum chuck in order to hold the rotating wafer firmly in place. The power and control switches must be pressed before initiating the spinning cycle process. The spin cycle

51

times for the fluid dispense and spin-up stages were 9 and 20 seconds, respectively, whereas the spin cycle speeds for the fluid dispensing and the spin-up stages were 500 rotations per minute (rpm) and 2000 rpm, respectively. Both the spin cycle times and the speeds were pre-set accordingly. These stages refer to the first two stages of the key stages of the spin-on doping process, as outlined in Chapter Two, Section 2.2, in which the spinning speeds up during the second stage. The timer and spin controls are shown in Figure 3.2.

The Si NW wafers were individually centred on the sample chuck, and the vacuum button was pressed to turn on the vacuum. Once the Si NW wafer was firmly in position, approximately 3 drops of liquid $POCl_3$ were applied to the top surface of the wafer with a plastic transfer pipette, ensuring that the entire surface area of the wafer was covered with the dopant source. The bowl cover was placed over the bowl, and the spinning cycle process was initiated by pressing the start switch at the previously mentioned pre-set spin cycle times and speeds. At the end of the spinning process, the control switch was pressed. Figure 3.3 shows the experimental set-up during spin-on doping. The inset of Figure 3.3 illustrates the sample chuck onto which the sample was placed. Thereafter, the Si NW wafers that were exposed to spin-on doping creating a P-rich oxide layer on Si NW wafers were ready for annealing.
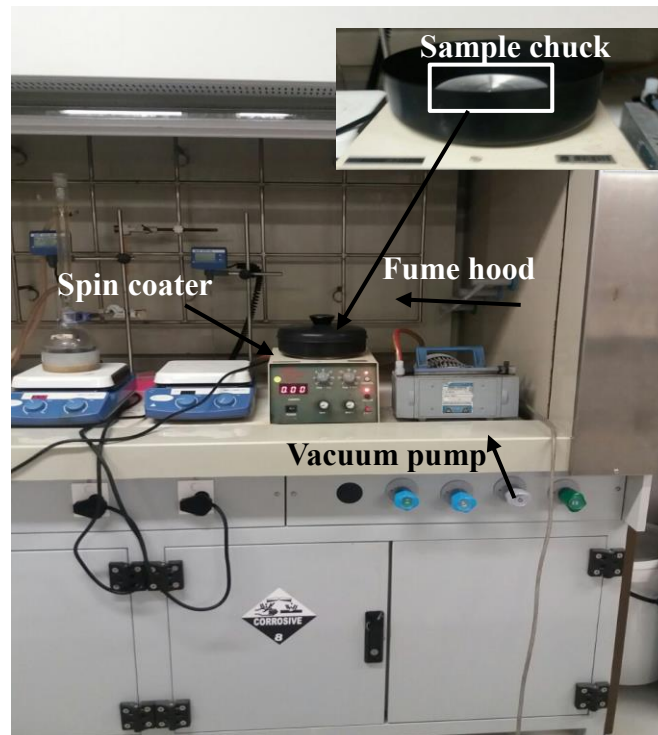
52

Figure 3.3: Spin-on doping experimental set-up and corresponding illustration of the sample chuck.
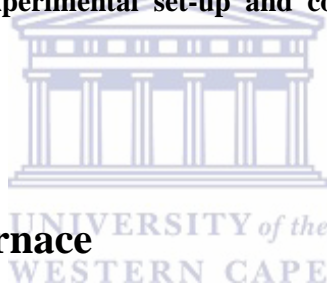
3.3.2 Annealing in Furnace

3.3.2.1 Thermal Chemical Vapour Deposition Three-Zone Furnace System

The thermal chemical vapour deposition (TCVD) system, a Brother (XD-1600MT) three-zone tube furnace, proposed and synthesized by Zhengzhou Brother Furnace Co., Ltd, was utilized for the P dopant drive-in diffusion annealing to obtain the resultant n-doped Si NWs. Figures 3.4 (a) and (b) illustrate the overall system and the control system of the Brother (XD-1600MT) tube furnace, respectively.

Figure 3.4: (a) The overall system and (b) the control system of the Brother (XD-1600MT) three-zone tube furnace.
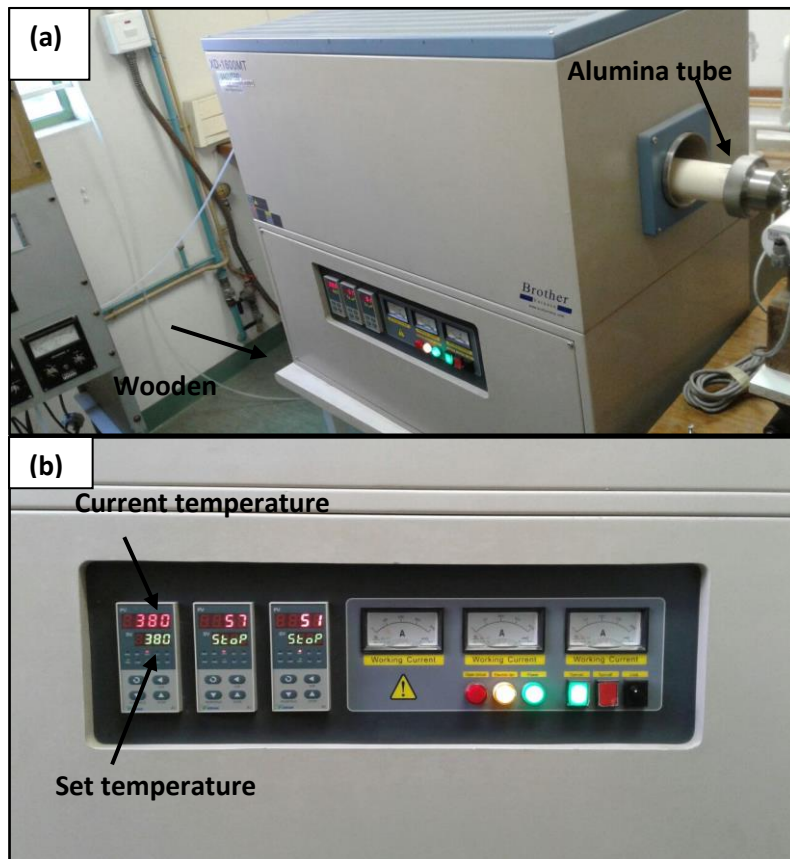
The furnace is ideal for various materials since the accuracy of the temperature controller is around ± 1 °C. This high precision bench-top tube furnace employs high-quality ceramic molybdenum disilicide ($MoSi_2$) rods and resistance wires as heating elements. The furnace is mass-produced from a double layer steel casing with a three-fan cooling system that enables the furnace surface to remain at a lower temperature than the inner chamber. Each square-shaped heating chamber in the furnace is $20 \times 20 \times 20$ cm in dimension, with a 4 cm thick insulating material subdividing the heat chambers from each other. For each chamber, the current temperature (PV) and the set temperature (SV) are displayed on the temperature control system. For convenience and flexibility, the system was mounted on top of a $100 \times 60 \times 60$ cm wooden top trolley [3.3].

54

3.3.2.2 Mass Flow Control System

Nearly all applications in CVD require mass flow metering and control in the experimental and production setup. Gas flow is needed as a carrier gas, as the reaction gas, and also for purging or throttling in a vacuum pump [3.4]. In this study, the TCVD system is coupled with a mass flow control system (MFC) system to control the mass flow rate of the N_2 carrier gas entering the TCVD system. Figure 3.5 presents a pictorial and schematic representation of the MFC system.
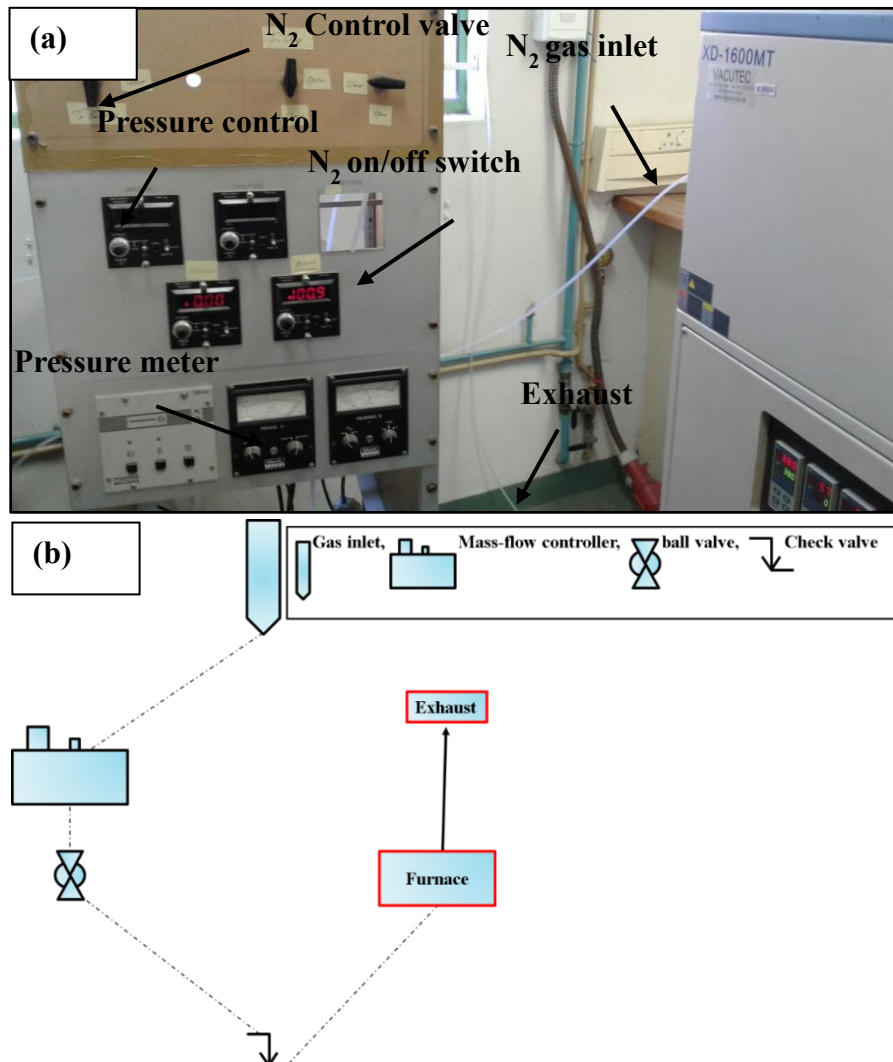

Figure 3.5: (a) The pictorial and (b) schematic representation of the mass flow control (MFC) system.

In this study, a MFC system that employs a 1179A Mass-Flow® controller was designed and constructed in the Department of Physics and Astronomy at the University of the Western Cape (UWC)). The system can employ four different gases, such as the nitrogen (N_2) carrier gas, argon (Ar) shielding gas, and the reactive gases, such as hydrogen (H_2) and silane tetrachloride ($SiCl_4$). In this study, the N_2 carrier gas was employed to prevent any unwanted chemical reactions degrading the sample.

The system consists of a gas supply and a mass flow controller (including an advanced flow sensor, a control valve, and an optimised bypass) that accurately sets, measures, and controls the mass flow rates of gases [3.5]. The flow rate was set and monitored to ~ 200 standard cubic centimetres per minute (sccm) on the control panel. Although the system is a three-way system, Figure 3.5 only illustrates the main features used in this study. The system also employs a ball-valve for turning the gas on/off and a check-valve that allows the gas to flow in one direction at a time. The mass flow controller, ball-valve and check-valve are not shown in Figure 3.5 (a), as they are situated behind the system.

3.3.2.3 Phosphorus Dopant Drive-in Diffusion Annealing Experimental Procedure

After the Si NWs were subjected to spin-on doping, thus creating a P-rich oxide layer on the surface of the Si NW wafers, the wafers were exposed to a tubular furnace annealing at various high temperatures of 700, 800, 900 and 1000 °C, separately in an N_2 purged Brother (XD-1600MT) three-zone tube furnace to form the resultant n-doped Si NWs; the furnace itself was located in a laboratory in the Department of Physics and Astronomy based at UWC. Prior to initiating the experimental procedure, segmented

temperature profiles were drawn for each annealing temperature used in this study. Figures 3.6 (a), (b), (c) and (d) depict the segmented temperature profiles of the annealing temperatures of 700, 800, 900, and 1000 °C, respectively.

About six samples were aligned to fit onto a layered Si rectangular sample stage and loaded into the alumina tube furnace. The samples were then transported 46 cm into the tube furnace with a calibrated meter stick. Another research group conducted a mini-investigation on the temperature distribution array along the heating chamber inside the tube furnace to identify ideal positions for placing the samples (see Reference 3.3 for an in-depth discussion of the temperature distribution inside the tube furnace). Two heated zones were employed and set at the same temperature, as it was found that the temperature remains constant over a reasonable distance, as shown by the research group.
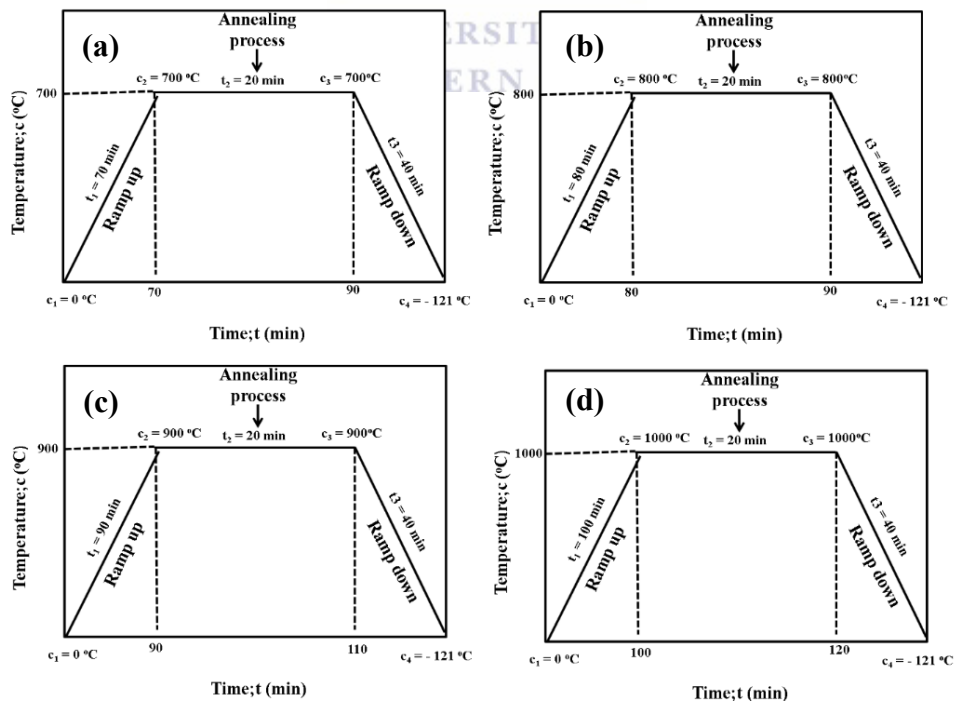

Figure 3.6: Segmented temperature profiles for annealing temperatures at (a) 700; (b) 800; (c) 900 and (d) 1000 °C.

57

After the substrates had been loaded into the furnace, both ends of the alumina tube were sealed with a pair of vacuum sealing assemblies to avoid heat radiation. Thereafter, the MFC system was switched on prior to switching on the furnace, thus enabling it to warm up. The gas supply was opened and the mass flow rate was set and controlled at ~ 200 sccm, as mentioned earlier. The main electrical supply of the furnace was then switched on at the wall socket. A green power light from the furnace control panel illuminated, indicating that the input power was supplied.

The annealing temperatures and times were set in accordance with the temperature profiles seen in Figure 3.6. The heating rate of the system is 10 °C/minute and the annealing process commenced at the current furnace temperature (PV) (i.e. room temperature). As can be seen from Figure 3.6, the furnace was ramped up to its desired annealing temperature, and then stabilised for 20 minutes. Thereafter, the system automatically cooled down to -121 °C for 40 minutes. The MFC system and furnace were switched off in the order that it was switched on. Finally, the samples were removed and dipped into HF for 60 seconds to remove the parasitic layer, as seen in the schematic of Figure 2.6 in Chapter Two.

3.4 Analytical Techniques

3.4.1 Scanning Electron Microscopy

3.4.1.1 Introduction

The scanning electron microscope (SEM) is used in a broad range of fields, extending from physical sciences and engineering to biology. Since the invention of the SEM, useful resolutions of 7 nm are attainable, and for some instruments, 3 nm can be

58

achieved. The range of electron-induced signals produced in the SEM can yield chemical, physical and morphological informational about the specimen (or sample) [3.6].

The principle of the SEM is based on the production of a high-resolution micrograph produced by focusing a beam of electrons onto the sample. Figure 3.7 presents a schematic representation of the SEM column. As seen in Figure 3.7, the electron gun, situated at the top of the electron column, is normally of the tungsten filament thermionic cathode type, generating a large spread of electrons that diverge outward from the filament tip. These electrons are contained within an electron cloud that accelerates towards an anode-containing sample in the range of 15 to 25 kV, which may vary depending on the type of sample and application [3.6].
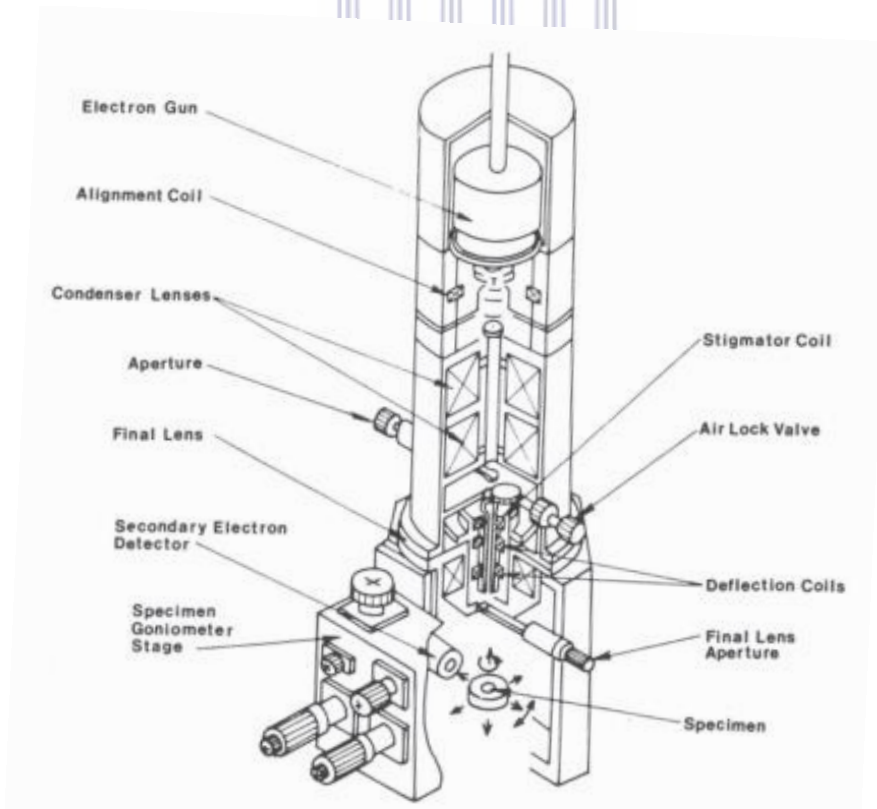

Figure 3.7: Schematic representation of the main components of the SEM column [3.6].

The electromagnetic lenses seen in Figure 3.7 focus the outward spread of electrons. The condenser lens is the first lens that has an effect on the electron beam, causing the beam to converge and pass through a focal point in the column. The condenser lens, in conjunction with the specified accelerating voltage, is the two factors that are mainly accountable for the beam intensity striking the sample and they, in turn, affect the brightness of the micrograph signal from that sample. The beam spreads again below the condenser lens aperture, and the final lens is used to bring the beam into focus by de-magnifying it at the focal point of the sample surface. In addition, a final lens aperture may be employed to reduce spherical aberrations (lens defects) in the final lens [3.6, 3.7].

3.4.1.2 Resolution

A high magnification micrograph produced in microscopy might be seen as useless if the microscope is incapable of delivering equally high resolution. The limit of resolution may be described as the minimum separation at which two objects are seen as different objects. To better understand the basic concept of resolution, Figure 3.8 shows an example of a pair of car headlights that are observed as a single entity from afar; as the car approaches, the headlights appear as two separate objects and become resolved to the onlooker. The same idea applies to microscopy. Mathematically, the limit of resolution is given by Abbe's equation as [3.6, 3.7]:

$$d = 0.612 \, \lambda / n \sin \alpha \qquad (3.1)$$

where

> d is the resolution (should be small)

λ is the wavelength of the energy beam

n is the index of refraction of the medium through which the energy beam travels, and

α is the aperture angle.

The product $n \sin \alpha$ is usually known as the numerical aperture (NA). The importance of Equation (3.1) is that it mathematically describes the limit of resolution for an optical system. If d should be small, it is obvious that λ should decrease or that n or α should increase to obtain the best resolution [3.6, 3.7].
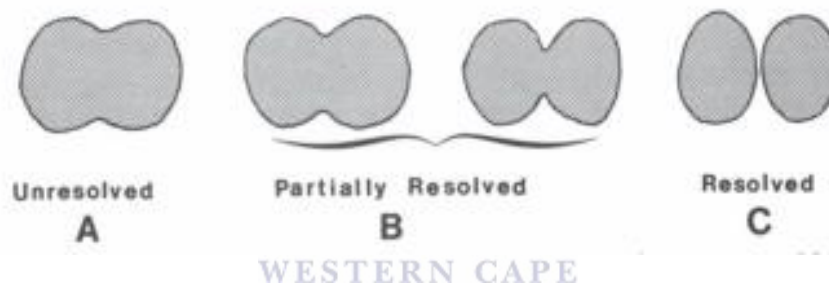

Figure 3.8: Schematic representation of the resolution of two objects using the headlights of an oncoming car as an example. From A to C: the pair of headlights initially appears as one object but, as the car approaches an onlooker, the two objects can be resolved and seen independently [3.6].

3.4.1.3 Depth of Field and Working Distance

In any microscope, the depth of field (DOF) is defined as the degree at which a region of an object appears reasonably in focus. The DOF can be enhanced in the SEM by distancing the sample from the final lens, hence increasing the working distance (WD) and effectively decrease the aperture angle, α, as can be illustrated by Figure 3.9. The space between the final lens pole piece and the topmost part of the sample is termed the WD, as can be seen in Figure 3.9. The consequence of the change in WD on the DOF

61

and resolution is listed in Table 3.1. It is obvious from Table 3.1 and Abbe's equation (see Equation (3.1)) that the conditions enhancing the DOF simultaneously worsen the resolution [3.6, 3.7].
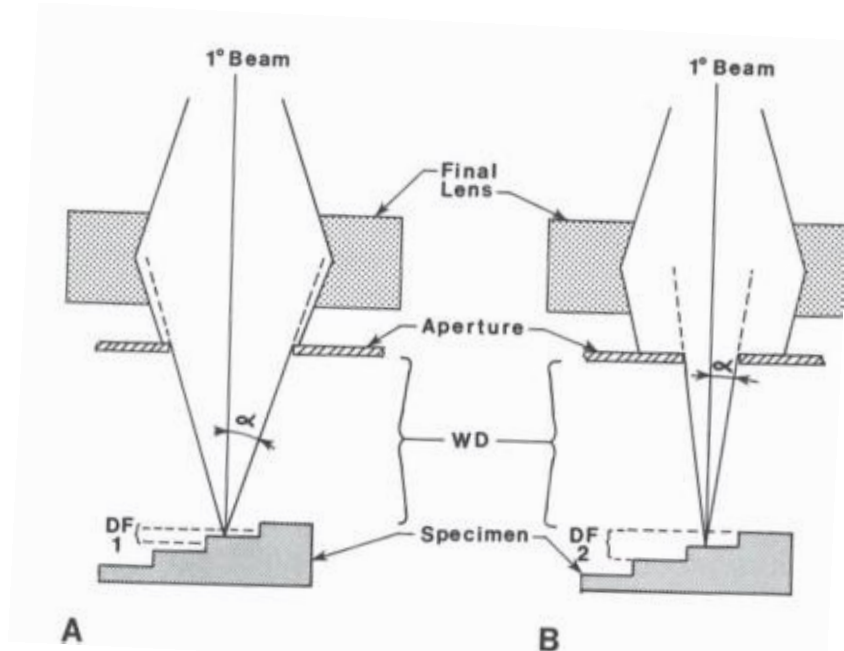

Figure 3.9: Schematic showing the enhancement of depth of field (DOF). (A) Short working distance (WD) and (B) longer WD enhance the DOF and effectively decrease the aperture angle, α [3.6].

Table 3.1: Influence of the Working Distance on Depth of Field and Resolution [3.6].

Working Distance (mm)	5	10	15	30
Depth of field	Shallow	----------------------------------		Deep
Resolution	High	----------------------------------		Low

3.4.1.4 Electron Beam - Specimen Interaction: Signals Produced

When a primary electron beam interacts with a specimen, it creates a volume of primary excitation within the specimen, causing electrons to scatter (see Figure 3.10). Two types of scattering events may occur: elastic or inelastic. Inelastic scattering events, the

62

electrons involved are termed backscattered electrons, because they are scattered back from the specimen surface; they maintain practically all of their energies, and as a result are high-energy electrons. In contrast, in an inelastic scattering event, low energy electrons with energy less than 50 eV, termed secondary electrons, lose much of their energy upon interaction and are formed throughout the volume of primary excitation (see also Figure 3.10). Since secondary electrons possess low energy, adjacent atoms in the specimen absorb them and, as a result, only those near the surface of the specimen are able to escape, whereas backscattered electrons are able to escape from deep within the specimen due to their higher energy [3.6].
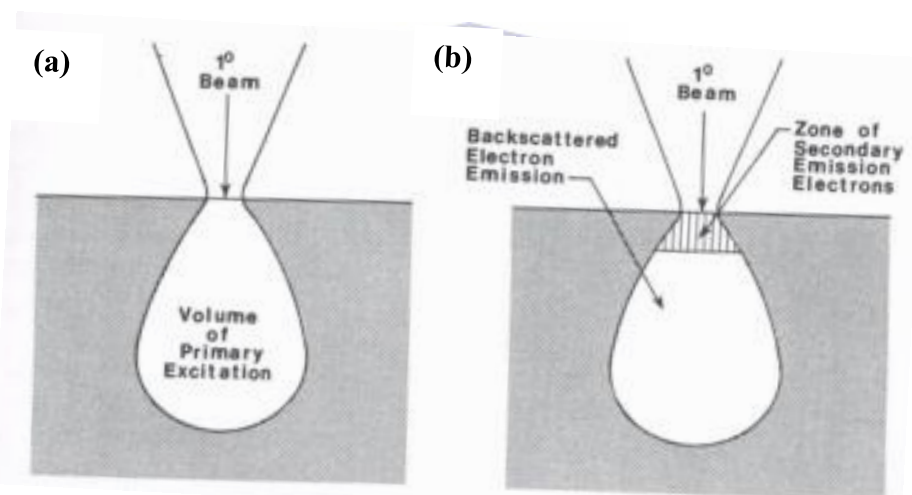
Figure 3.10: Schematic of the interaction between the electron beam and the specimen. (A) Illustration of the volume of primary beam excitation and (B) areas of origins of secondary and backscattered emissions [3.6].

There are, however, more signals generated during the interaction between the solid specimen and the electron beam that may be detected in the SEM, as can be seen in Figure 3.11. In order to obtain an image of the specimen, one might need to collect and display secondary electrons, backscattered electrons, transmitted electrons, or specimen

63

current. To determine the chemical composition of the specimen one might also need to measure cathodoluminescence, or record X-ray, or Auger spectra [3.6].
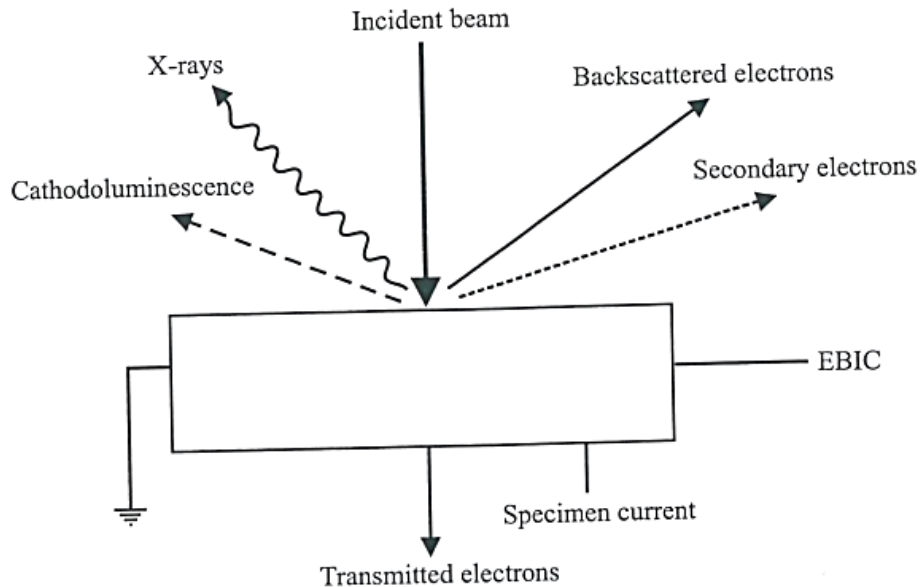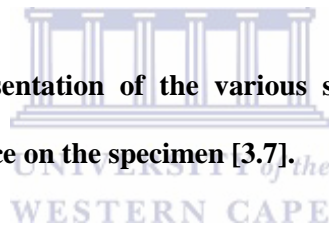

Figure 3.11: Schematic representation of the various signals produced subsequent to primary electron beam incidence on the specimen [3.7].

3.4.1.5 Detecting Secondary and Backscattered Electrons

The secondary and backscattered electrons emitted from the specimen surface in all directions can be detected by a system in the microscope column that is composed of a collector, a scintillator, a light pipe, and a photomultiplier tube, as can be seen in Figure 3.12. The collector has a positive bias that attracts the electrons to a thin plastic disc coated with a distinct phosphor that more efficiently transfers electrons to photons, and is known as the scintillator. This scintillator is also coated with roughly 10 nm of aluminium, acting as a mirror to reflect photons to the photomultiplier. Ultimately, the positive bias (anode) is applied to a ring around the scintillator that is able to accelerate low energy secondary electrons to the detector. The collector does not have an effect on

64

higher energy backscattered electrons, thus the "secondary electron micrograph" is a result of most of the secondary electrons being collected and the backscattered electrons being emitted toward the detector. The flashes of light (photons) formed by the phosphor-containing scintillator are driven through a light pipe and converted outside the microscope column to an amplified electronic signal by means of a photocathode and a photomultiplier tube. The signal is displayed on a cathode ray tube, in which the brightness seen on the screen is relative to the number of secondary electrons emitted from the specimen [3.6].

In order to form an image from the backscattered signals, the secondary electron signal must be prevented from touching the detector by cutting off the positive detector bias. Such microscopes are able to apply a somewhat negative bias to the detector, thus enabling secondary electron repulsion. Other techniques make use of modified scintillator detectors or other accessories [3.6].
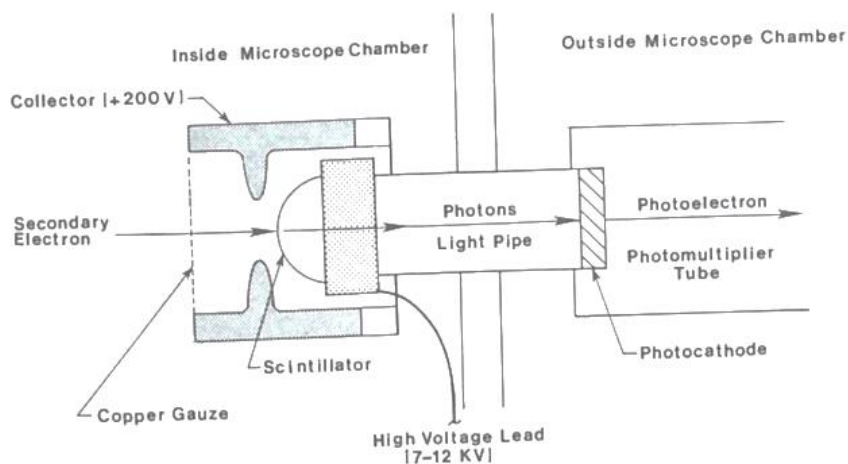

Figure 3.12: Image collection secondary electron detection system [3.6].

3.4.1.6 Characteristic X-rays and Energy Dispersive Spectroscopy (EDS)

As mentioned earlier, the interaction between the electron beam and the specimen produces many signals, including X-rays. From basic physics, it can be explained that the electrons of a given atom occupy distinct energy levels, also known as "shells" (see Figure 3.13). By convention, up to two electrons can occupy the shell closest to the atomic nucleus, which is known as the "K shell". Thereafter, up to 8 electrons are able to occupy the next "L shell", while 18 electrons can occupy the "M shell", and 32 electrons can occupy the "N shell", and so on [3.6].
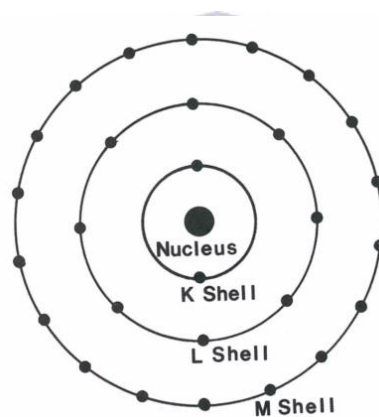
Figure 3.14: Schematic diagram of an atom depicting the electron shells [3.6].

When the beam has knocked out an electron from the K shell, an electron from the next shell will occupy the vacant position. Therefore, the energy difference of the electron from its initial to its final state may be emitted as X-rays; it follows that this energy difference, emitted in the form of X-rays, has a discrete quantity, characteristic of the atom from which it was discharged. X-ray spectroscopy of interest in this work includes quantitative energy dispersive analysis in order to identify the elements and their relative atomic percentages in the sample. A special detector, known as an energy

dispersive spectrometer, that is able to measure the energies of X-rays is needed for this type of analysis [3.6].

The energy dispersion accompanied by X-ray energy analysis involves the separation of X-rays according to their energy, which is currently measured by a semiconductor detector. When an X-ray is incident upon a semiconductor crystal, each electron in the crystal absorbs a particular amount of energy: the higher the energy of the X-ray, the higher the number of electron excitation. The X-ray energy absorbed by the electrons in the crystals is converted to an electrical signal that is emitted and amplified. The strength of the current from the crystal is relative to the X-ray energy. The amplified electrical pulses from the semiconductor are converted to digital form and introduced into a multichannel analyser (MCA), which sorts and counts the number of X-rays at each energy level incident upon the crystal [3.6].
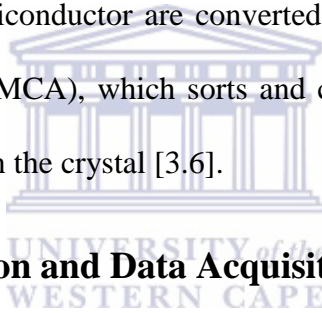
3.4.1.7 Sample Preparation and Data Acquisition

In order to obtain effective micrographs in SEM, the sample needs to be electrically conductive in order to enhance the collection of backscattered and secondary electrons. To satisfy this condition, non-conductive and low-conductive samples are coated with a thin, highly conductive layer of Au or C via sputter coating or thermal evaporation. When the incoming electron beam strikes the sample, there is a build-up of charge that may lead to sample damage. For a non-conductive sample (such as a biological sample), the build-up of charge results in an effect known as charging, which may degrade the resolving power that ultimately produces a low-quality micrograph. However, if the sample is conductive, the effect becomes insignificant, as the charge will be conducted through the sample and eventually grounded by contact with the sample stage.

In this study, SEM was used to evaluate the effect that the Ag catalyst morphology has on the geometry of the resultant MaCE-grown Si NWs and also the effect of n-type doping on the morphology of the MaCE-grown Si NWs. All Ag-coated Si wafers, as-synthesised Si NWs and n-doped Si NWs were coated using a Quorom150 ES gold/palladium (Au/Pd) sputter coater, in which a base pressure of 10^{-4} millibar (mbars) and a deposition pressure of 10^{-2} mbar were maintained. All micrographs were analysed with a Zeiss Auriga field-emission gun scanning electron microscope (FEG-SEM) at the Electron Microscope Unit (EMU) in the Department of Physics and Astronomy at UWC (see Figure 3.14). All EDS spectra were collected and analysed using Oxford Aztec software and an Oxford X-Max solid-state silicon drift detector (SDD), respectively. The SEM was operated at a working distance of 5 mm. Micrographs and EDS measurements were acquired at an accelerating voltage of 5 and 20 kV, respectively.

Figure 3.14: Zeiss Auriga FEG-SEM (EMU, UWC, Cape Town).

3.4.2 Transmission Electron Microscopy

The transmission electron microscopy (TEM) technique differs in principle from SEM, in that the primary electron beam is transmitted through the sample, instead of knocking out secondary electrons from the sample or being backscattered [3.8]. In TEM, the accelerating potential is enhanced to 50 kV, which reduces the electron wavelength to about 5 petameters (Pm) in accordance with De Broglie's relationship [3.9]. These higher energy electrons are able to penetrate into a solid material over distances of several microns (μm). If the solid material is crystalline, then the atomic planes of the material diffract the electrons, producing a transmission electron diffraction pattern. Due to the smaller wavelength of the transmitted electrons, the sample can be imaged at a higher spatial resolution in comparison to SEM. Modern TEMs are capable of producing accelerating voltages between 100 and 300 kV, thus regularly reaching spectral resolutions of 0.1 nm (1 angstrom (Å)) [3.8].

Image formation during TEM can be explained by means of two stages, namely elastic and inelastic scattering. The incoming electrons undergo interactions with the atoms of the sample, resulting in the aforementioned scattering processes. The electron wave function leaving the surface of the sample is first transferred through the objective lens and then through the intermediate lenses of the electron microscope to produce the final enlarged image [3.8], as can be seen in the schematic diagram of the TEM in Figure 3.15.
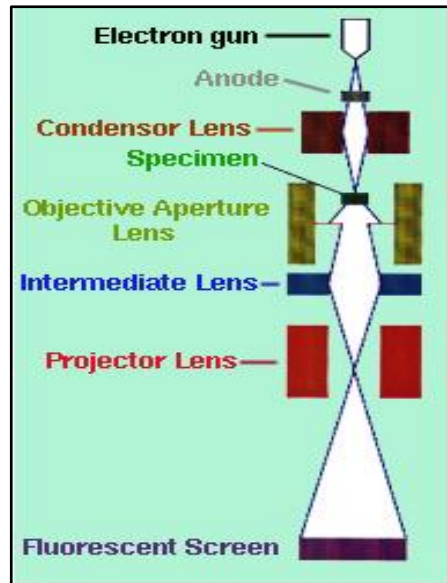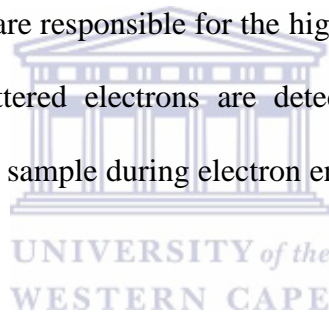
Figure 3.15: Schematic diagram of the transmission electron microscope [3.10].

Elastically scattered electrons are responsible for the high-resolution TEM micrographs, whereas the inelastically scattered electrons are detected and analysed to produce valuable information about the sample during electron energy loss spectroscopy (EELS) [3.8].

TEM was used to study the structural properties of the MaCE-grown Si NWs and n-doped Si NWs. For TEM analysis, the samples need to be thin enough for electrons to be transmitted and to allow for good imaging. For the preparation of the TEM samples, the Si NWs were mechanically removed from the substrates and dispersed in ethanol by means of ultra-sonication. The solution was then dropped cast onto a copper (Cu) grid covered by a thin amorphous C layer and thereafter inserted into the instrument for analysis. All results were obtained using the Technai $G^2 20$ field emission gun transmission electron microscope (FEG-TEM), operated at 200 kV. Figure 3.16 shows the FEG-TEM used at the Electron Microscope Unit (EMU) at UWC.

70

 In order to obtain a single precise interplanar spacing (d) from the high-resolution TEM (HR-TEM) micrographs to determine the Si NW preferred-growth orientation, five consecutive spacing's were averaged using the ImageJ image processing program. The selected area electron diffraction (SAED) patterns were indexed using the NBS monograph [3.11], and the lattice constant (a) values obtained from the SAED patterns were averaged across three interplanar spacing (d) values measured using the ImageJ program.

Figure 3.16: Technai G²20FEG-TEM (EMU, UWC, Cape Town).

3.4.3 X-Ray Diffraction

3.4.3.1 Basic Theory of X-Ray Diffraction

X-rays are classified as electromagnetic waves with energies in the range of about 100 eV to 10 megaelectron volts (MeV); they differ from radio waves, light, and gamma rays in terms of wavelength and energy. X-rays exhibit a wave-like nature with a wavelength in the range of about 10 to 103 nm. Atoms that are the basis of a crystal generate X-rays with a similar wavelength as that of the incoming X-ray beam by oscillating electrons, whereas the generated X-rays are most likely to be spherical waves centring on the individual atoms [3.12]. X-ray diffraction (XRD) is a technique that may be used to determine the structural properties, chemical analysis, particle size and the stress measurement of materials [3.13]. In this study, XRD is used to study the structural properties of the MaCE-grown Si NWs and n-doped Si NWs.

The main objective of X-ray diffraction by crystals is to recognise the specific condition under which the incoming and scattered X-rays are entirely in phase, and in which they thus strengthen each other in order to produce a detectable diffraction beam. For this reason, the most significant and well-known law is given by Bragg's law, which includes the Bragg angle. Bragg's law is illustrated in Figure 3.17. If the incoming X-ray beam of wavelength (λ) is incident upon a crystal, with atoms arranged in a regular periodic array with lattice spacing d', a diffraction beam of sufficient intensity is detected only if the "Bragg condition", in other words, Bragg's law, is satisfied such that [3.12]:

$$2d' \sin \Theta = n\lambda \tag{3.2}$$

where *n* is the order of reflection and is given as the number of wavelengths in the path difference between diffracted X-rays from neighbouring crystal planes (see Figure 3.17). For a fixed value of λ and *d* ′, diffraction takes place at a number of incident angles, such as Θ_1, Θ_2, Θ_3, … , corresponding to *n* = 1, 2, 3 …. In the first order of reflection, where *n* = 1, the path difference between two scattered X-rays is indicated by 1' and 2' in Figure 3.17 as one wavelength. In contrast, the path difference between two scattered X-rays is indicated by 1' and 3' as two wavelengths, etc. If the X-rays diffracted from all the atomic planes are entirely in phase, such that an X-ray beam is diffracted with intensity in a specific direction, it satisfies Bragg's law. Equation 3.2 may be rewritten as [3.12],

$$2d \sin \Theta = n\lambda \tag{3.3}$$

where $d = d'/n$. This is the most common form of Bragg's law.
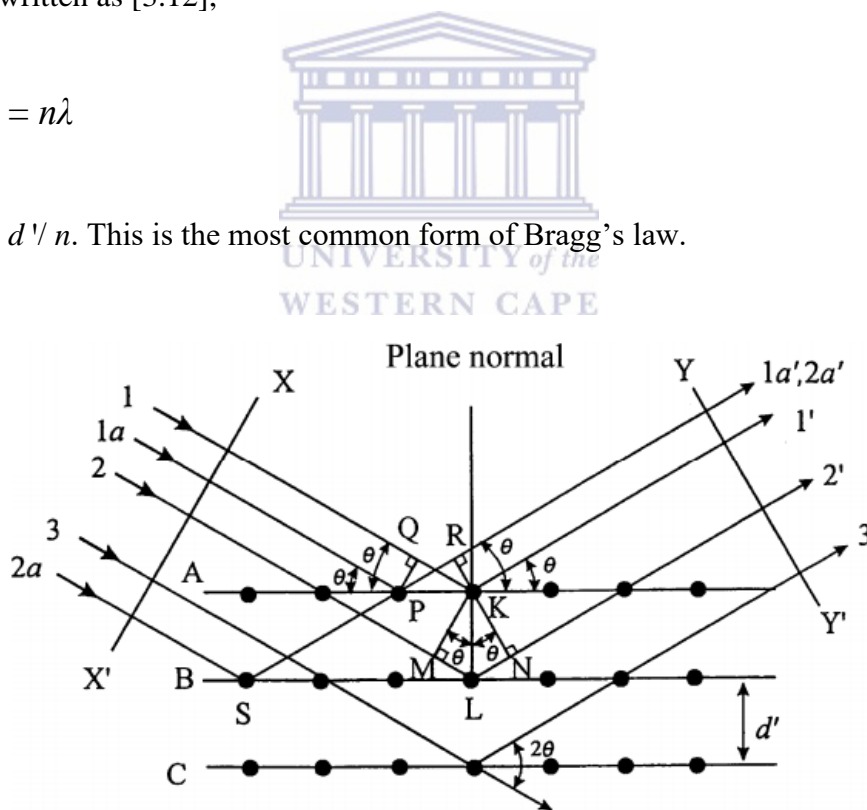

Figure 3.17: Schematic of X-ray diffraction by a crystal (Bragg's condition) [3.12].

In general, the nth order of reflection from a specific crystal plane (*hkl*) with interplanar spacing *d*, is considered the first order of reflection from a plane (*nh nk nl*). And since

the (*nh nk nl*) plane is parallel to the (*hkl*) plane, reflection from the (*nh nk nl*) plane is equal to the first order reflection from planes that are spaced at a distance of $d = d'/n$. In this way, the diffraction angle in most cases is considered to be 2Θ. The diffraction angle 2Θ may be determined by relating Equation 3.3 (Bragg's law) and the plane-spacing equations seen in Table 3.1 that relates the interplanar spacing to the lattice parameters and the Miller indices for each type of crystal. For example, for a cubic crystal with lattice parameter (*a*), the interplanar spacing (*d*) and Miller indices (*hkl*) are given by [3.12]:
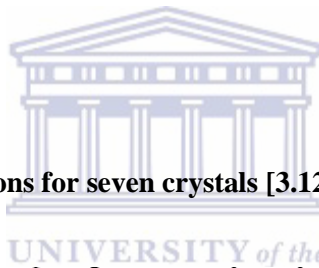
$$1/d^2 = (h^2 + k^2 + l^2)/a^2 \qquad\qquad (3.4)$$

Table 3.1: Plane-spacing equations for seven crystals [3.12].

Cubic	$\frac{1}{d^2} = \frac{h^2+k^2+l^2}{a^2}$
Tetragonal	$\frac{1}{d^2} = \frac{h^2+k^2}{a^2} + \frac{l^2}{c^2}$
Hexagonal	$\frac{1}{d^2} = \frac{4}{3}\left(\frac{h^2+hk+k^2}{a^2}\right) + \frac{l^2}{c^2}$
Trigonal	$\frac{1}{d^2} = \frac{(h^2+k^2+l^2)\sin^2\alpha + 2(hk+kl+hl)(\cos^2\alpha - \cos\alpha)}{a^2(1-3\cos^2\alpha + 2\cos^3\alpha)}$
Orthorhombic	$\frac{1}{d^2} = \frac{h^2}{a^2} + \frac{k^2}{b^2} + \frac{l^2}{c^2}$
Monoclinic	$\frac{1}{d^2} = \frac{1}{\sin^2\beta}\left(\frac{h^2}{a^2} + \frac{k^2\sin^2\beta}{b^2} + \frac{l^2}{c^2} - \frac{2hl\cos\beta}{ac}\right)$
Triclinic	$\frac{1}{d^2} = \frac{1}{V^2}(S_{11}h^2 + S_{22}k^2 + S_{23}k^2 + 2S_{12}hk + 2S_{23}kl + 2S_{13}hl)$

On the triclinic system, V is the volume of a unit cell and the coefficients are given below.

$$S_{11} = b^2c^2\sin^2\alpha, \qquad S_{12} = abc^2(\cos\alpha\cos\beta - \cos\gamma),$$
$$S_{22} = a^2c^2\sin^2\beta, \qquad S_{23} = a^2bc(\cos\beta\cos\gamma - \cos\alpha),$$
$$S_{33} = a^2b^2\sin^2\gamma, \qquad S_{13} = ab^2c(\cos\gamma\cos\alpha - \cos\beta)$$

3.4.3.2 The X-Ray Diffractometer

XRD patterns are acquired by using an X-ray diffractometer as shown in Figure 3.18. The diffractometer is composed of three main parts, namely [3.3, 3.8, 3.12]:

- The X-ray source (indicated by *S* and *T* in Figure 3.18)

- The diffractometer circle and

- The detector system (indicated by *G* and *E* in Figure 3.18)

The detector (*G*) is positioned at the circumference of the diffractometer circle centred at the sample stage, *C*. The sample is supported by a horizontal table *H*, which can rotate about its axis *O*, perpendicular to this page. X-rays are diverged from the source at *S* and diffracted by the sample at *C* to produce a convergent diffracted beam, which focuses at the slit *F* prior to entering the detector at *G* that is supported on a carriage, *E*. The carriage with angular position 2Ө also rotates about the axis O. The supports indicated as *H* and *E* is mechanically sealed in a Ө-2Ө connection. The unique slits indicated as *A* and *B* in Figure 3.18, define and collimate the incident and diffracted X-ray beams. A filter is located in the diffracted beam-path to suppress the K-beta (K$_\beta$) radiation and to minimise the background radiation coming from the sample.
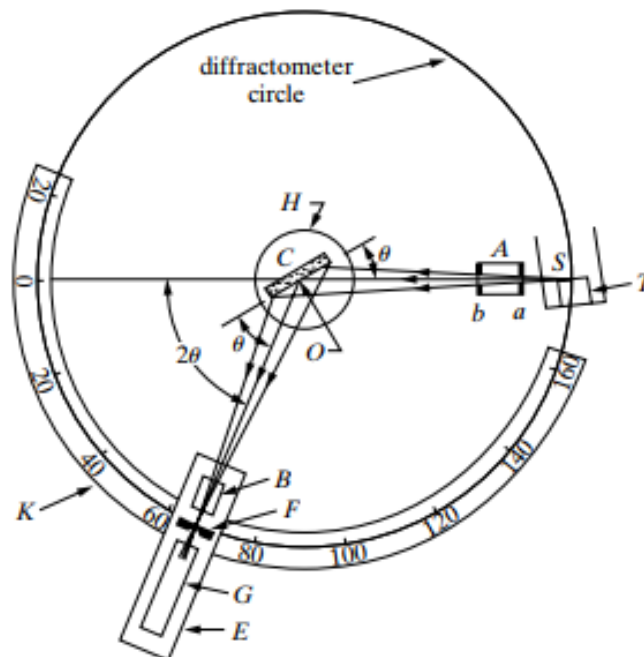

Figure 3.18: X-ray diffractometer [3.12].

3.4.3.3 Data Acquisition

XRD patterns were obtained by means of an Empyrean XRD system from PANalytical in grazing incidence geometry at the National Metrology Institute of South Africa (NMISA) in Pretoria. Figure 3.19 illustrates the Empyrean XRD system. The patterns were recorded at room temperature (25 °C) in 2Θ range between 15° and 90° with a step size of 0.02^o. Cu K-alpha 1 (Kα_1) radiation with a wavelength of 1.5406 Å was used as the X-ray source, operated with a voltage and current of 45 kV and 40 milliamperes (mA), respectively. The divergence slit was fixed at 0.01 millimetre (mm) to ensure that the measured spot was smaller than the sample size ($\sim 1 \times 1$ cm^2). PANalytical X' PERT Data Collector and X' PERT HighScore software were used for data acquisition and evaluation, respectively. Hence the interplanar spacing (*d*), peak position 2Θ and the full width at half maximum (FWHM) parameters were readily obtained and did not need any calculation. The XRD patterns were indexed using the NBS monograph [3.11]. The lattice parameter (*a*) values were calculated by re-arranging the plane spacing equation (see Equation 3.4). The XRD patterns were plotted using the OriginPro 8.5.1 software.

Figure 3.19: Empyrean XRD system (NMISA, Pretoria).

3.4.4 X-Ray Photoelectron Spectroscopy

X-ray photoelectron spectroscopy (XPS) is a technique widely used to study the chemical composition of surfaces. During XPS surface analysis, a sample is irradiated with monochromatic soft X-rays, of which Al k_α radiation (1486.7 eV) is often used. When the X-rays are incident upon the surface atoms of the sample, electrons are emitted via the photoelectron effect. The emitted photoelectrons have kinetic energies expressed as [3.13]:

$$KE = hv - BE - \sigma_S \qquad (3.5)$$

where hv is the energy of the incoming X-ray photon, BE is the binding energy of the atomic orbital of the initial position of the electron and σ_S is the work function of the spectrometer. The BE is given as the energy difference between the initial and final states of the photoelectron upon leaving the atom and is characteristic for each atom. In general, elemental quantification is obtained by using the area and height of the particular energy peaks [3.13].

Methods involving peak area sensitivity factors are normally more accurate and frequently used. The number of atoms n of the element per cm^3 of a homogeneous sample is expressed as [3.13]:

$$n = I / f\sigma\Theta y\lambda AT \qquad (3.6)$$

where I is the number of photoelectrons per second for a particular peak within the spectra, f is the X-ray flux in units of photons/cm^2/s, σ is the photoelectron cross-section of the particular atomic orbital in units of cm^2, Θ is the angular efficiency factor of the detector that is based on the arrangement of the instrument, y is the efficiency of the

photoelectric process that is based on the production of photoelectrons within the sample, A is the sample area from which the photoelectrons are detected, λ is the electron mean free path of the photoelectrons in the sample, and T is the detection efficiency of electrons emitted from the sample. The denominator of Equation (3.6) is better known as the atomic sensitivity factor S [3.13].

For that reason, the XPS technique is capable of qualitative and quantitative chemical composition analysis of the surfaces of samples. In certain XPS systems, elemental depthprofiling is possible. Depth profiling involves the removal of atomic layers of the sample surface by sputtering it with Ar ions. This is done by sputtering the surface of the sample sequentially to obtain elemental composition information within the sample [3.13].

XPS was used to evaluate the chemical composition of the surfaces of the n-doped Si NWs annealed at 1000 °C and the location of the P dopants within the sample. The analysis was carried out at an ambient temperature of 20 ± 5 °C and a relative humidity (RH) of 50 ± 25%. The chemical composition of the surface was characterised using a Thermo ESCAlab 250Xi X-ray photoelectron spectrometer with a scanning monochromated Al k_α source (1486.7 eV; 80 W; spot size, 300 μm). Figure 3.20 shows a pictorial of the Thermo ESCAlab 250Xi X-ray photoelectron spectrometer located at NMISA in Pretoria. The X-ray beam collected elemental information relating to O 1s, Si 2p, C 1s, N 1s, P 2s, and F 1s. Detailed XPS acquisition parameters (chemical states of the elements) were identified from the NIST database [3.13]. Depth profiling was accomplished by using the instrument's Ar$^+$ ion source. XPS depth profiles were acquired after each sputtering time of 0 s, 48 s, and 1068 s, respectively. The data were plotted using the OriginPro 8.5.1 software.

Figure 3.20: (Thermo ESCAlab 250Xi X-ray photoelectron spectrometer NMISA, Pretoria).

3.4.5 Hall Effect Measurement Technique

3.4.5.1 Introduction

The Hall effect occurs when a current carrying semiconductor or conductor is placed in a magnetic field perpendicular to the current [3.15, 3.16]. Consequently, the magnetic field deflects the charge carriers within the conductor (or semiconductor), giving rise to an electric field, owing to the voltage induced by the separation of negative and positive carriers, which is known as the Hall field. The Hall field is perpendicular to both the current and the magnetic field. The Hall field can point along whichever direction of the axis it exist in. It should be noted that, at sufficient temperature, the net current within a semiconductor is composed of counteracting currents of n-type and p-type carriers

79

[3.15]. And for that reason, the Hall effect measurement technique is useful for analysing the electrical conducting properties of semiconductors [3.16].

3.4.5.2 Theory

Electric current in a semiconductor is composed of charged carriers known as electrons and holes. When these charged carriers experience a force owing to a magnetic field that is applied perpendicular to their movement, they experience a Lorentz force, given by [3.15, 3.16]:

$$\boldsymbol{F}_L = -q\boldsymbol{v}\boldsymbol{B} \tag{3.7}$$

This results in mobile charged carriers accumulating on one face of the material, leaving equal and opposite charges exposed on the other face, where there is a scarcity of mobile charges. Due to the separation of charges, an electric field ($\boldsymbol{E}$) is formed between these two faces. Immediately, the electric field ($\boldsymbol{E}$) produces a force $\boldsymbol{F} = q\boldsymbol{E}$, which cancels the Lorentz force. Once equilibrium between the two forces is reached, a voltage difference is recognised across the faces of the material. This transverse voltage difference is better known as the Hall voltage V_H. The sign of V_H is dependent upon whether the carriers are primarily negatively (electrons) or positively (holes) charged [3.16]. Therefore, by measuring V_H we can identify whether we have an n-type or p-type semiconductor material [3.15]. In this study, the charge carriers in the Si NW samples are the electrons (negatively charged). In other words, the Si NW samples are n-type. So, if the samples are n-type, V_H is negative, and is determined through:

$$V_H = -\boldsymbol{I}\boldsymbol{B} / qnd \tag{3.8}$$

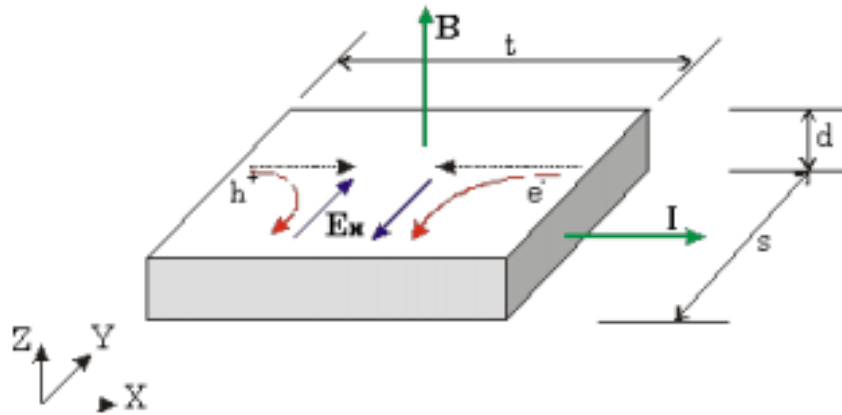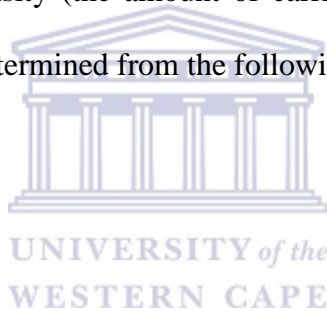Figure 3.21 presents a schematic of the Hall effect theoretical model.

Figure 3.21: Hall effect geometry [3.15].

From V_H the sheet carrier density (the amount of carriers in the dopant layer) of the conducting material may be determined from the following expression [3.16]:

$$n_s = IB \, / \, qV_H \tag{3.9}$$

where I = current

   B = applied magnetic field

   q = charge of free carriers

   V_H = Hall voltage.

The bulk carrier density of the material is acquired once the thickness (d) of the sample is known; it is obtained by using and re-arranging the expression, $n_s = nd$ [3.16]. In this study, the lengths of the n-doped Si NWs are taken as the thickness (d). SEM analysis later on in this work will interrogate the length measurements (See Chapter 4, Sections 4.2.1.2 and 4.2.1.3). Other important parameters of interest in this study are the Hall mobility (μ_H) and the bulk resistivity (ρ). The Hall mobility is acquired by using

81

Equation (3.10), whereas the bulk resistivity (ρ) is obtained by using Equation (3.11) subsequent to obtaining the sheet resistance (R_s) from Equation (3.10) [3.16].

$$\mu_{sheet} = V_{\text{H}} / R_s I\boldsymbol{B} = 1 / qn_s R_s \tag{3.10}$$

$$\rho = R_s d \tag{3.11}$$

3.4.5.3 Data Acquisition

In this study, the temperature dependence of electrical transport properties using the Hall effect measurement technique on the n-doped Si NWs annealed at 700, 800, 900, and 1000 °C was interrogated. The electrical transport properties were acquired at UWC using the Ecopia HMS-3000 Hall Effect Measurement System with a 0.55 tesla (T) permanent magnet operating at room temperature. Figure 3.22 illustrates the system used in this study. Six stages of the input current of 50, 100, 250, 500, 750, and 1000 µA were applied to reduce the error allowance to a minimum.

The system is fully automated and computer-controlled to enable it to derive the Hall mobility (μ_H), the charge carrier density (n) and the resistivity (ρ). In this study, we simply refer to the Hall mobility (μ_H), the charge carrier density (n) and the resistivity (ρ) as the mobility (μ), the dopant concentration (N_D) and the resistivity (ρ), respectively.
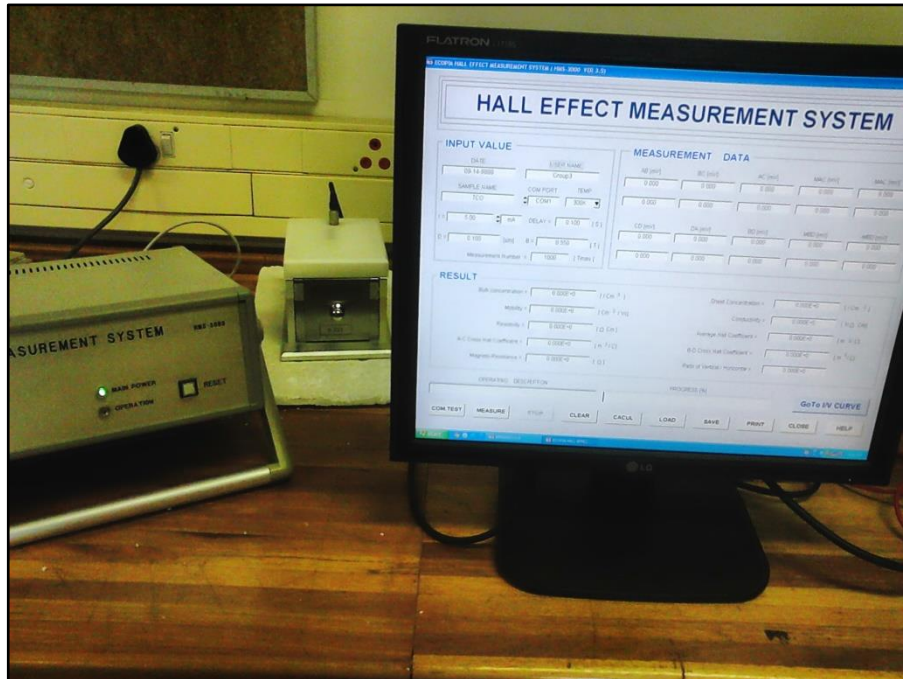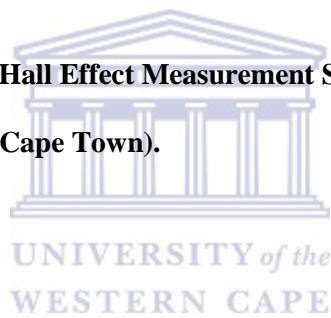
Figure 3.22: Ecopia HMS-3000 Hall Effect Measurement System (The Department of Physics and Astronomy, UWC, Cape Town).

3.5 References

[3.1]Spin Coater KW4A.2017.Available:http://www.chemat.com/chematscientific/KW-4A.aspx [2016, November 5].

[3.2]2016.Available:http://www.chemat.com/chematscientific/docspdf/spin_coater_kw-4a_manual.pdf [2016, November 5].

[3.3]   Khanyile, S. (2015). Deposition of silicon nanostructures by thermal chemical vapour deposition. MSc Thesis. University of the Western Cape.

[3.4]   Boer, H. (1999). Precision mass flow metering for CVD applications. Le Journal de Physique, 4(5), 869.

[3.5] MKS Instruments – Process Control

Solutions.2016.Available:http://www.mksinst.com [2016, November 19].

[3.6]   K. Howard, A. Johnson, K. McMichael and M.T. Postek. (1980). Scanning Electron Microscopy – A Students Handbook. Ladd Research Industries, Inc., Burlington.

[3.7]   P.J. Goodhew and F.J. Humphreys. (Ed.). (1988). Electron Microscopy and Analysis. (2nd ed.). Taylor & Francis, London.

[3.8]   Cummings, F. (2012). TiO_2 based dye-sensitised solar cells. PhD Thesis. University of the Western Cape.

[3.9]   2017. Available: http://www.phys.nthu.edu.tw/~thschang/notes/GP41.pdf [2017, April 10].

[3.10]ElectronMicroscopy.2017.Available:http://sv.rkriz.net/classes/MSE2094_NoteBook/96ClassProj/experimental/electron.html [2017, April 23].

[3.11] Morris, M.C., McMurdie, H.F., Evans, E.H., Paretzkin, B., de Groot, J.H., Hubbard, C.R., and Carmel, S.J. (1976). Standard X-ray Diffraction Powder Patterns. Washington: U.S. Government Printing office.

[3.12] Waseda, Y., Matsubara, E., and Shinoda, K. (2011). X-ray diffraction crystallography. London: Springer.

[3.13] Oliphant, C. (2012). Hot-wire chemical vapour deposition of nanocrystalline silicon and silicon nitride: growth mechanisms and filament stability. PhD Thesis. University of the Western Cape.

[3.14] NIST X-ray Photoelectron Spectroscopy (XPS) Database, Version 3.5. 2017. Available: http://srdata.nist.gov/xps/ [2017, August 18].

[3.15]2017.Available:http://experimentationlab.berkeley.edu/sites/default/files/writeups/SHE.pdf [2017, August 19].

[3.16] Lebogang, K. (2010). Fabrication and characterization of a solar cell using an aluminium P-doped layer in the hot-wire chemical vapour deposition process. PhD Thesis. University of the Western Cape.

Chapter Four: Results and Discussions

4.1 Introduction

As previously outlined in Chapter 1, Sections 1.7, the metal-assisted chemical etching (MaCE) top-down fabrication technique is employed in this study to form silicon nanowires (Si NWs). Given the increased necessity and scarcity of high-quality Si materials, it is essential to use novel materials that are inexpensive for photovoltaic (PV) applications [1.30]. Si NWs produced from the MaCE process is a potential candidate that can be used as a low-cost alternative for PV applications [1.31]. In this study, the two-step MaCE process is used, in which the silver (Ag) metal catalyst is coated onto a Si wafer before proceeding with anisotropic etching in an oxidant/hydrofluoric (HF) solution to form the resultant Si NWs.

The morphological properties of the silver nanoparticles (Ag NPs) are dependent on the coating conditions, such as coating solution temperature, silver nitrate (AgNO$_3$) concentration, and coating time [4.1]. If the Ag NPs are relatively high in density such that it overlaps or if the distance between Ag metal particles is minimal (i.e. an increased Ag NP coverage), Si NWs may form. The increased surface coverage is a result of higher surface density and, to a small degree, Ag NP size, which ultimately depends on a higher coating solution temperature, larger AgNO$_3$ concentration or longer coating time. As a result, the geometry of the resultant etched Si structures grown by MaCE is generally affected by the initial morphology of the Ag NP coverage and the

86

distance between the Ag NPs [1.21, 1.23]. Hence, it is necessary to report on the effect that the morphology of the Ag metal catalyst (i.e. Ag NPs) has on the resultant MaCE-grown Si NWs.

As stated in Chapter 2, Section 2.1, thermal diffusion of phosphorus (P) in Si is the main method for emitter formation in Si solar cell (SC) processing. The thermal diffusion of phosphorus is required to form an n-type emitter to the p-type wafer. P-type Si wafers are extensively employed in solar industries and for that reason diffusion technologies have been developed to deposit n-type dopants to form p-n junctions [2.3]. In this study, the diffusion annealing technique of bulk p-type Si is adapted in order to produce n-doped MaCE-grown Si NWs by using a phosphorus-containing spin-on dopant (SOD) source for the post-deposition technique. There is limited understanding of the precise diffusion procedure of coating a SOD to MaCE-grown Si NWs, as most studies have thus far focused on understanding the diffusion mechanism in the vapour-liquid-solid (VLS)-grown Si NWs. This study seeks to contribute to the development, cost reduction, and understanding of depositing a phosphorus-containing SOD to MaCE-grown Si NWs.

In this chapter, the effect of the initial morphology of the Ag NPs on the resultant etched Si structures grown by MaCE will be interrogated. Also, the effect of n-type doping on the morphological, structural, compositional and electrical transport properties of MaCE-grown Si structures will be studied. This chapter begins by studying the effects of the initial morphology of the Ag NPs on the MaCE-grown Si NWs.

4.2   Morphology Characterisation

In this section, the scanning electron microscopy (SEM) characterisation technique was employed to study the effect that the initial Ag catalyst morphology has on the geometry of the resultant etched Si structures (i.e. Si NWs) grown by MaCE, in conjunction with energy dispersive spectroscopy (EDS) to study the elemental composition of the Ag catalyst, MaCE-grown Si NWs, and n-doped Si NWs. The SEM technique was employed in conjunction with the transmission electron microscopy (TEM) characterisation technique to study the effect of n-type doping on the morphology of MaCE-grown Si NWs.

4.2.1 Scanning Electron Microscopy Characterisation

4.2.1.1 Ag Catalyst Morphology

The Ag-coated Si wafer, illustrated in Figure 4.1 (a), was intentionally prepared under the experimental conditions as explained in Chapter 3, Section 3.2 to meet the required morphological features seen in Figure 4.1 (a). The semi-spherical and densely-packed Ag NPs coated onto the p-type single-crystalline (100) Si wafer has a mean particle size of 167 ± 23 nm and a relatively uniform size distribution, as indicated and confirmed by the corresponding size distribution curve of the Ag NPs in Figure 4.1 (b). The measured EDS spectrum of the Ag-coated Si wafer (see Figure 4.1 (c)) was obtained by scanning the entire surface area of the top-view SEM micrograph, as seen in the inset of Figure 4.1 (c). The EDS spectrum of the Ag-coated Si wafer confirms the presence of Ag and Si. Carbon (C), gold (Au), and palladium (Pd) are the only other visible peaks in the spectrum due to Au/Pd sputter coating and the use of carbon conductive tape, onto which the Si wafer was deposited during preparation for SEM characterisation.
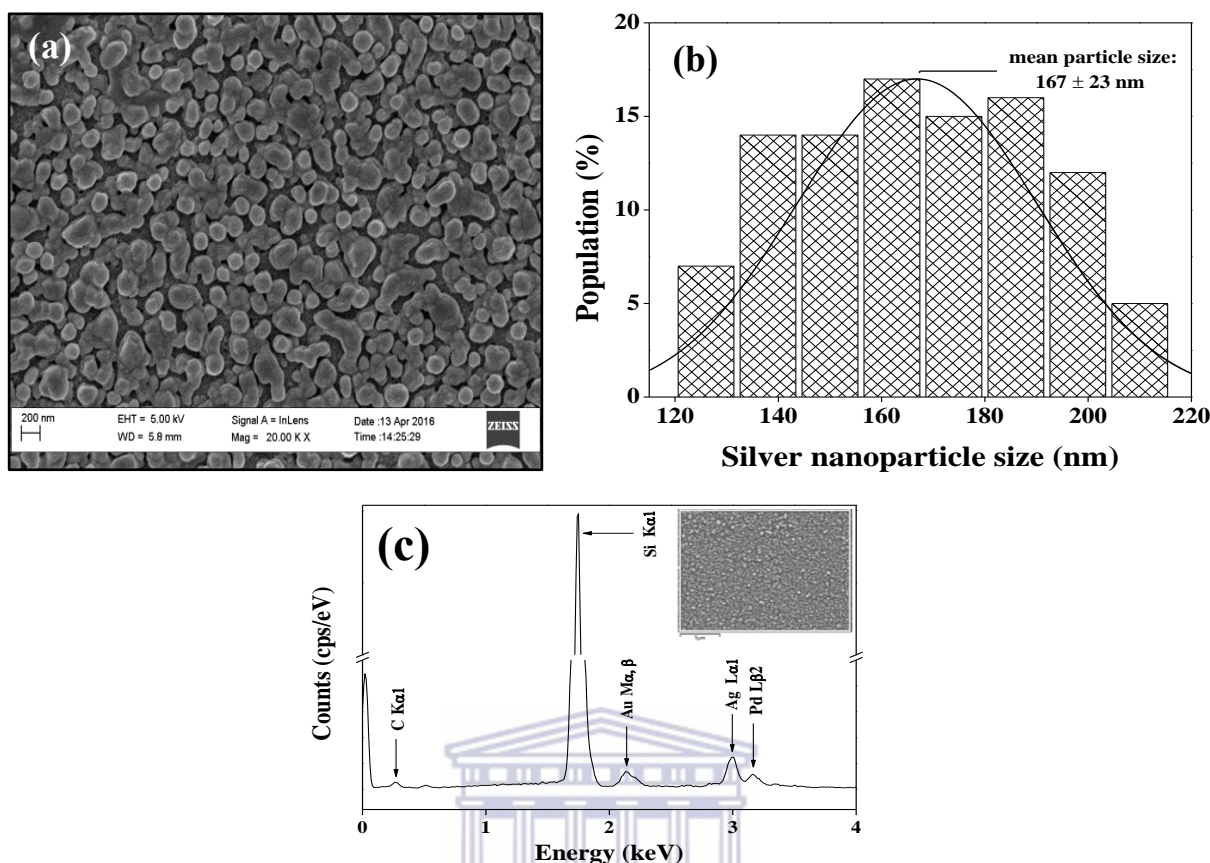
Figure 4.1: (a) Top-view SEM micrograph, (b) size distribution curve, and (c) EDS spectrum with corresponding scan area analysis on a top-view SEM micrograph of Ag NPs coated onto the Si wafer grown by MaCE.

4.2.1.2 As-synthesised Si NWs Morphology

The top-view and cross-sectional SEM micrographs of Figures 4.2 (a) and (b) are representative of the resultant as-synthesised Si NWs with a mean diameter and length of 128 ± 18 nm and 8.28 ± 0.47 μm, respectively. The dark hollow and bright projected areas seen in Figure 4.2 (a) are those of the Ag NPs in the etched regions and of the Si NWs in the unetched regions, respectively. It is apparent from Figure 4.2 (a) that the Si NWs accumulate at the tips to form a 'cone-like' geometry. The bundle formation may be due to the capillary action during the MaCE drying process, as a result of high-aspect-ratio Si NWs [1.20].

89

The etching of Si as a result of the ongoing sinking of the Ag NPs in the presence of the oxidant in the etched regions and the simultaneous unaffected Si in the unetched regions resulted in the presence of Ag NPs at the Si NW/wafer interface (indicated by the arrow) and the Si NW growth normal (i.e. vertically aligned Si NWs) to the wafer surface, as can be seen in Figure 4.2 (b).

It has been hypothesised that the MaCE process is isotropic and that the metal catalyst always promotes the etching along the vertical direction relative to the wafer surface. It has been proved in relation to (100) and (111) wafers, although it was subsequently proved otherwise in the case of (111) and (110) wafers. The etching in a certain preferred crystallographic direction is ascribed to the back-bond breaking theory. This may be described as follows: In order for surface Si atoms to be dissolved or oxidised, it is essential to break the back-bonds of the surface atoms that link to the atoms below. The greater the back-bond strength, the more difficult it becomes to remove the surface atoms. Now, the crystallographic orientation of the starting Si wafer determines the number of Si atom back-bonds. In this study, each atom on the surface of the (100) Si surface plane has two back-bonds, while the atoms on the (110) or (111) wafer have three. As a result of the back-bond strength, the Si atom on the (100) plane is more easily removed [1.23], hence the presence of vertically aligned Si NWs evident in the cross-sectional micrograph of Figure 4.2 (b) infers that the etching is isotropic and that it grows along the <100> direction.

The measured EDS spectrum of Figure 4.2 (c) acquired from the EDS scan area analysis taken at the interface of the cross-sectional SEM micrograph of the Si NWs prior to the removal of the Ag NPs at the Si NW/wafer interface (inset of Figure 4.2 (c)) confirms the presence of Ag situated at the Si NW/wafer interface.
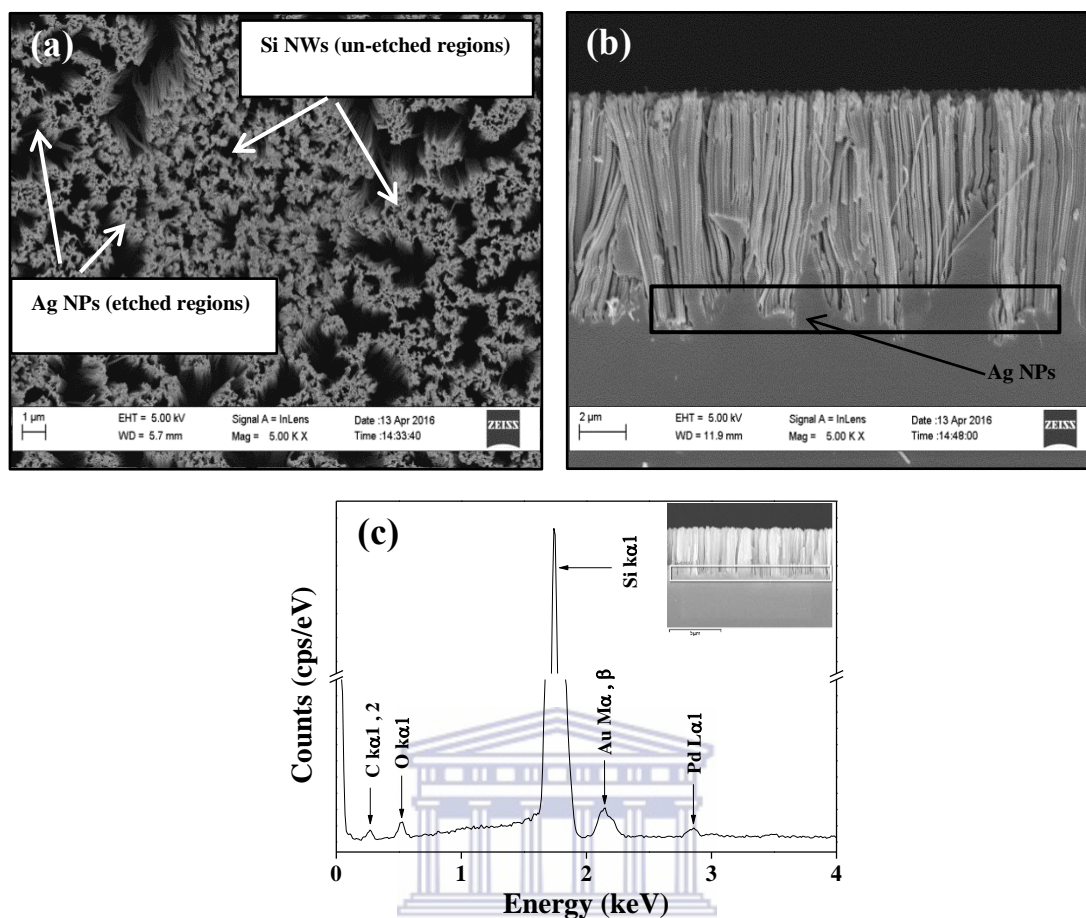
Figure 4.2: Top-view (a) and (b) cross-sectional SEM micrographs of Si NWs prior to the removal of the Ag NPs at the Si NW/wafer interface; (c) Measured EDS spectrum and corresponding EDS scan area analysis taken at the interface of the cross-sectional SEM micrograph of the Si NWs.

To remove the Ag NPs at the Si NW/wafer interface, the Si NWs observed in Figures 4.3 (a) and (b) were placed into a nitric acid (HNO$_3$) solution, as specified in Chapter 3, Section 3.2. A mean diameter and length of 133 ± 22 nm and 8.21 ± 0.27 μm were obtained for the resultant Si NWs, respectively. It appears that the mean diameter and length measurements of the Si NWs prior and subsequent to HNO$_3$ treatment remain constant when the standard deviation is taken into account. The same 'cone-like' and cluster formation that was seen in Figure 4.2 (a) for the Si NWs prior to the removal of the Ag NPs at the Si NW/wafer interface is apparent in the top-view SEM micrographs

91

of Figure 4.3 (a). However, for the cross-sectional SEM micrograph of the Si NWs seen in Figure 4.3 (b), no significant traces of Ag NPs are present at the Si NW/wafer interface.
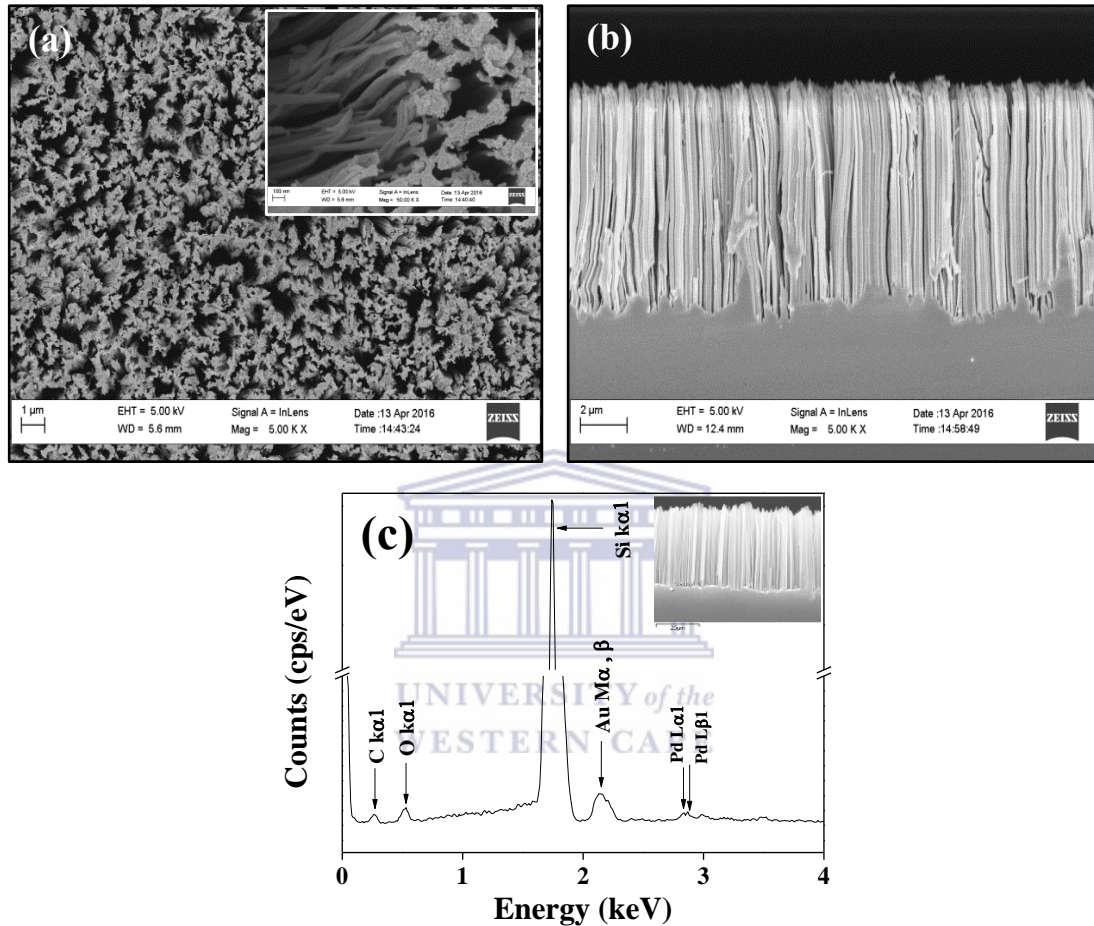

Figure 4.3: Top-view (a) and (b) cross-sectional SEM micrographs of Si NWs subsequent to the removal of the Ag NPs at the Si NW/wafer interface; (c) The measured EDS spectrum with corresponding EDS spot analysis taken at the interface of the cross-sectional SEM micrograph of the Si NWs.

This is confirmed by the measured EDS spectrum of Figure 4.3 (c) acquired from the corresponding EDS spot analysis taken at the interface of the cross-sectional SEM micrograph of the Si NWs subsequent to the removal of the Ag NPs at the Si NW/wafer

92

interface (inset of Figure 4.3 (c)), showing the absence of Ag. The gold, palladium, and carbon peaks visible in the spectrum are due to the same phenomena explained in Section 4.2.1.1. However, the oxygen (O) peak in the spectrum is due to native oxidation in the air.

4.2.1.3 N-doped Si NWs Morphology

Subsequent to MaCE-growing the Si NWs, liquid $POCl_3$ SOD was spin-cast onto the Si NWs. Thereafter it was annealed via phosphorus drive-in dopant diffusion at elevated temperatures (i.e. 700, 800, 900, and 1000 °C) in an N_2 purged high-temperature tube furnace as earlier mentioned in Chapter 3, Section 3.3.2.3, setting out the experiments. Annealing is essential for the formation of n-doped Si NWs. Here we interrogate the effect of n-type doping on the morphological properties of the MaCE-grown Si NWs. For the sake of simplicity, this section refers to the resultant doped wafers as n-doped Si NWs, as electrical transport properties by means of the Hall effect measurement technique and X-ray photoelectron spectroscopy (XPS) characterisation in Sections 4.5 and 4.4 of this chapter will verify whether the phosphorus dopant atoms are electrically active and whether they exist within the Si NWs, respectively.

The same bundle formation realised for the as-synthesised Si NWs seen in Figures 4.2 (a) and 4.3 (a) can be seen for the n-doped Si NWs in the top-view SEM micrographs of Figures 4.4 (a), (c), (e), and (g) for all annealing temperatures. However, certain Si NW attributes seen in Figure 4.4 for n-doped Si NWs differed from the as-synthesised Si NWs; for instance, they showed less Si NW bending and enhanced Si NW accumulation, which will be elaborated on later in this section. In comparing morphological features of the n-doped Si NWs from the top-view, it is realized that an

increase in annealing temperature does not contribute to any obvious modifications in terms of Si NW bending and accumulation.

Figures 4.4 (b), (d), (f), and (h) present the cross-sectional SEM micrographs of n-doped Si NWs annealed at 700, 800, 900, and 1000 °C, respectively. The mean diameter and length measurements for n-doped Si NWs increased from 133 ± 22 nm to 160 ± 17 nm and decreased from 8.21 ± 0.27 μm to 4.48 ± 0.14 μm when compared to the as-synthesised Si NWs. The mean diameter and length of the n-doped Si NWs enhanced and reduced when compared to the as-synthesised Si NWs; this may be attributed to additional layers having formed post-annealing and to sample damage occurring during SEM characterisation preparation. XPS studies in Section 4.4 of this chapter will prove whether extra layers may have formed post-annealing.

The cross-sectional SEM micrographs show that annealing reduced the Si NW density and interface roughness after Si NWs had been MaCE-grown, although no significant variations in Si NW densities and interfaces are observed at elevated temperatures. The reduction in density may be attributed to the enhanced Si NW accumulation and lower Si NW bending [4.2], as previously observed in Figures 4.4 (a), (c), (e), and (g). The reduced Si NW density post-annealing poses an advantage for PV application, as it results in lower reflectance, as proved in reflectance studies by Peng et al. (2011) [1.3]. The reduced interface roughness post-annealing is in good agreement with a previous study [4.3].
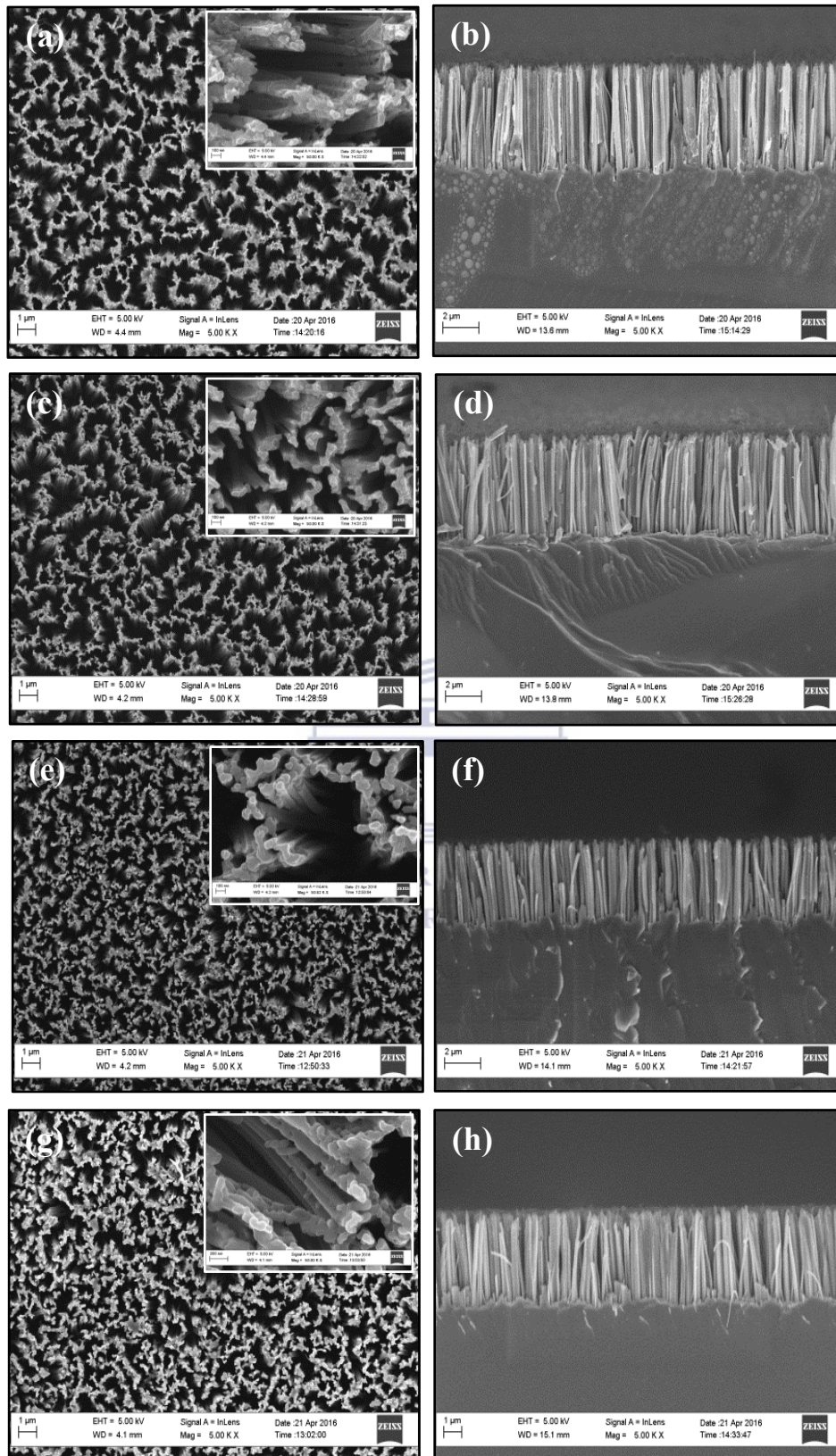
Figure 4.4: The top-view and corresponding higher magnification SEM micrographs ((a), (c), (e), and (g)); Cross-sectional SEM micrographs ((b), (d), (f), and (h)).

Figures 4.5 (a), (b), (c), and (d) present the EDS spectra for n-doped Si NWs annealed at 700, 800, 900 and 1000 °C, respectively. The EDS spectra were acquired from the corresponding EDS scan analysis taken at the interface of the cross-sectional SEM micrographs, seen in the insets. The EDS spectra confirmed the presence of Si (p-type wafer) and P (n-type dopant) in n-doped Si NWs annealed at 700, 800, 900, and 1000 °C.
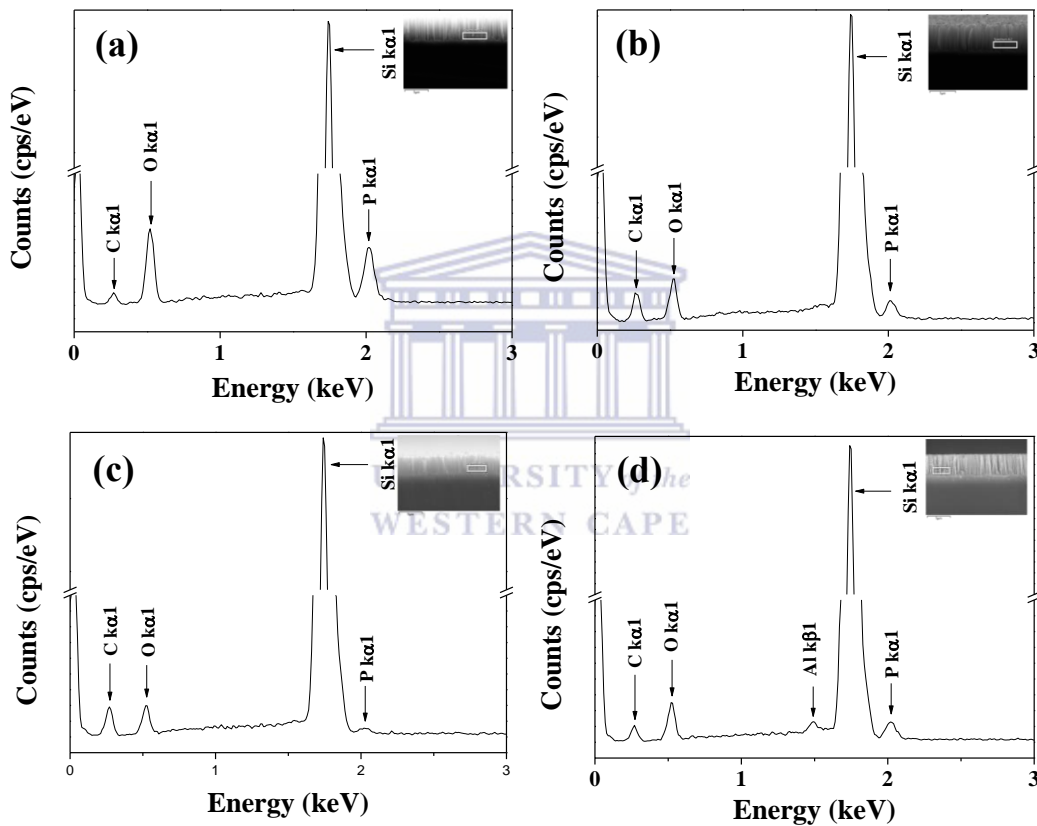

Figure 4.5: EDS spectra ((a), (b), (c), and (d)) with corresponding scan selected-area analysis of n-doped Si NWs annealed at 700, 800, 900, and 1000 °C, respectively.

The presence of the oxygen peaks in the spectra for all n-doped Si NWs may be due to the thermally grown oxidized Si, seen in the schematic of Figure 2.6 (see Chapter 2). The aluminium (Al) peak in the spectrum for n-doped Si NWs annealed at 1000 °C is due to the aluminium stub onto which the sample was mounted, and the carbon peak in

96

the spectra for all n-doped Si NWs is due to an unavoidable contamination in the internal walls of the SEM vacuum chamber during the SEM characterisation, respectively. XPS studies in Section 4.4 will elaborate more on the oxide formation.

4.2.2 Transmission Electron Microscopy Characterisation

Heavier dopant atoms, such as phosphorus, are more tightly bound to the crystal lattice of the starting material, and as a result, that temperatures from 800 °C to 1250 °C are required to ensure practical diffusion rates [4.4]. Hence, TEM characterisation was employed to intentionally study the internal structure of a singular as-synthesised Si NW and n-doped Si NWs under 700 °C and 900 °C drive-in annealing conditions (temperatures both below and within the range of 800 and 1250 °C).

Figure 4.6 presents the TEM micrograph of a singular as-synthesised Si NW grown by the MaCE fabrication technique. The smooth surface of the as-synthesised Si NW that is apparent in the micrograph agrees with various low and short etching condition of the Si wafer (100, 1 to 10 Ω.cm) used in this study; it is controlled by various low and short etching conditions stated in [4.5], which include low hydrogen peroxide (H_2O_2) etchant concentration (from 0.005 to 0.2 M), low temperature (< 25 °C), short etching time (from 15 to 30 minutes) and short Ag NP deposition time. Also, the wafer properties, such as crystal orientation and doping level, affect the surface morphology of the material. If the above conditions are enhanced or changed, a rough-surfaced Si NW with or without pores is induced [4.5]. See Reference 4.5 for the various phenomena for roughness and pore formation.
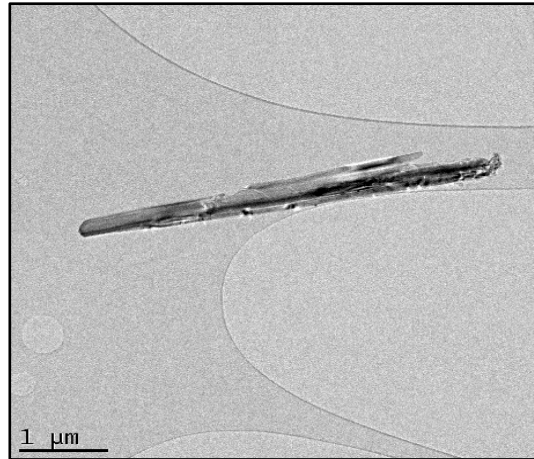
Figure 4.6: TEM micrograph of the smoothly-surfaced singular as-synthesised Si NW grown by the MaCE fabrication method at room temperature.

The n-doped Si NWs annealed at 700 °C and 900 °C are illustrated in the TEM micrographs of Figures 4.7 (a) and (b), respectively. The n-doped Si NW annealed at 700 °C seen in Figure 4.7 (a) exhibits a slight enhancement in surface roughness in comparison to the as-synthesised Si NW. Increasing the annealing temperature to 900 °C showed obvious surface roughness for the n-doped Si NW in Figure 4.7 (b).
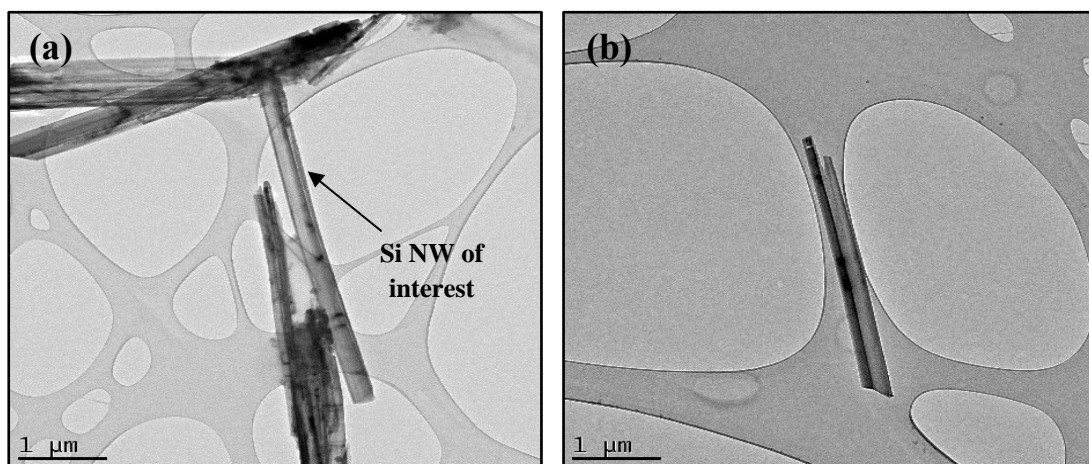

Figure 4.7: TEM micrographs of the roughly-surfaced singular n-doped Si NWs annealed under (a) 700 °C and (b) 900 °C conditions.

It is also widely accepted that the induced surface roughness of a Si wafer and/or Si NWs post-annealing is a consequence of the N_2 carrier gas ambient during annealing [4.6]. It is widely accepted that the surface roughness observed for the n-doped Si NWs facilitates and contributes to light trapping in PV devices, by reducing the reflection of light [1.6].

Having examined the impact of n-type doping on the morphological properties of the MaCE-grown Si NWs, the next section will evaluate whether the MaCE-grown Si NWs and n-doped Si NWs maintained the structural properties of the bulk single-crystalline (100) Si wafer.

4.3 Structural Characterisation

TEM and XRD characterisation techniques were employed to evaluate whether the MaCE-grown Si NWs and n-doped Si NWs maintained the single-crystalline diamond lattice structure of the bulk (100) Si wafer.

4.3.1 Transmission Electron Microscopy Characterisation

A non-uniform amorphous outermost Si oxide layer is observed in the high-resolution transmission electron microscopy (HR-TEM) micrograph of Figure 4.8 (a) for the as-synthesised Si NW and may be attributed to native oxidation in the air as mentioned above in Section 4.2.1.2. Also, amorphous outermost Si oxide layers are evident in the HR-TEM micrographs of Figures 4.8 (b) and 4.8 (c) for the n-doped Si NWs annealed at 700 °C and 900 °C, respectively. The presence of the oxide layer may possibly be thermally-grown oxidised Si. The oxide chemical composition and stoichiometry of a n-doped Si NW sample will be confirmed by XPS presented later on in this study.

As of yet, TEM cannot image single point defects [4.7], but by indirect interpretation, the interruptions marked as rectangles in Figures 4.8 (a), (b), and (c) may be due to phosphorus impurity atom defects. These defects are governed by the vacancy diffusion mechanism in the case of slower diffusion and the interstitialcy mechanism in the case of faster diffusion, as previously stated in Chapter 2, Section 2.6.
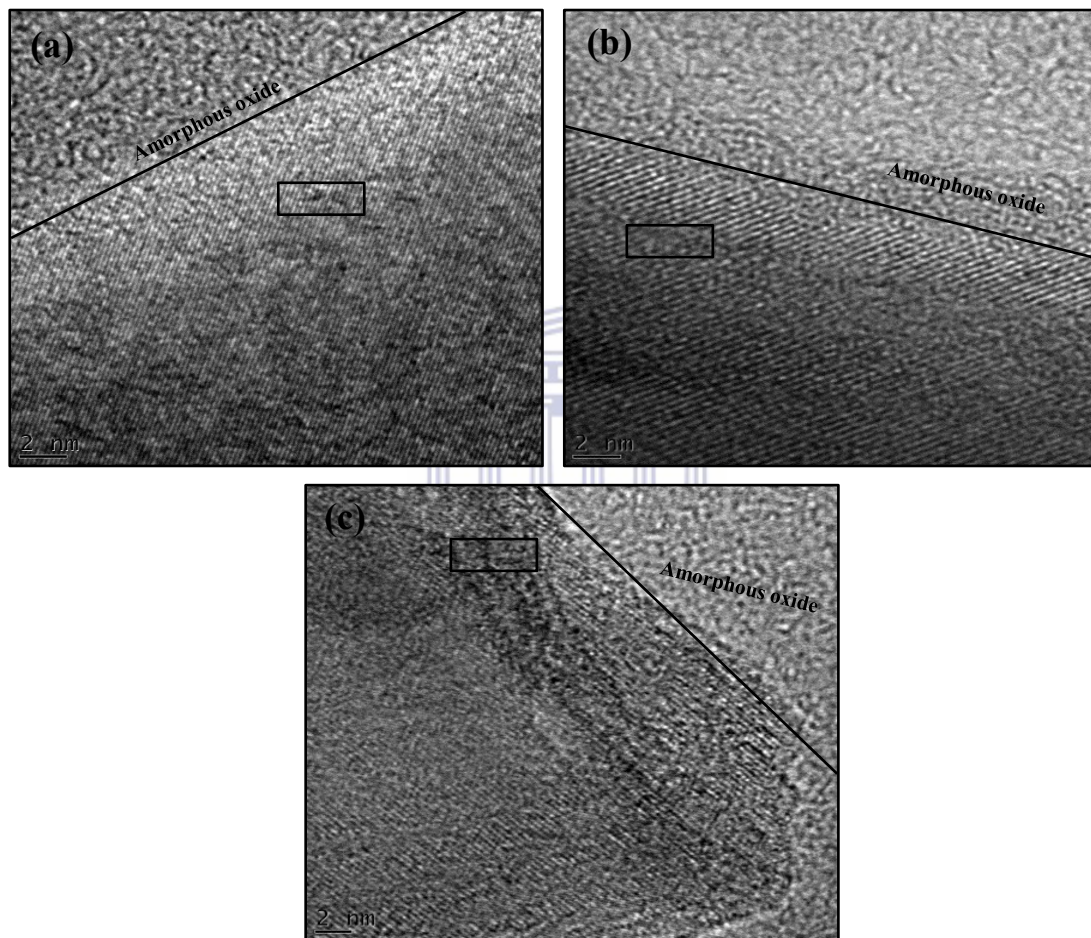

Figure 4.8: HR-TEM micrographs of the singular (a) as-synthesised Si NW sample and n-doped Si NWs annealed under (a) 700 °C and (b) 900 °C conditions.

The insets of the selected area electron diffraction (SAED) patterns of Figures 4.9 (a), (b), and (c) present magnified HR-TEM micrographs of the crystalline structure of the as-synthesised Si NW and n-doped Si NWs annealed at 700 and 900 °C, respectively. The insets were taken from the HR-TEM micrographs of Figure 4.8 to demonstrate the

100

measured interplanar spacings (d) more accurately. The interplanar spacing obtained for the as-synthesised Si NW, n-doped Si NW annealed at 700 °C and n-doped Si NW annealed at 900 °C was 0.3187 nm, 0.3182 nm and 0.3178 nm, respectively.
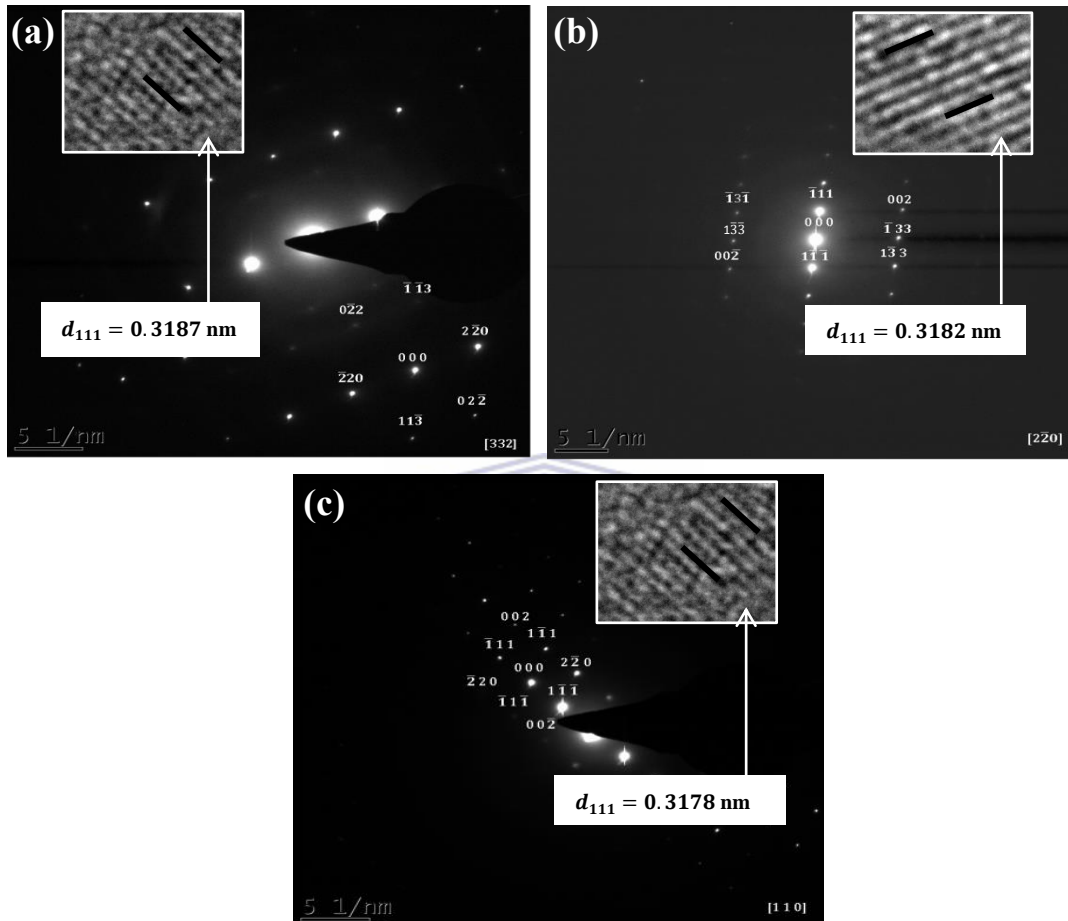

Figure 4.9: SAED patterns of the singular (a) as-synthesised and n-doped Si NWs annealed under (b) 700 °C and (c) 900 °C conditions. Insets: magnified selected-areas from the crystalline structure of the HR-TEM micrographs of Figure 4.8 demonstrating the interplanar spacing (d).

The interplanar spacings for all the samples were consistent with the (111) planes. Hence, the Si NWs are indeed grown along the <100> orientation, as evident in the HR-TEM micrographs of Figures 4.8. The (111) planes are not necessarily perpendicular to the <100> growth direction, as it is known in the literature that the (111) and (100)

101

surfaces make a sharp angle at 54.74° [4.8], which makes sense by visually interpreting the HR-TEM micrographs.

The SAED patterns of Figures 4.9 (a), (b), and (c) were acquired along the [332], [2$\bar{2}$0], and [110] zone axes for the as-synthesised Si NW and n-doped Si NWs annealed at 700 and 900 °C, respectively. The well-aligned atomic planes seen from the HR-TEM micrographs and the diffraction spots from the SAED patterns confirm that the as-synthesised Si NW and n-doped Si NWs retained the single-crystalline diamond lattice structure of the bulk Si wafer.

4.3.2 X-ray Diffraction Characterisation

The structural properties of the as-synthesised Si NWs and n-doped Si NWs were further studied by means of X-ray diffraction (XRD) characterisation.

Figure 4.10 presents the XRD patterns of the as-synthesised Si NWs and n-doped Si NWs annealed at 700 °C and 900 °C. It appears that all the Si NWs hold the original characteristics of the single-crystalline diamond lattice structure of bulk Si that is in agreement with the TEM results. As can be seen from Figure 4.10, all the Si NW wafers have a prominent Si (311) diffraction peak at around $2\theta \approx 56°$. Figure 4.11 presents the magnification of the Si (311) peak prior and subsequent to annealing.
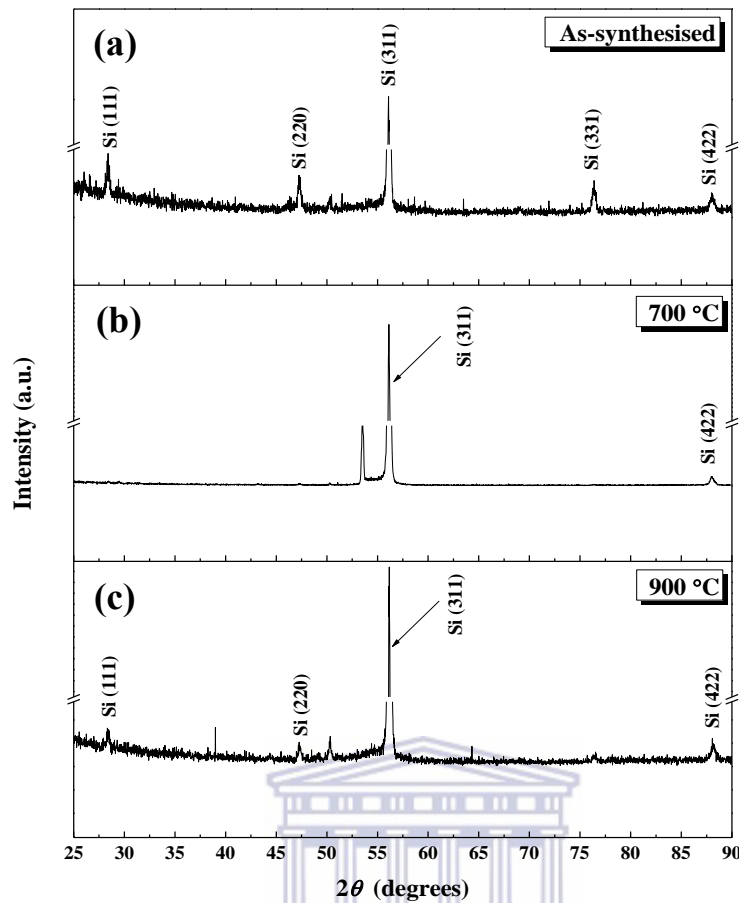
Figure 4.10: XRD patterns of the (a) as-synthesised (MaCE-grown) Si NWs at room temperature and n-doped Si NWs annealed under (b) 700 °C and (c) 900 °C conditions.
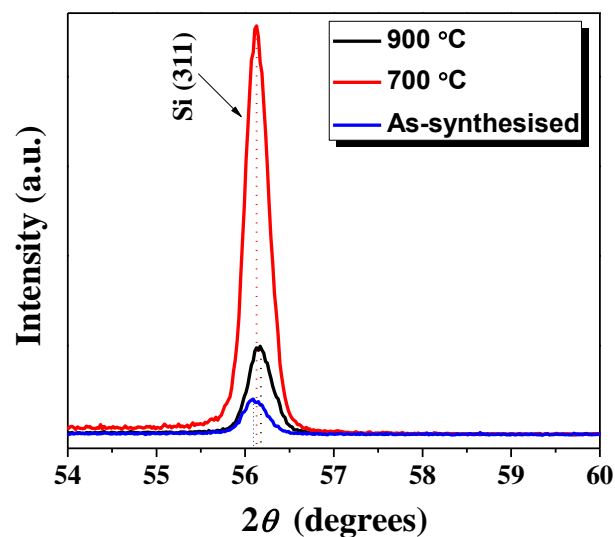

Figure 4.11: Magnification of the Si (311) XRD patterns for the as-synthesised Si NWs and n-doped Si NWs annealed under 700 °C and 900 °C conditions.

103

The as-synthesised Si NWs show a broad and weak Si (311) diffraction peak. It is also apparent that the full width at half maximum (FWHM) was reduced with enhanced annealing temperature, and this is attributed to an increase in the average crystal size. The FWHM values listed in Table 4.1 for the as-synthesized Si NWs and n-doped Si NWs annealed at 700 °C and 900 °C are given as 1.6401, 1.6388, and 1.6378 degrees, respectively. The increased crystal size is attributed to the higher thermal energy with annealing temperature leading to more lattice scattering with the Si NW sample that ultimately reduces the mobility [4.9]. The electrical transport properties using the Hall effect measurement technique will confirm the reduced mobility with increasing annealing temperature.

It can also be seen from Figure 4.11 that the crystallinity of the n-doped Si NWs worsens with an increase in annealing temperature; this may be attributed to higher phosphorus dopant concentration that ultimately contributes to increasing defects [1.6, 4.9]. The enhancement in phosphorus dopant concentration with annealing temperature will be confirmed by the electrical transport properties by means of the Hall effect measurement technique.

The Si (311) peak shifts to a higher angle post-annealing from $2\theta = 56.08°$, $56.13°$, and $56.16°$ for the as-synthesised Si NWs and n-doped Si NWs annealed at 700 °C and 900 °C, respectively. According to Bragg's law, as given by Equation (3.3) and the lattice parameter (a) calculated using Equation (3.4), it is expected that the lattice parameter values should decrease post-annealing, due to the enhanced 2θ values with annealing temperature.

Table 4.1: Influence of post-deposition annealing on the structural properties of the as-synthesised Si NWs and n-doped Si NWs.

Temperature (°C)	Peak Position 2θ for (311) (degrees)	Interplanar Spacing *d* (nm)	Lattice Parameter *a* (nm)	Full width at half maximum FWHM (degrees)
As-synthesised	56.08	0.1640	0.5440	1.6401
700	56.13	0.1639	0.5435	1.6388
900	56.16	0.1638	0.5432	1.6378

Figure 4.12 presents a comparative plot of the lattice parameter as a function of the annealing temperature that was calculated from the SAED patterns of Figure 4.9 in the TEM analysis and that obtained from the given interplanar spacing values of Table 4.1 in the XRD analysis. The lattice parameter values as determined by TEM linearly decreases from 0.5589 ± 0.0012 nm to 0.5370 ± 0.0007 nm with enhanced annealing temperature for the as-synthesised Si NWs and n-doped Si NWs annealed at 700 °C, respectively. The lattice parameter value rapidly enhanced to 0.5628 ± 0.0025 nm with an increase in the annealing temperature for the n-doped Si NWs annealed at 900 °C.

In contrast, there is a linear decrease in the lattice parameter values with enhanced annealing temperature as determined by the XRD analysis. The lattice parameter values obtained in XRD of the as-synthesised Si NWs at room temperature (RT) is determined

105

to be 0.5440 nm, while that of the n-doped Si NWs annealed at 700 °C and 900 °C is 0.5435 nm and 0.5432 nm, respectively. The XRD analysis provides a more precise means of measuring the lattice parameter value as a result of a larger imaging area capability, giving an average value across the sample as opposed to a localised lattice parameter value obtained in TEM due to the small sample size. Hence, the lattice parameter analysis here onwards is based on the value given by XRD.

The lattice parameter value calculated in XRD for the as-synthesised Si NWs (0.5440 nm) is higher than the lattice parameter value in the literature (0.5431 nm) [4.10], reported for the bulk Si diamond lattice structure at room temperature. The enhanced lattice parameter value for the as-synthesised Si NWs shows that the structure is enlarged along the preferred growth direction having tensile stress applied; it may be attributed to the occurrence of the Ag-catalyst initially present in the Si wafer [4.11].

The lattice parameter values for the n-doped Si NWs are found to be approaching the reported value for bulk Si with enhanced annealing temperature. This indicates that the presence of the lattice compression is due to the phosphorus impurity atom defects since the atomic radii of the phosphorus atoms are smaller than those of the Si host atoms [4.9, 4.12]. The lattice parameter values for the n-doped Si NWs also reduce with enhanced annealing temperature due to the increase in phosphorus dopant concentration with annealing temperature. These phenomena obey Vegard's law, which states that the change in the lattice parameter value is directly proportional to the dopant concentration and the difference between dopant and host atomic radii [4.13].
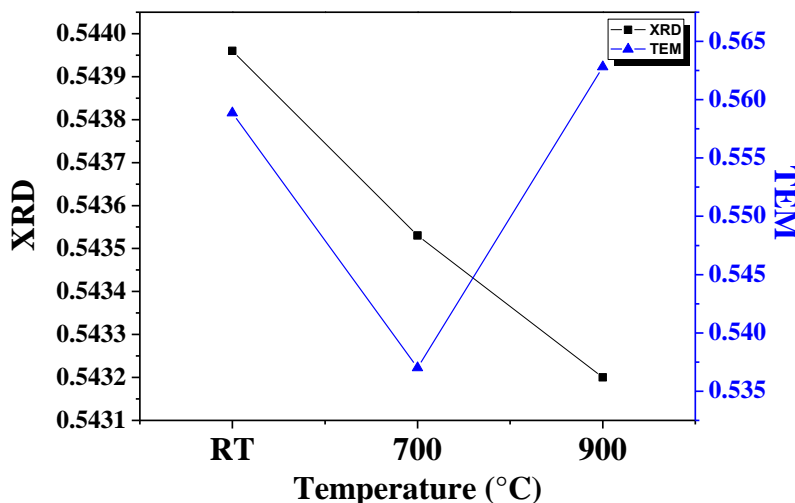
Figure 4.12: Variation in the lattice parameter (*a*) for n-doped Si NWs as a function of annealing temperature.

Having examined whether the MaCE-grown Si NWs and n-doped Si NWs had an impact on the structural properties of the single-crystalline diamond lattice structure of the starting (100) bulk Si wafer, the next section will focus on the compositional properties of n-doped Si NWs annealed at 1000 °C.

4.4 Compositional Characterisation

4.4.1 X-ray Photoelectron Spectroscopy

X-ray photoelectron spectroscopy (XPS) was used to study the chemical composition, bonding status of phosphorus and silicon, and the location of the phosphorus dopants in the n-doped (phosphorus-doped) Si NWs annealed at 1000 °C.

4.4.1.1 Chemical Composition

Figure 4.13 presents the overall XPS spectrum of the n-doped Si NWs. It can be seen that the n-doped Si NWs are composed of fluorine (F), oxygen (O), nitrogen (N), carbon

107

(C), phosphorus (P), and silicon (Si). The F 1s, O 1s, N 1s, C 1s, P 2s, Si 2p peaks have corresponding binding energies (BEs) of approximately, 687.9, 533.9, 402.4, 286.2, 193.0, and 104.3 eV, respectively. The presence of the peak related to phosphorus in the Si NWs is the result of phosphorus as a dopant. The oxygen-related peak is due to an oxide of Si on the Si NW surface. The $_x(P_yO_z)$ layer, which was deposited after the spin-on doping process, reacted with the Si NWs to form silicon dioxide (SiO_2) on the surface during the drive-in annealing process, as previously outlined in Chapter 2, Section 2.4. Fluorine, nitrogen, and carbon are typically surface contaminants.
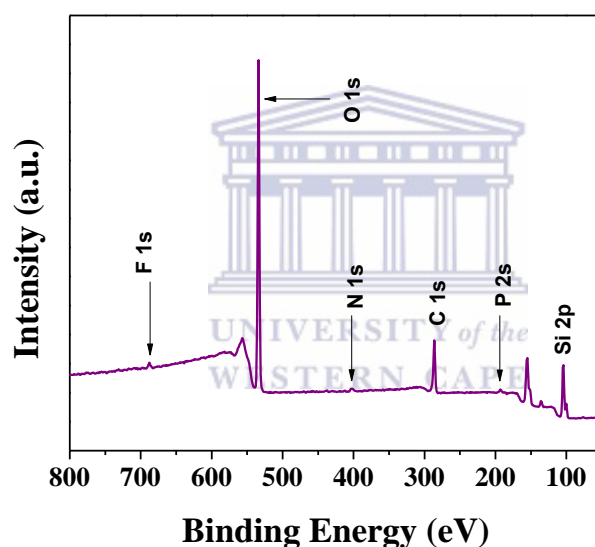
Figure 4.13: XPS surface spectrum of n-doped Si NWs annealed at 1000 °C.

4.4.1.2 Bonding Status

Figure 4.14 (a) and (b) shows the surface analysis of the XPS Si 2p and P 2p spectra for the n-doped Si NWs annealed at 1000 °C, respectively. There are two peaks centred at approximately 104.6 eV and 100.4 eV in the Si 2p spectrum of Figure 4.14 (a), corresponding to the SiO_2 and Si-Si bonds, respectively. It is obvious that the SiO_2 peak is the most prominent on the surface of the n-doped Si NWs.

The peak positioned at approximately 135.5 eV corresponds to the phosphorus pentoxide (P_2O_5) bond in the P 2p spectrum of Figure 4.14 (b). The SiO_2 and P_2O_5 bonds seen in Figures 4.14 (a) and (b) that originate from the proposed layers formed after the drive-in annealing stage (see Figure 2.6 in Chapter 2) verify the oxide composition and stoichiometry of the non-uniform disordered amorphous outermost Si layer in the HR-TEM micrographs of Figure 4.8; it confirms the stoichiometry of the deposited layer formed after the spin-on doping process.

As previously mentioned in Chapter 2, Section 2.4, the P_2O_5 layer reacts with the Si NWs to form SiO_2 on the Si NW surface. In this way, the Si NW wafer is oxidised, and it forms a SiO_2/Si NW thin interface. At the same time, P_2O_5 reacts with SiO_2 to form a phosphorus silicate glass (PSG) layer on the pure SiO_2 layer. The SiO_2 is continuously increasing at the interface [1.13], which explains the vast amount of SiO_2 seen at the surface of the XPS Si 2p surface spectrum of Figure 4.14 (a).

Neither the PSG nor the SiO_2 layer is supposed to be present at the surface since hydrofluoric (HF) acid is supposed to remove these parasitic layers after the annealing process. There are a few causes that might explain the presence of the PSG and SiO_2 layers: (i) The weakly concentrated (5%) HF is not an effective means to remove the parasitic layers after the annealing process, (ii) the HF removal time of 60 seconds is too short to remove the parasitic layers (PSG and SiO_2), or (iii) the oxide formation on the surface is due to a native oxide.
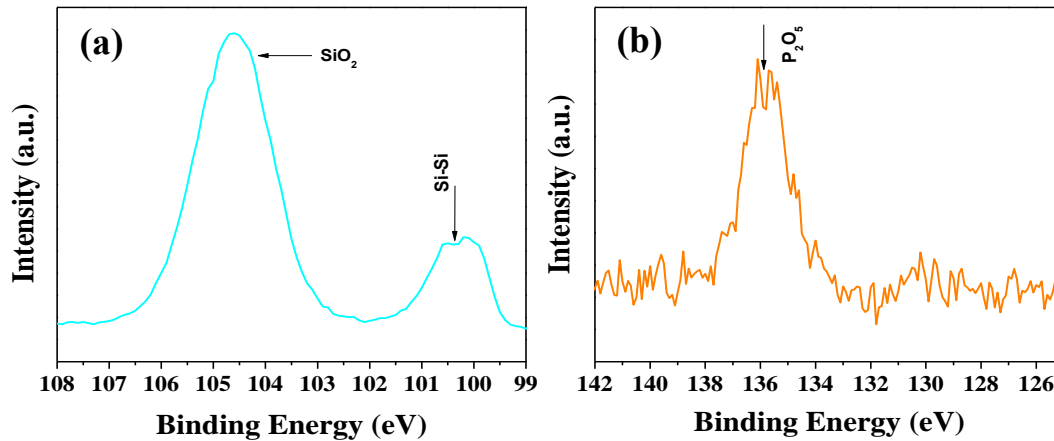
Figure 4.14: XPS surface spectra of the (a) Si 2p and (b) P 2p bonds of the n-doped Si NWs annealed at 1000 °C.

4.4.1.3 Location of the Phosphorus Dopants

Figure 4.15 presents the XPS depth-profiles of the (a) Si 2p and (b) P 2p peaks for the n-doped Si NWs annealed at 1000 °C. The XPS scans were acquired after each sputter time of 0, 48, 1068 seconds, respectively. The co-occurrence of the two peaks (SiO_2 (104.6 eV) and Si (100.4 eV)) seen in the Si 2p spectrum of Figure 4.15 (a) at a sputter time of 0 seconds, suggests that the spotted position is near the SiO_2/Si NW interface. At the same depth, a prominent P_2O_5 (135.8 eV) bond is spotted in Figure 4.15 (b), which corresponds to the phosphorus dopant atoms incorporated in the underlying SiO_2 layer.

When the sputtering time is increased to 48 seconds, the SiO_2 peak (103.7 eV) decreases in intensity compared to the higher intensity peak of Si (99.7 eV) as can be seen in Figure 4.15 (a). This implies that the spotted location is near the Si NW surface. At the same time, a P-Si bond (129.3 eV) appears and the P_2O_5 peak (135.2 eV) shrinks

110

in intensity as can be seen in Figure 4.15 (b). This indicates that the phosphorus dopant atoms exist near the Si NW surface.

When the sputtering time is further enhanced to 1068 seconds, the oxidised Si peak vanishes entirely. A prominent Si-Si peak (99.9 eV) exists in the Si 2p spectrum of Figure 4.15 (a). At the same time, the P_2O_5 peak vanishes entirely and a prominent P-Si (129.3 eV) exists as evident in Figure 4.15 (b). This implies that the phosphorus atoms are diffused in the Si NW layer and will form the n-type dopant.
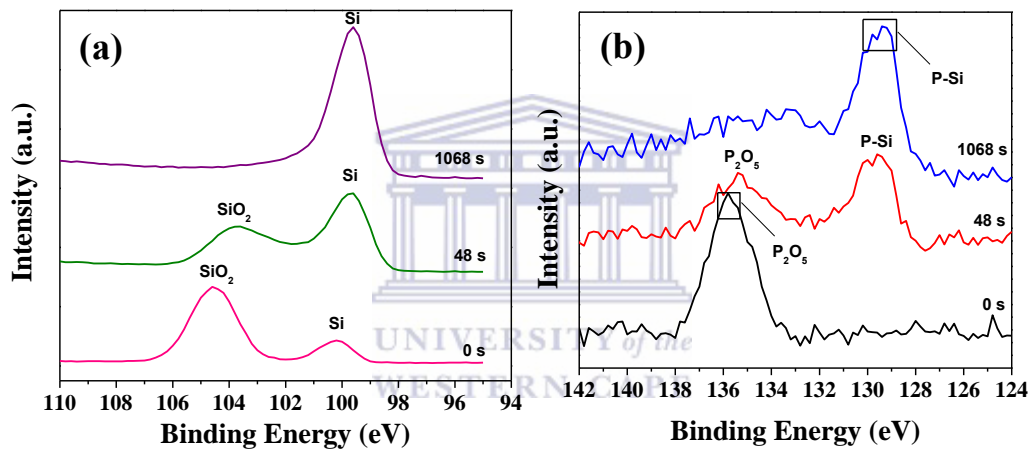

Figure 4.15: XPS depth-profiles of the (a) Si 2p and (b) P 2p peaks for the n-doped Si NWs annealed at 1000 °C.

These results show that the phosphorus dopant atoms exist mostly at the interface and within the Si NWs. This phenomenon is a result of the phosphorus atoms redistributed near the SiO_2 until equilibrium is reached. But since the diffusivity of phosphorus is less in SiO_2 than in Si, the diffusivity due to redistribution does not count. It is confirmed that phosphorus is blocked by the SiO_2 layer and piles up at the Si NW layer. The pile-up phenomena depend on the diffusivity and segregation coefficient of phosphorus in SiO_2. Hence more phosphorus dopant atoms exist in the Si NW layer, due to the high

segregation coefficient ($m \sim 10$) and the slow diffusivity of phosphorus in SiO_2 [1.13, 4.14].

Having examined the compositional properties of the n-doped Si NWs annealed at 1000 °C, in particular the chemical composition, location of the phosphorus dopants and the bonding status of phosphorus and silicon in the n-doped (phosphorus-doped) Si NWs annealed at 1000 °C, the next section will look into the temperature dependence of electrical transport properties using the Hall effect measurement technique.

4.5   Electrical Transport Characterisation

Electrical transport properties of Si NWs are important to produce functional electronic devices such as SCs [1.3]. In this section, the temperature dependence of electrical transport properties using the Hall effect measurement technique on n-doped Si NWs annealed at 700, 800, 900, and 1000 °C was studied.
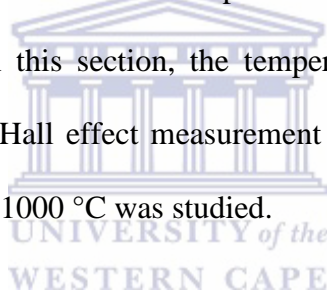
4.5.1 Hall Effect Measurement Technique

4.5.1.1 Temperature Dependence of Dopant Concentration

The variation of the dopant concentration (N_D) with annealing temperature, as can be seen in Figure 4.15, increased from about 9×10^{17} cm^{-3} to 8×10^{19} cm^{-3} with enhanced annealing temperature. The dopant concentration value in this study is considerably lower than the dopant concentration value of 10^{20} cm^{-3} found by Vaurette et al. (2008) [4.15] and could possibly mean that the spin-on doping method in this work is not a good means of controlling the phosphorus-containing source while spin-doping. As previously stated in Chapter 3, Section 3.4.5, the negative sign of the Hall voltage confirmed that the dopant concentration type is n-type. For the purpose of convenience,

the negative sign is not considered. Consequently, these results confirm that the pentavalent phosphorus dopants changed the electrical transport properties of the initially p-type Si NWs to n-type conducting. In addition, these results also prove that the phosphorus dopant atoms are electrically active in the Si NWs. The overall increase of the dopant concentration of the phosphorus dopant atoms with annealing temperature is attributed to the improved ability of the phosphorus atoms to diffuse into the Si NWs at higher annealing temperature [4.16].

The dopant concentration given here is a measure of the amount of electrically active P dopant atoms, as opposed to the total amount of dopant atoms measured by Secondary Ion Mass Spectrometry (SIMS) [4.17]. Hence it is expected that the dopant concentration values measured using the Hall effect measurement technique is considerably lower than the total dopant concentration of the phosphorus dopant atoms measured by SIMS.
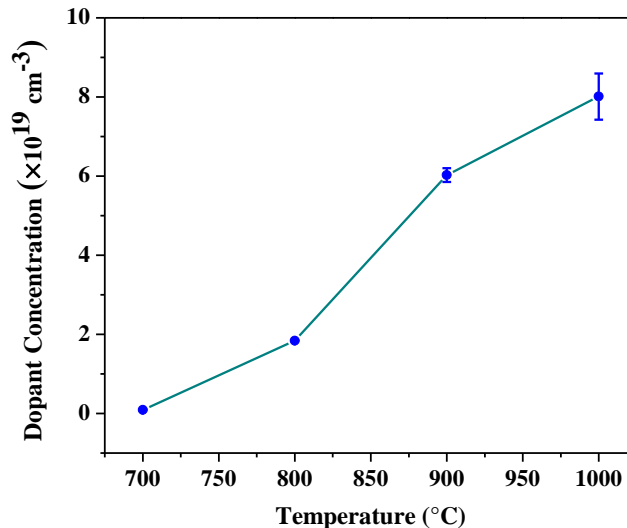

Figure 4.15: Temperature dependence of dopant concentration of n-doped Si NWs by means of the Hall effect.

4.5.1.2 Temperature Dependence of Mobility

Figure 4.16 illustrates the variation of the mobility (μ) of the phosphorus dopant atoms with annealing temperature. The mobility deteriorates from about 184 cm^2/V.s to 67 cm^2/V.s as the annealing temperature is enhanced. The enhancement in the dopant concentration with annealing, as seen in Figure 4.15, increases the possibility of a silicon host atom colliding with a dopant in a given time period and the shorter the mean free time between the collisions become, hence reducing the mobility. The reduced mobility with increasing annealing temperature is also inferred to the enhanced lattice (phonon) scattering. The phonon concentration enhances with annealing temperature, causing increased lattice scattering, which results in the reduced mobility [4.18].
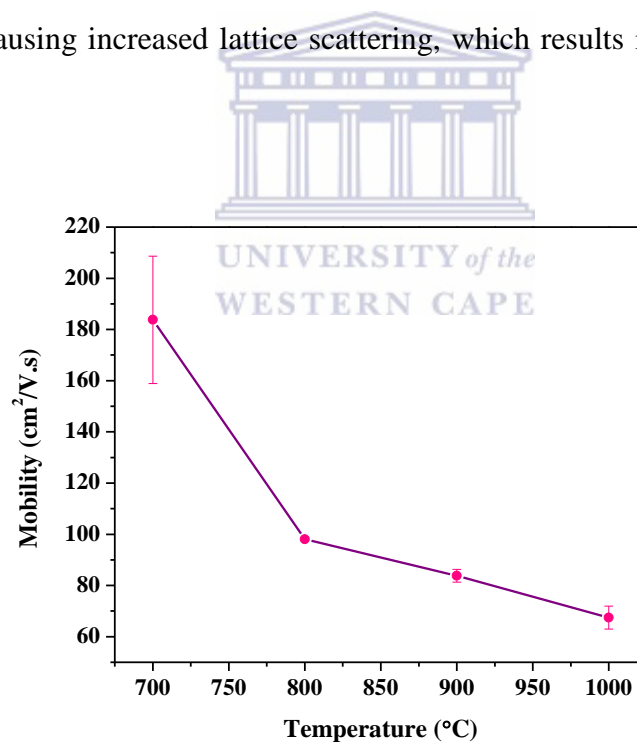

Figure 4.16: Temperature dependence of the mobility of n-doped Si NWs by means of the Hall effect.

4.5.1.3 Temperature Dependence of Resistivity

The resistivity (ρ) values for the n-doped Si NWs were calculated using Equation (3.11) and were found to decrease from about 0.962 to 0.025 Ω.cm with increasing annealing temperature, as evident from Figure 4.17. The larger dopant concentration improves the conductivity of the n-doped Si NWs, thus reducing the resistivity with enhanced annealing temperature [4.16].
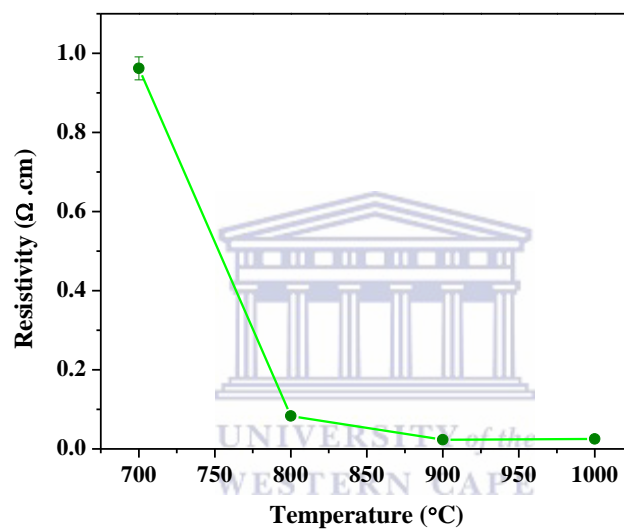

Figure 4.17: Temperature dependence of the resistivity of n-doped Si NWs by means of the Hall effect.

4.6 References

[4.1]   Puglisi, R., Garozzo, C., Bongiorno, C., Di Franco, S., Italia, M., Mannino, G., Scalese, S. & La Magna, A. (2015). Molecular doping applied to Si nanowires array based solar cells. Solar Energy Materials and Solar Cells, 132, 18.

[4.2]   Jaballah, A., Moumni, B. & Bessais, B. (2012). Formation, rapid thermal oxidation and passivation of solar grade silicon nanowires for advanced photovoltaic applications. Solar Energy, 86(6), 1955.

[4.3] Doping techniques - Waferfabrication - Semiconductor Technology from A to Z - Halbleiter.org. 2017. Available: https://www.halbleiter.org/en/waferfabrication/doping/ [2017 ,March 12].

[4.4]   Wu, S., Zhang, T., Zheng, R. & Cheng, G. (2012). Facile morphological control of single-crystalline silicon nanowires. Applied Surface Science. 258(24), 9792.

[4.5]   Dalsa Semiconductor Inc. 2011. Patent No. EP2019080 A3. Germany. [2017, March 23].

[4.6]   P.J. Goodhew and F.J. Humphreys. (Ed.). (1988). Electron Microscopy and Analysis. (2nd ed.). Taylor & Francis, London.

[4.7]2017.Available:http://www.inst.eecs.berkeley.edu/~ee243/sp10/EE143/homework/143S2006-02-soln.pdf [2017, June 3].

[4.8]   Tyagi, M., Tomar, M. & Gupta, V. (2013). Postdeposition annealing of NiOx thin films: A transition from n-type to p-type conductivity for short wave length optoelectronic devices. Journal of Materials Research, 28(05), 723.

[4.9]   2017. Available: http://Yardley, J.T. Silicon basics. 2001 – 11/09 [2017, July 15].

[4.10] Ouertani, R., Hamdi, A., Amri, C., Khalifa, M. & Ezzaouia, H. (2014). Formation of silicon nanowire packed films from metallurgical-grade silicon powder using a two-step metal-assisted chemical etching method. Nanoscale Research Letters, 9(1), 574.

[4.11] Fukata, N., Sato, K., Mitome, M., Bando, Y., Sekiguchi, T., Kirkham, M., Hong, J. & Wang, Z. et al. (2010). Doping and Raman Characterization of Boron and Phosphorus Atoms in Germanium Nanowires. ACS Nano, 4(7), 3807.

[4.12] Leszczyński, M., Litwin-Staszewska, E., Suski, T., Bąk-Misiuk, J. & Domagała, J. (1995). Lattice Constant of Doped Semiconductor. Acta Physica Polonica A, 88(5), 837.

[4.13] Lau, F., Mader, L., Mazure, C., Werner, C. & Orlowski, M. (1989). A model for phosphorus segregation at the silicon-silicon dioxide interface. Applied Physics A Solids and Surfaces, 49(6), 671.

[4.14] Vaurette, F., Nys, J., Deresmes, D., Grandidier, B. & Stiévenard, D. (2008). Resistivity and surface states density of n- and p-type silicon nanowires. Journal of Vacuum Science & Technology B: Microelectronics and Nanometer Structures, 26(3), 945.

[4.15] Chen, T. & Liao, T. (2013). Influence of Annealing Temperature on the Characteristics of Ti-Codoped GZO Thin Solid Film. Journal of Nanomaterials, 2013, 1.

[4.16] Lee, H., Kang, M., Choi, S., Kang, G., Myoung, J. & Song, H. (2013). Characteristics of silicon solar cell emitter with a reduced diffused phosphorus inactive layer. Current Applied Physics, 13(8), 1718.

[4.17] Ayele, Y., Yohannes, Z. & Benor, A. (2016). Effect of phosphorus dopant concentration on the carrier mobility in crystalline silicon. Ethiopian Journal of Science and Technology, 9(2), 113.

UNIVERSITY *of the*
WESTERN CAPE

Chapter Five: Conclusion and Recommendations

Silicon nanowires (Si NWs) demonstrate unique electrical and optical properties compared to bulk Si for its use in photovoltaic (PV) applications. The two basic approaches for Si NW fabrication are the bottom-up approach, such as the vapour-liquid-solid (VLS) growth, and the top-down approach, such as the recently developed metal-assisted chemical etching (MaCE) fabrication technique.

In this study, n-doped Si NWs were synthesised from p-type MaCE-grown Si NWs using a phosphorus (P)-containing spin-on dopant (SOD) by means of a post-deposition technique. Most analysis on the diffusion doping of Si NWs are carried out with VLS-grown Si NWs. Hence, there is a limitation in the understanding of the precise diffusion process of applying the SOD to MaCE-grown Si NWs.

This study focussed on the effect of n-type doping on the morphological and structural properties of MaCE-grown Si NWs. Also the compositional and electrical transport properties of the n-doped Si NWs were interrogated.

The morphological properties of the MaCE-grown Si NWs and n-doped Si NWs were studied using scanning electron microscopy (SEM) and transmission electron microscopy (TEM) characterisation techniques. The structural properties of MaCE-grown Si NWs and n-doped Si NWs were studied using TEM and X-ray diffraction (XRD) characterisation techniques. The compositional and electrical transport

properties of n-doped Si NWs were studied using X-ray photoelectron spectroscopy (XPS) and the Hall effect measurement technique, respectively.

The SEM results showed that the vertically-aligned Si NWs formed infers that the etching is isotropic and grows along the <100> direction. The SEM results also showed that the as-synthesised Si NWs and n-doped Si NWs accumulated at the tips due to the capillary action during the MaCE drying process; however, less Si NW bending and accumulation was observed at the tips due to reduced Si NW density in n-doped Si NWs. The average diameter and length of the n-doped Si NWs annealed at 700 °C and 900 °C increased and decreased, as compared to the as-synthesised Si NWs and may be attributed to the extra layers created post-annealing and to sample damage during SEM preparation, respectively. The TEM results showed that the surface roughness post-annealing for the n-doped Si NW enhanced as a result of the N_2 carrier gas ambient.

TEM and XRD studies confirm that the as-synthesised Si NW and n-doped Si NWs kept the single-crystalline diamond lattice structure of the bulk Si wafer.

The XPS results showed that phosphorus dopant atoms exist mostly within the Si NW layer, due to the low diffusivity and high segregation coefficient of phosphorus in SiO_2.

The Hall effect measurement technique showed that the electrical transport properties of the n-doped Si NWs improved with increasing annealing temperature.

Since there is a limitation in the understanding of the precise diffusion process of applying the SOD source to the MaCE-grown Si NWs, few to no resources explain the layer(s) formed post spin-on doping and post diffusion annealing. Hence, in this study proposed layers were created as can be seen in Chapter 2 (Figures 2.5 and 2.6) for the spin-on doping and diffusion drive-in processes, respectively. Hence, it is recommended

that the morphological and compositional properties post spin-on doping should be studied, as opposed to only studying the various properties post-annealing.

For future reference, a solar cell (SC) based on n-doped MaCE-grown Si NWs can be fabricated after application of the drive-in diffusion annealing technique.